UNIVERSITY OF CALIFORNIA SAN DIEGO SAN DIEGO STATE UNIVERSITY

Toward high-frequency determinstic simulations: source, path and site effects

A dissertation submitted in partial satisfaction of the requirements for the degree

Doctor of Philosophy

in

Geophysics

by

Zhifeng Hu

Committee in charge:

University of California San Diego

Professor Joel Conte Professor Peter Shearer

San Diego State University

Professor Kim Olsen, Chair Professor Steven Day Professor Samuel Shen Doctor Daniel Roten

Copyright
Zhifeng Hu, 2021
All rights reserved.

The dissertation of Zhifeng Hu is approved, and it is accept-
able in quality and form for publication on microfilm and
electronically.
Chair

University of California San Diego San Diego State University

2021

DEDICATION

To my family

Xiaoyang, Xiuhong and Fei

EPIGRAPH

You must know that a person's ability to discern the truth is directly proportional to his knowledge.

— Cixin Liu, The Three-Body Problem

There are only the pursued, the pursuing, the busy and the tired.

— F. Scott Fitzgerald, The Great Gatsby

Never confuse education with intelligence,
you can have a PhD and still be an idiot.

— Richard P. Feynman

TABLE OF CONTENTS

Dissertation A	approval Page
Dedication .	
Epigraph	
Table of Cont	ents
List of Figure	s
List of Tables	
Acknowledge	ments
Vita	
Abstract of the	e Dissertation
Chapter 1	Introduction 1.1 Motivation
Chapter 2	Calibration of the Near-surface Seismic Structure in the SCEC CommunityVelocity Model Version 412.1 Introduction12.2 Numerical Approach1Acknowledgements1Tables and Figures1Supplementary Materials1
Chapter 3	Calibration of the Near-surface Seismic Structure in the SCEC Community Velocity Model Version 4

4.1 Introduction 4.2 Numerical Approach	Chapter 4	Calibration of the Near-surface Seismic Structure in the SCEC Community
4.2 Numerical Approach		Velocity Model Version 4
Acknowledgements Tables and Figures Supplementary Materials Chapter 5 Modeling of Empirical Transfer Functions with 3D Velocity Structure 5.1 Introduction 5.2 Data 5.3 TFs 5.4 Model Construction 5.4.1 Numerical simulations 5.5 GVDA 5.6 TKCH05 5.7 Discussion 5.8 Summary and Conclusions Acknowledgements Tables and Figures Supplementary Materials		
Tables and Figures Supplementary Materials Chapter 5 Modeling of Empirical Transfer Functions with 3D Velocity Structure 5.1 Introduction 5.2 Data 5.3 TFs 5.4 Model Construction 5.4.1 Numerical simulations 5.5 GVDA 5.6 TKCH05 5.7 Discussion 5.8 Summary and Conclusions Acknowledgements Tables and Figures Supplementary Materials		4.2 Numerical Approach
Supplementary Materials Chapter 5 Modeling of Empirical Transfer Functions with 3D Velocity Structure 5.1 Introduction 5.2 Data 5.3 TFs 5.4 Model Construction 5.4.1 Numerical simulations 5.5 GVDA 5.6 TKCH05 5.7 Discussion 5.8 Summary and Conclusions Acknowledgements Tables and Figures Supplementary Materials		Acknowledgements
Chapter 5 Modeling of Empirical Transfer Functions with 3D Velocity Structure 5.1 Introduction 5.2 Data 5.3 TFs 5.4 Model Construction 5.4.1 Numerical simulations 5.5 GVDA 5.6 TKCH05 5.7 Discussion 5.8 Summary and Conclusions Acknowledgements Tables and Figures Supplementary Materials		Tables and Figures
5.1 Introduction 5.2 Data 5.3 TFs 5.4 Model Construction 5.4.1 Numerical simulations 5.5 GVDA 5.6 TKCH05 5.7 Discussion 5.8 Summary and Conclusions Acknowledgements Tables and Figures Supplementary Materials		Supplementary Materials
5.2 Data 5.3 TFs 5.4 Model Construction 5.4.1 Numerical simulations 5.5 GVDA 5.6 TKCH05 5.7 Discussion 5.8 Summary and Conclusions Acknowledgements Tables and Figures Supplementary Materials	Chapter 5	Modeling of Empirical Transfer Functions with 3D Velocity Structure
5.3 TFs 5.4 Model Construction 5.4.1 Numerical simulations 5.5 GVDA 5.6 TKCH05 5.7 Discussion 5.8 Summary and Conclusions Acknowledgements Tables and Figures Supplementary Materials		5.1 Introduction
5.4 Model Construction 5.4.1 Numerical simulations 5.5 GVDA 5.6 TKCH05 5.7 Discussion 5.8 Summary and Conclusions Acknowledgements Tables and Figures Supplementary Materials		5.2 Data
5.4.1 Numerical simulations 5.5 GVDA 5.6 TKCH05 5.7 Discussion 5.8 Summary and Conclusions Acknowledgements Tables and Figures Supplementary Materials		5.3 TFs
5.5 GVDA		5.4 Model Construction
5.6 TKCH05 5.7 Discussion		5.4.1 Numerical simulations
5.7 Discussion		5.5 GVDA
5.8 Summary and Conclusions		5.6 TKCH05
Acknowledgements		5.7 Discussion
Tables and Figures		5.8 Summary and Conclusions
Supplementary Materials		Acknowledgements
		Tables and Figures
Appendix		Supplementary Materials
	Appendix .	
<u> </u>		

LIST OF FIGURES

Figure 2.2:	Simulation region for the La Habra event (rectangle) and locations of 259 strong ground motion stations (circles represent soil sites with surface V_S < 1000 m/s and red triangles represent rock sites with surface V_S >= 1000 m/s). The named sites (triangles with black edge) are selected for further comparisons in Figure 12. The star depicts the epicenter of the La Habra earthquake	15
Figure 2.2:	(a) V_S profile sample locations in California. Triangles denote rock sites and circles denote soil sites, and (b) extracted V_S profiles. The top panel zooms into the top 500 m	16
Figure 3.1:	Simulation region for the La Habra event (rectangle) and locations of 259 strong ground motion stations (circles represent soil sites with surface V_S < 1000 m/s and red triangles represent rock sites with surface V_S >= 1000 m/s). The named sites (triangles with black edge) are selected for further comparisons in Figure 12. The star depicts the epicenter of the La Habra earthquake	27
Figure 3.2:	Description of the source model used in this study. (a) Total moment on the fault. The contours represent rupture time at a 0.4 s interval starting from 0. (b) and (c) represent the sum of the moment rates for all subfaults and the Fouerier amplitude spectrum, respectively.	28
Figure 3.3:	(a) Top 150 m and (b) 0-4000 m V_S profiles at the 259 stations. The black and red curves represent rock (surface $V_S >= 1000$ m/s) and soil (surface $V_S < 1000$ m/s) sites, respectively. The darker curves denote the sites with farther distance from the source	29
Figure 3.4:	FAS derived from the records (black) and CVM-S (blue) for the (a) eastwest component, (b) north-south component and (c) vertical component. The left and right columns represent soil sites with surface V_S smaller and larger than 1000 m/s, respectively. The solid line is the median of FAS over the site group, the narrow band is the 95% confidence interval of the median, and the wide band depicts the standard deviation centered at the median.	30
Figure 3.5:	(a) Surface V_S extracted from CVM-S, and (b) V_{S30} from Thompson (2018) in our model domain (values in the left bottom corner are not available). The star denotes the epicenter.	31
Figure 3.6:	Representative V_S profiles for (a) soil sites and (b) rock sites from CVM-S. The thick black curves depict the averaged velocity profiles for all 220 soil and 39 rock sites directly extracted from CVM-S. The thin lines show the V_S refinement resulting from our proposed method for different z_T depths between 200 m and 1500 m. The dashed curve shows the V_S profile calculated	
	using our preferred z_T value of 1000 m	32

Figure 3.7:	The SH1D response for the refined profiles using various z_T depths for av-	
	erage (a) soil and (b) rock sites, divided by the response obtained with the	
	averaged soil and rock profiles from CVM-S	33
Figure 3.8:	Bias of FAS for the two horizontal components averaged over all (a) soil	
	and (b) rock sites for CVM-S at all 259 stations, superimposed with the	
	corresponding SH1D response. The black curves denote CVM-S and other	
	labeled curves represent refinements to various depths using SH1D results.	34
Figure 3.9:	Bias of FAS on the (a) east-west, (b) north-south and (c) vertical compo-	
	nents, calculated from 3D simulations in CVM-S and with V_S refinements	
	of 350 m, 700 m, and 1000 m. A positive (negative) value depicts overpre-	
	diction (underprediction). The left (right) column shows soil (rock) sites.	
	The solid line is the median of FAS, where the narrow band is the 95%	
	confidence interval of the median, and the dashed lines depict the standard	
	deviation centered at the median	35
Figure 3.10:	Maps of interpolated log10-based FAS bias between four 3D models and	
	data: (a) CVM-S, and CVM-S with refinements of (b) 350 m, (c) 700 m and	
	(d) 1000 m, calculated from the synthetics and records at 259 stations. The	
	warm (cool) colors represent overprediction (underprediction). The circles	
	(triangles) depict soil (rock) sites. Note the log10-based colorbar	36
Figure 3.11:	Maps of interpolated log10-based FAS bias for two 3D CVMs and data. (a)	
	CVM-S with refinement depth of 350 m and $Q_S = 0.15V_S$, and (b) CVM-S	
	with refinement of 1000 m and $Q_S = 0.05V_S$. Warm (cool) colors represent	
	overprediction (underprediction). Circles depict soil sites and triangles show	
	rock sites	37
Figure 3.12:	Cumulative kinetic energy and Fourier velocity spectra at six rock sites. The	
	subtitles show the names of the sites and their hypocentral distance	38
Figure 3.13:	Rock site V_S profiles (defined as surface $V_S >= 1000$ m/s) from CVM-S, and	
	CVM-S and CVM-H with (default) Ely et al. (2010) GTL refinement depth	
	of 350 m	39
Figure 3.14:	(a) V_S profile sample locations in California. Triangles denote rock sites and	
	circles denote soil sites, and (b) extracted V_S profiles. The top panel zooms	
	into the top 500 m	40
Figure 3.15:	Bias of FAS of the (a) east-west, (b) north-south and (c) vertical component,	
	calculated from 3D simulations in CVM-S with V_S refinement depths of 350	
	m and 1000 m along with attenuation models $Q_S = 0.05V_S$, $Q_S = 0.1V_S$, and	
	$Q_S = 0.15V_S$. A positive (negative) value means overprediction (underpre-	
	diction). The left (right) columns show soil (rock) sites. The solid line is	
	the median of FAS, where the narrow band is the 95% confidence interval	
	of the median, and the dashed lines depict the standard deviation centered at	
	the median	41

Figure 3.16:	Average FAS bias for frequencies between 0.15-1 Hz at rock sites plotted as a function of site surface V_S for (a) three-component average, (b) eastwest, (c) east-west and (d) vertical components. The shades represent 95% confidence intervals estimated using bootstrap.	42
Figure 4.1:	(a) V_S profile sample locations in California. Triangles denote rock sites and circles denote soil sites, and (b) extracted V_S profiles. The top panel zooms into the top 500 m	49
Figure 5.1:	Site map of Garner Valley Downhole Array (GVDA), denoted by the star. The rectangle depicts the extent of the modeling domain, where the contours depict elevation in meters. The triangle denotes a nearby outcrop site GVAR.	72
Figure 5.2:	The color version of this figure is available only in the electronic edition. (a) Multiresolution index of valley bottom flatness (MRVBF) and (b) the bedrock depth map surrounding GVDA, which is depicted by a triangle in both figures. (c) The mapping function from MRVBF to bedrock depth, with	73
Figure 5.3:	GVDA marked with an asterisk. The color version of this figure is available only in the electronic edition	74
	model. The color version of this figure is available only in the electronic edition	75
Figure 5.4:	Comparison between the theoretical transfer functions (TTFs) computed using the 3D model and the SH1D model at GVDA, with the two-sigma scatter of empirical transfer functions (ETFs) shaded in gray. The color version of this figure is available only in the electronic edition.	76
Figure 5.5:	Site map of TKCH05, denoted by the star. The rectangle depicts the extent of the modeling domain, where the contours depict elevation in meters. The	77
Figure 5.6:	color version of this figure is available only in the electronic edition (a) Borehole log at TKCH05 (from Thompson <i>et al.</i> 2012). (b) Borehole V_S profiles at TKCH05 and HKD090, as well as for our simplified 1D model.	77
Figure 5.7:	The color version of this figure is available only in the electronic edition. (a) Comparison between TTFs and the two-sigma scatter of the ETF for 3D and 1D models at TKCH05. Solid and dashed lines without markers are the 3D and 1D models based on the borehole log profile, respectively; solid and dashed lines with diamond markers depict the 3D and 1D models, based on the simplified downhole profile. (b,c) Comparison of 1.5–8 Hz observed east—west component surface ground motions with those obtained from convolution of the downhole records with the TTFs from models using the simplified profile for the (b) 3D model and (c) 1D model. The color	78
	version of this figure is available only in the electronic edition	79

Figure 5.8:	(a) MRVBF and (c) depth to bedrock in the vicinity of TKCH05, with the	
	site location denoted by the triangle. (b) West–east A–A' and (d) north–south	
	B-B' cross sections intersecting TKCH05, the downhole sensor is marked	_
	with the asterisk. The color version of this figure is available only in the	
	electronic edition	80
Figure 5.9:	(a) The Gibbs and Steller velocity profiles at GVDA, in which the bedrock	
	depth is 64 (solid line) and 88 m (dashed line), respectively. (b) Comparison	
	between the two-sigma scatter of the ETFs (gray shaded) and the TTFs from	
	the 3D models assembled with the Gibbs and Steller profiles, respectively.	
	The color version of this figure is available only in the electronic edition	81
Figure 5.10:	Comparison between the median ensemble ETF, the TTF from the 3D model	
_	without and with small-scale heterogeneities (SSHs) at TKCH05. The gray	
	shaded region is the range of maximum and minimum values encountered	
	in TTFs from these realizations of SSHs. The color version of this figure is	
	available only in the electronic edition	82
Figure 5.11:	Energy on the (a) horizontal and (b) vertical components at the site TKCH05.	
	(c) Total energy along depth using the simplified velocity profile at TKCH05	
	with different incidence angles. The gray horizontal line, at around 100 m	
	depth, depicts the downhole site depth. The color version of this figure is	
	available only in the electronic edition	83
Figure S5.1:	(a) Map of events (purple triangles) used for computing the ETFs at GVDA.	
	The red triangle depicts the event used in simulations. (b) Recorded acceler-	
	ations (normalized) along West-East direction at 10 randomly selected sites.	
	The maximum amplitude is showed to the left of each line	85
Figure S5.2:	(a) Map of events (purple triangles) used for computing the ETFs at TKCH05.	
	The red triangle depicts the event used in simulations. (b) Recorded acceler-	
	ations (normalized) along West-East direction at 10 randomly selected sites.	
	The maximum amplitude is showed to the left of each line	86
Figure S5.3:	Snapshots of V_X at TKCH05 along the A-A' cross section in Figure 5.8c,	
	bandpass filtered between 4.5 and 5 Hz. (a), (c) and (e) display snapshots	
	of the 3D model, where the gray contour lines represent interfaces between	
	bulks with difference Vs; the green star denotes the downhole site and the	07
E. 05.4	green line marks its depth. (b), (d) and (f) are for the 1D model	87
Figure S5.4:	Same as Figure S5.3, except along the B-B' cross section in Figure 5.8c	88

LIST OF TABLES

Table 3.1:	: Simulation parameters used for the deterministic ground motion simulations	
	of the 2014 La Habra earthquake	24
Table 3.2:	Rock site information	25
Table 3.3:	Average FAS biases for all three components for various models	26
Table 5.1:	Earthquakes Used to Compute the Empirical Transfer Functions at Garner	
	Valley Downhole Array (GVDA)	71
Table 5.2:	Earthquakes Used to Compute the Empirical Transfer Functions at TKCH05	72

ACKNOWLEDGEMENTS

First and foremost, I would like to express my deepest sense of gratitude my supervisor, Professor Kim Olsen, for his invaluable supervision, support, and tutelage during the course of my PhD degree. Kim always gives me the freedom to explore problems, allows me to try different approaches, and correct me every time before I dive deep into a wrong direction. He is always responsive to asking and patient to answering, even if my questions are naive. His suggestions and comments are so detailed and constructive that they easily refresh my thoughts and guide me towards real research. I am always impressed by his skills in applying physical sense in solving problems and extracting relevant knowledge from his "brain" hard drive accurately in no time. He emphasized big picture in seismology, while in the same time teached me how to present scientific findings, polish academic reports and communicate with the community. What I learned from Kim is a great wealth to me in my whole life.

It is my privilege to thank my committee members for their great mentorship and guidance. I thank Professor Steve Day, who is always supportive and warm. Even during the hardest days, I feel encouraged thinking of his optimistic altitudes and enthusiasm in life. He is rigorous to scientific problems but open to every exploration, to which he always provides precious comments and insights. It was an honor to attend his retirement ceremony in person and see how a life of contribution to science is remembered and respected. Professor Peter Shear is the person leading me to this field by his popular "Introduction to Seismology", which is still the source of answers in my study. He showed me that science can be elegant yet fun. I thank Professor Samuel Shen for his valuable help in mathematics in our discussions. I also thank Professor Joel Conte for his kind suggestions and comments. Dr. Daniel Roten is extraordinarily supportive in Kim's group, who taught me about the details in research practice from the beginning. I cannot overestimate how much I learned from him, and it is my privilege to work with someone as versatile, brilliant, and productive as Daniel. I am also grateful to Professor Shuo ma at SDSU, who is warm and caring, for sharing his experiences and life advice.

I am grateful to all the professors at Scripps and SDSU, who taught a wide series of courses that prepared me in my following research, including Professor Duncan Agnew, Professor Adrian Borsa, Professor Catherine Constable, Professor Steven Constable, Professor Yuri Fialko, Professor Guy Masters, Professor David Sandwell, Professor Peter Shearer, and Professor Dave Stegman at Scripps Institution of Oceanography at UCSD; Professor Michael Holst in Department of Mathematics at UCSD; Professor Shou Ma and Professor Kim Olsen at SDSU.

My research fulfillment would not be possible without the help and communications from my coauthors and collaborators from the Southern California Earthquake Center. I thank Kim Olsen, Steven Day, Daniel Roten, Christine Goulet, Robert Graves, Fabio Silva, Scott Callaghan, Kevin Milner for their incredible collaborations and discussions.

I appreciate the support and friendship from my incredible fellows and friends: Nan Wang, Teyang Yeh, Yongfei Wang, Shiying Nie, Qian Yao, Wei Wang, Zefeng Li, Yuxiang Zhang, Bill Savran, Kyle Withers, Drake Singleton, Rumi Takedatsu, Xiaohua Xu, Kang Wang, Wenyuan Fan, Zhao Chen, Yuval Levy, Zeyu Jin, Yue Du, Zheng Fang, Junlong Hou, Mingda Li, Yuan Huang. Thank you for making my time at San Diego a wonderful memory. I also appreciate the administrative advisors and staffs, including Gilbert Bretado, Wayne Farquharson, Paul Dean, and Sara Miceli at UCSD; Irene Occhiello, Pia Parrish, Heather Webb, Susan Langsford, and Pat Walls at SDSU, for their consistent and timely assistance.

Finally, I would also like to extend my deepest gratitude to my parents, Xiaoyang and Xiuhong, for always listening to me, supporting me, and encouraging me. Lastly but most importantly, I thank Fei for being there for me through thick and think, for always believing in me, and for enriching my life in numerous amounts of ways.

Chapter 2, in full, is a reformatted version of a paper currently being prepared: Hu, Z., Roten, D., Olsen, K.B., and Day, S.M. (2021). Kinematic Source Models for Earthquake Simulations with Fault-zone Plasticity. The dissertation author was the primary investigator and author of this paper.

Chapter 3, in full, is currently under review for publication as: Hu, Z., Olsen, K.B., and Day, S.M. (2021). Calibration of the Near-surface Seismic Structure in the SCEC Community Velocity Model Version 4. The dissertation author was the primary investigator and author of the paper.

Chapter 4, in full, is a reformatted version of a paper currently being prepared: Hu, Z. and Olsen, K.B. (2021), 0-5 Hz Deterministic 3D Ground Motion Simulations for the 2014 Mw 5.1 LaHabra Earthquake. The dissertation author was the primary investigator and author of this paper.

Chapter 5, in full, is a reformatted version of the material as it appears in Bulletin of the Seismological Society of America: Hu, Z., Roten, D., Olsen, K. B, and Day, S.M. (2020). Modeling of Empirical Transfer Functions with 3D Velocity Structure. *Bulletin of the Seismological Society of America*. The dissertation author was the primary investigator and author of this paper.

VITA

2015	B.S. in Geophysics, Peking University
2015-2021	Graduate Teaching/Research Assistant, San Diego State University
2021	Ph.D. in Geophysics, University of California San Diego and San Diego State University

PUBLICATIONS

- **Hu, Z.**, Roten, D., Olsen, K.B., and Day, S.M. (2021) Kinematic Source Models for Earthquake Simulations with Fault-zone Plasticity. *In preparing*.
- **Hu, Z.** and Olsen, K.B. (2021). 0-5 Hz Deterministic 3D Ground Motion Simulations for the 2014 Mw 5.1 LaHabra Earthquake. *To be submitted*.
- **Hu, Z.**, Olsen, K.B., and Day, S.M. (2021). Calibration of the Near-surface Seismic Structure in the SCEC Community Velocity Model Version 4. *To be submitted*.
- O'Reilly O., Yeh, T. Olsen, K.B., **Hu, Z.**, Breuer, A.N., Roten D., Goulet C. (2021). A High-order Finite Difference Method on Staggered Curvilinear Grids for Seismic Wave Propagation Applications with Topography, *Bulletin of the Seismological Society of America*. *Submitted*.
- **Hu, Z.**, Roten, D., Olsen, K.B., and Day, S.M. (2020). Modeling of Empirical Transfer Functions with 3D Velocity Structure. *Bulletin of the Seismological Society of America*. doi:10.1785/0120200214.

ABSTRACT OF THE DISSERTATION

Toward high-frequency determinstic simulations: source, path and site effects

by

Zhifeng Hu

Doctor of Philosophy in Geophysics

University of California San Diego, 2021 San Diego State University, 2021

Professor Kim Olsen, Chair

High-frequency ($f_{max} > 1$ Hz) ground motions are closely relevant to building response associated with small structures of the engineering interests. Gaining an deeper understanding of the propagation of seismic waves and characterisite of ground motions, is therefore a principal goal for seismologists and earthquake engineers. Earthquake simulations, physcis-based deterministic simulations in particular, as a valuable complement to (often inadequate) recorded data, have drawn significant attention from the seismic community in the last decades. With the potential ability to accurately characterize broadband wavefield, numerical simulations have their own limitations, namely the difficulty in characterizing the underlying physical parame-

ters in fine scale and accommodating regional-scale domains for risking earthquake study. The primary objective of this dissertations is to explore various model properties that impose high-frequency effects. Chapter 1 is an introduction, providing background and motivation for each of the following chapters. Chapter 2 studies nonlinear effects using dynamic simulations and propose an equivalent kinematic source generator to emulate near-source plasticity in terms of the resulting peak ground velocities. Chapter 3 and 4 focus on model characteristics that govern the high-frequency ground shaking. Chapter 3 proposes a calibration approach that enhances the near-surface velocity structure insufficiently resolved in community velocity models. In Chapter 4, we intensively simulate a series of models with topography, small-scale heterogeneities, frequency-dependent attenuation, low near-surface velocities to investigate their contributions in modulating wavefields and ground motions as the frequency extends up to 5 Hz. In Chapter 5, we incoporates surface topography in constraining the 3D subsurface structure to predicte site response.

Chapter 1

Introduction

1.1 Motivation

Earthquake, a globally frequent phenomenon of ground shaking resulting from vast energy release from Earth interior in short time, is one of the most catastrophic natural hazard to human society. While the majority of earthquakes are too small to be felt by humans, they are detected by seismic sensors more than ever and contribute to our understanding of seismology. Yet major earthquakes with magnitude greater than 7 happen more than once per month and still remain not predictable, which necessitates continueing study to migigate their damage.

Ground motion prediction is central to seismic hazard management, because the ground shaking is oftentimes the most diminant source of damages and immediate cause of following secondary damages, such as tsunamis, landslides, liquifaction and fires. A straightforward approach is to collect earthquake records and perform statistical analysis to formulate empirical functions that incorporate correlations between eartqhuake characteristics and measurements. This method is referred to as ground motion models (GMMs) or ground motion prediction equations (GMPEs; e.g., Abrahamson *et al.*, 2014; Boore *et al.*, 2014; Campbell and Bozorgnia, 2014; Chiou and Youngs, 2014; Idriss, 2014). However, due to sporadicity of extreme earth-

quakes and sparsity of direct measurements, the estimate of strong ground motions using GM-PEs, especially within close distances to earthquakes, suffers from large uncertainty. Numerical methods are therefore widely adopted to investigate both historic and scenario eartquakes, serving as a feasible complement or a substitute to recorded data, in order to estimate seismic rick even beyond the range of existing data. This makes physics-based methods valuable for public earthquake emergency prepareness and design seismic-resistent structures in civil engineering.

Physics-based determinastic earthquake simulation, sometimes also referred to as ground motion prediction, is the process of solving elastodynamic equations numerically by incoporating physical theories with velocity models constrained by direct measurements and indirect inversions. Because analytical methods cannot provide solutions for realistic sophisticated models and stochastic or empirical methods generally provide median values with estimates of uncertainty only, the derministic numerical methods are developed, including finite-difference, finiteelement, boundary element, spectral element and the pseudo-spectral methods (e.g., Sánchez-Sesma et al., 1982; Frankel and Vidale, 1992; Olsen et al., 1995; Graves, 1996; Bao et al., 1998; Seriani, 1998; Käser and Dumbser, 2006; Chaljub et al., 2006). These numerical methods differ from each other with indivisual advantages or disadvanatages in terms of accuracy, efficiency and ranges of applicibility. Among all these methods, the finite-difference method is still the most widely used in large scale three-dimensional (3D) simulations considering its simplicity in mesh generation and GPU parallelization, efficiency and scalability. Additionally, the finite-difference methods have recently been improved to support plasticity, discontinuous mesh discretization and irregular surface topography (e.g., Roten et al., 2017; Nie et al., 2017; Zhang et al., 2012; O'Reilly et al., 2021). Based on extensive varifications and validations, though under various simplifications and assumptions due to insufficiently resolved paramters and computaional limits, these methods have been developed and applied successfully in a series of meaningful research practicices (e.g., ShakeOut, PetaShake, M9 Cascadia; for more details readers are referred to Cui et al., 2009a; Cui et al., 2009b; Olsen et al., 2009; Marafi et al., 2019).

With the accelerated advancement of high-performance computing facilities and applications, researchers have achieved considerable progress in higher-freuqency ground motion simulations in the last decades (Graves *et al.*, 2008; Olsen *et al.*, 2009; Bielak *et al.*, 2010; Roten *et al.*, 2012; Savran and Olsen, 2019; Withers *et al.*, 2019). In the meantime, it is accordingly important to identify different aspects to a finer scale that govern the temporal and spatial characteristics of broadband seismic waves. In general, seismology studies three main aspects: source, path, and site effects, covering a broad range of fields including rupture nucleation, rock failure, plastic deformation, attenuation and scattering, 3D geometrical interference, low-velocity amplification, etc. This thesis will introduce and explore some relavant disciplines in more detail below.

1.2 Near-source Plasticity

A number of densely populated regions are located close to major faults where extreme earthquakes are likely to occur, e.g., Los Angeles, San Fransisco, Tokyo, Istanbul and so forth. Nonetheless, near-source ground motions are not sufficiently presented in observed data, which leads to large uncertainty and therefore high ground motion levels at low exceeding probability in probablistic seismic hazard assessments including building code design and ground motion prediction equations (e.g., Hanks *et al.*, 2005; Bommer and Abrahamson, 2006). Physics-based numerical simulations can complement the GMPEs in these regions where observations are undersampled. Nonetheless, most large-scale simulations consider linear deformation only for modeling simplicity (Olsen *et al.*, 2008; Molnar *et al.*, 2014), while studies have shown that crust rocks in the fault damage zone and near the surface experience plastic yielding in extreme earthquakes, which limits the peak ground motions, especially in the near field (Andrews *et al.*, 2007; Ma, 2008; Duan and Day, 2010; Templeton *et al.*, 2010; Dunham *et al.*, 2011). Field *et al.*

(1998) reviewed laboratory results and observations and claimed non-linearity is most effetive at frequencies above 1 Hz. Graves *et al.* (2008) found that non-linear material response can reduce the peak amplitudes of long-period (<1 s) ground motions by up to 70% in the Los Angeles Basin compared to the case with visco-elastic models in numerical simulations.

1.3 Model characteristics in High-Frequency Simulations

Seismic velocity models that incorporate geological, geotechnical and geophysical informations are vastly used in forward simulations. The accuracy of these models are important in minimizing the systematic uncertainties in the following modeling procedures and resulting reliable ground motion predictions. In the past decades, most large-scale deterministic earthquake simulations have been focused on low-frequency ($f_{max} \leq 1$ Hz) seismic waves, which allows rough quantification of model properties due to the intrisic low resolution in the simulation approach. Generally, these simulations excludes surface topography, small-scale spatial heterogeneities and frequency-dependent attenuation, along with the minimum velocity clamped at relatively high values to alleviate computational costs. However, these characteristics are expected to matter much more when entering the high-freugency bandwidth and, more importantly coupled with eath other to impose complicated wavefield modification. For example, Lai et al. (2020) found that surface waves triggered by shallow sources are scattered by both topography and velocity heterogeneities that dominate synthetics over a wide range distance range, and weaker attenuation may increase the envelope duration. The sections below briefly discuss the abovementioned effects according to previous studies and how they can be accommodated and addressed in high-freugency deterministic simulations.

1.3.1 Near surface Low Velocity

The presence of near-surface low-velocity layers has a dramatic effect on the simulated ground motion (Imperatori and Mai, 2015). Shaw *et al.* (2015) investigated the effects of different velocity models and found significant sensitivity of ground motions to the velocity model. Previous studies have evidenced that low near-surface material properties, V_S in particular, can lead to significant amplification, especially at higher frequencies, e.g. 0.5-10 Hz (Boore and Joyner, 1997; Poggi *et al.*, 2011). Imperatori and Mai (2013) reported that low-velocity layers increase coda wave amplitude and duration by trapping energy close to the free surface. Most large-scale determinaitic simulations, however, adopt a larger than realistic surface low velocities, because of the limitation of modeling methods and computing capacity, as well as the common understanding that current crustal model of the Earth is insufficient to accurately model demonstrate the complex scattering the interference in soft shallow soils.

The quantitative identification of properties of shallow materials is one of the main tasks for earthquake modellers. This is not a problem for local site study, because numerous well-established techniques have been applied for this purpose, including seismic borehole logging, surface-wave dispersion survey, cone penetration test, gravity observations and oil-well samples. The regional-scale measurements, however, are technically infeasible and financially prohibitive. For this reason, researchers always rely on 3D crustal velocity model, along with empirical functions, to address eismic hazard assessments. The challenge is then raised improve the accuracy and resolution of shallow crustal materials.

Our method (see Chapter 3) is an update of the Ely *et al.* (2010) method that enhances the shallow velocities, fulfilling the need for detailed description of near-surface structure in numerical simulations, constrained from both the very uppermost (30 m) geological and geotechnical information (e.g., V_{S30}) and the deeper tomographic inversions (e.g., Lee *et al.*, 2014; Shaw *et al.*, 2015).

1.3.2 Topography

Surface topography is known to induce severer seismic risk by amplifying ground motions at high elevations, compared to flat grounds or hollow topographies (Çelebi, 1987; Kawase and Aki, 1990; Massa *et al.*, 2010; Burjánek *et al.*, 2014). The key point in exploring topographic effects is to isolate the contribution of local relief from other factors, such as stratigraphy, the presence of fault damage zone or low-velocity surface layers. In addition, the ideal reference point, which is supposed to share similar geology with topgraphic areas while exempt from topographic effects (Çelebi, 1987; Geli *et al.*, 1988; Chávez-García and Faccioli, 2000), is difficult to determine in reality. Numerical simulations are therefore applied to overcome such limitations and produce flexible ranges of characterizing topographic amplification (Boore, 1972; Sánchez-Sesma and Campillo, 1991; Lovati *et al.*, 2011; Hartzell *et al.*, 2017).

The topographic regions are affected in a frequency band, which is correlated with the characteristic dimensions of the relief. In addition, a wide range geomorphometric parameters are used to describe topography geometry, including slope, curvature, relative elevation, surface roughness are investigated (Ashford and Sitar, 1997; Nguyen and Gatmiri, 2007; Bouckovalas and Papadimitriou, 2005). It is found that smoothed curvature and relative elevation, which are linearly correlated with eath other, are mostly relavant in topographic amplification (Maufroy *et al.*, 2015; Rai *et al.*, 2017). Because the characteristic length is critical and dependent on frequency, the topographic effects behave differently in different frequency bands. As the freuqency increases, the conventional assumptions that topography has ignorable effects below 1 Hz (Boore, 1972; Pischiutta *et al.*, 2010), may not hold and thus is needed in high-frequency simulations.

1.3.3 Anelastic attenuation

Anelastic attenuation of seismic waves suring propogation thorough earth crust can be described as a fractal energy loss per cycle: $Q^{-1}(\mathbf{x}, f) = \sigma E/2\pi E$, where \mathbf{x} is the position and f is the circular frequency and E is the total energy (O'Connell and Budiansky, 1978). The attenuation, as the inverse of the quality factor Q, is composed of internal dissipation and scattering from lethospheric heterogeneities (Sato and Fehler, 2009), which become prominent at high frequencies ($f \ge 1$ Hz). As indicated by its nature, Q affects the ground motion amplitudes mainly, though studies also show that weaker attenuation may prolong the shaking duration, especially on surface waves incited by shallow events (Imperatori and Mai, 2015; Lai $et\ al.$, 2020). Particularly, in southern California, which is the region to study in this chapter, the anelastic attenuation is assumed to have stronger effects due to the lower Q values for both compressional (P) and shear (S) waves compared to techtonically stable areas (Erickson $et\ al.$, 2004; Frankel $et\ al.$, 1990). In addition, the near-surface crust experiences more attenuation, where Q can be as low as 10 in soft sediments (Abercrombie, 1997; Aster and Shearer, 1991).

Q is normally modeled as frequency-dedependent at low frequencies (Aki and Richards, 2002), but observed to increase with frequency above 1 Hz at a power law rate between 0 to 1 (e.g., Aki, 1980; Atkinson, 1995; Erickson *et al.*, 2004). Withers *et al.* (2015) applied the memory-variable approach (Day and Minster, 1984; Emmerich and Korn, 1987; Blanch *et al.*, 1995) to implement the frequency-dependent Q in a 3D staggered-grid finite difference scheme, and showed that Q(f) models generally predict ground motions better than constant Q models. As the simulations are pushed to higher frequencies, the anelastic attenuation becomes progressively important because of the increasing wave cycles within the simulated domain. An accurate modeling of attenuation, along with the power-law exponent in accordance, is critical in physics-based ground motion simulations.

1.3.4 Small-scale Heterogeneities

The heterogeneous nature of the Earth crust, at different scales, is one of the most important factors governing the propagation of seismic wavefields (Levander and Holliger, 1992; Levander *et al.*, 1994; Bean *et al.*, 1999; Helffrich and Wood, 2001; Hedlin *et al.*, 1997). The most prominent phenomenon due to scattering is relavant with coda waves, including envelope broadening (Sato, 1989), waveform variation and travel time shift (Flatté and Wu, 1988). Multiple theoretical studies have been developed to explain the nature of wave scatterings (Aki, 1969; Wu, 1985; Aki and Chouet, 1975), and eventually condensed into the multiple shear-to-shear backscattering theory (Zeng *et al.*, 1991; Zeng, 1993; Zeng *et al.*, 1995).

Deterministic numerical simulations are also extensively used to study the scattering process, distributions of heterogeneities and scattering characteristics by comparing the synthetic results to data records or theretical predictions (Frankel and Clayton, 1986; Roth and Korn, 1993; Shapiro and Kneib, 1993; Thybo *et al.*, 2003). Not until the last decade, regional-scale elastic 3D simulations are carried out for freuqency above 1 Hz due to the computational expense (Hartzell *et al.*, 2010; Pitarka and Ichinose, 2009). On the other hand, stochastical numerical simulations are performed using radiative transfer equation (Gusev and Abubakirov, 1996; Przybilla *et al.*, 2006) or Markov approximation (Saito *et al.*, 2002; Sawazaki *et al.*, 2011). For the sake of ground motion predictions and earthquake engeineering, hybrid techniques are applied to emulate scattering stochastics, mainly at high frequencies, in order to match observed seismograms and ground motion prediction models (Liu *et al.*, 2006; Graves and Pitarka, 2010; Mai *et al.*, 2010). The lack of consiering real medium heterogeneities, however, precludes the presence of spatial correlation within short distance between sites.

The perturbation of crustal material properties is generally superimpsoed onto the base deterministic velocity model via a spatial random field, such as the band-limit von Karman corrlation function (Frankel and Clayton, 1986; Hartzell *et al.*, 2010; Appendix A)), along with Gaussian and exponential correlation functions, which are less favorable for being unable to

match some key scattering phenomena. The determination of the spatial parameters that control the heterogeneities remain largely uncertain yet (e.g., Dolan and Bean, 1997), though researchers have been narrowing the uncertainty (Thybo *et al.*, 2003; Nielsen and Thybo, 2006; Przybilla *et al.*, 2009; Imperatori and Mai, 2013; Imperatori and Mai, 2015)

1.4 Site Amplification Due To 3D Structure

The amplitude of seismic waves is increased when propagating from stiff bedrocks into the lower-velocity soils near the surface (Boore, 1986; Silva and Darragh, 1995). The effects of soft soils on ground motions, referred to as site response (or site effects, site amplification), have been documented and studied since as early as 1900s (e.g., Wood, 1908; Reid, 1910; Gutenberg, 1957). For example, Gutenberg (1957) found that the amplitude of ground motions between 0.67 to 1 Hz were 5 times larger at dry alluvium sites than at crystalline rock sites. Different soil types respond differently when incited by ground motions with various freuqency bands, dependent on the depth of underlying soil column (Aki, 1993). One of the most outstanding example of site amplification due to local geology structure was observed during the *M* 8.1 Mexico Michoacan Eartqhuake in 1985, where the ground motions on soft lake sediments were amplified by a factor of up to 50 compared to nearby competent sites (Singh and Ordaz, 1993). In view of the concern about the potential hazard over metropolitan regions underlain by soft and young sediments, the study of local site condition and the resulting amplification is a fundamental goal for earthquake engineering.

The accuracy of site response estimates depends on the accuracy of the subsurface model used, and this is usually assumed to be controlled by the uncertainty in the site properties, in particular, the shear-wave velocity, V_S (e.g., Barani *et al.*, 2013; Griffiths *et al.*, 2016). V_S is the most important parameter for conventional 1D modeling of the TF, in which it is assumed that surface (and subsurface) motion consists of horizontally polarized plane S waves propagating

through a stack of homogeneous layers (e.g., Kramer, 1996). This modeling procedure (SH1D) ignores the lateral complexity of the often heterogeneous geology and subsurface structure and is, therefore, not able to include potential 2D and 3D amplification effects in the observations (e.g., Roten *et al.*, 2008; Thompson *et al.*, 2012). Zhu *et al.* (2018) performed numerical analysis on 2D basins and found that a constant spectral aggravation factor (Chávez-García and Faccioli, 2000), which quantifies the discrepancy between 1D and 2D/3D models, is insufficient to identify basin effects, especially, in close-to-edge regions of shallow basins. Both observations and analytical solutions suggest that 1D models lack an estimate of spatial variability, caused by complex wave propagation such as basin amplification, surface-wave generation, and scattering, and are, therefore, unable to capture spatial correlations, which may be important for understanding risk, especially, to regional-scale infrastructure (e.g., Olsen and Schuster, 1995; Boore, 2004). Although, recent approaches have attempted to reduce velocity uncertainties in site effect estimation (Matavosic and Hashash, 2012; Teague *et al.*, 2018), these methods either require prohibitively complex processing or are developed for specific cases only.

It is impractical to constrain subsurface structure over a wide region to the resolution (on the order of meters to tens of meters) required for accurate ground-motion estimation to high frequencies (e.g., 10 Hz). Instead, some studies choose to use simple proxies, based on broad site classes to supplement estimates of soil properties and site spatial characteristics, for example, the National Earthquake Hazards Reduction Program (NEHRP) soil classification (BSSC, 2003; Akkar and Bommer, 2010) or a weighted average of V_S in the uppermost 30 m (V_{S30} , e.g., Abrahamson and Silva, 2008; Idriss, 2014). Thompson *et al.* (2012) proposed a scheme to classify surface-downhole site pairs by the extent of interevent variability and goodness of fit between 1D modelling and empirical site response, which can be used to calibrate the constitutive models and guide specific site studies. Despite the use of these characterizations in some generic seismic hazard estimates, for instance, via ground-motion prediction equations, recent work has pointed out the importance of considering site-to-site amplification variability (Atkinson and

Boore, 2006; Atik *et al.*, 2010). These studies show that, even within a single NEHRP or V_{S30} class, the variability of site amplification and spatial correlations is strong enough to contribute significant uncertainty in ground-motion estimates.

In Chapter 5, we propose a method to constrain the near-surface properties using surface topography and perform highresolution 3D numerical simulations to investigate the uncertainty in site response modeling. The simulations naturally take advantage of 3D geotechnical information and are able to incorporate complicated spatially varying amplification effects.

Chapter 2

Calibration of the Near-surface Seismic Structure in the SCEC Community Velocity Model Version 4

The near-surface seismic structure (to a depth of about 1000 m), particularly the shear-wave velocity (Vs), can strongly affect the propagation of seismic waves, and therefore must be accurately calibrated for ground motion simulations and seismic hazard assessment. The Vs of the top 30 m of the crust (Vs30) is often well-characterized from borehole studies, geotechnical measurements, and water wells, while the velocities of the material deeper than about 1000 m are typically determined by tomography studies. However, the material parameters between these two regions are typically poorly constrained due to lack of data constraints. A widely-used method for incorporating the near-surface earth structure is incorporated in the Southern California Earthquake Center (SCEC) Community Velocity Models (CVMs) by interpolating Vs from Vs30 measurements to the S-wave velocity at 350 m (Ely et al., 2010). However, our 3D simulations of the 2014 M5.1 La Habra earthquake in the Los Angeles area using the SCEC CVM-S4.26.M01 model significantly underpredict low-frequency (< 1 Hz) ground motions at

rock sites for the Ely *et al.* (2010) method. On the other hand, extending the Vs30-based refinement of the shallow velocities down to a depth of about 1000 meters improves the fit between our synthetics and seismic data at rock sites considerably, without compromising the fit at soil sites. We recommend that our proposed near-surface velocity refinement at rock sites down to about 1000 meters be incorporated in CVM-S4.26M01, as well as considered for other CVMs.

2.1 Introduction

2.2 Numerical Approach

Data and Resources

Acknowledgements

This research was supported through the U.S. Geological Survey External Program (award #G19AS00021), as well as the Southern California Earthquake Center (SCEC; Contribution Number xx). SCEC is funded by the National Science Foundation (NSF) Cooperative Agreement EAR-1600087 and the U.S. Geological Survey (USGS) Cooperative Agreement G17AC00047. We thank Robert W. Graves for providing the source models and Fabio Silva for providing the station records of the 2014 La Habra earthquake.

Chapter 2, in full, is a reformatted version of a paper currently being prepared: Hu, Z., Roten, D., Olsen, K.B., and Day, S.M. (2021). Kinematic Source Models for Earthquake Simulations with Fault-zone Plasticity. The dissertation author was the primary investigator and author of this paper.

Tables and Figures



Figure 2.1: Simulation region for the La Habra event (rectangle) and locations of 259 strong ground motion stations (circles represent soil sites with surface $V_S < 1000$ m/s and red triangles represent rock sites with surface $V_S >= 1000$ m/s). The named sites (triangles with black edge) are selected for further comparisons in Figure 12. The star depicts the epicenter of the La Habra earthquake.

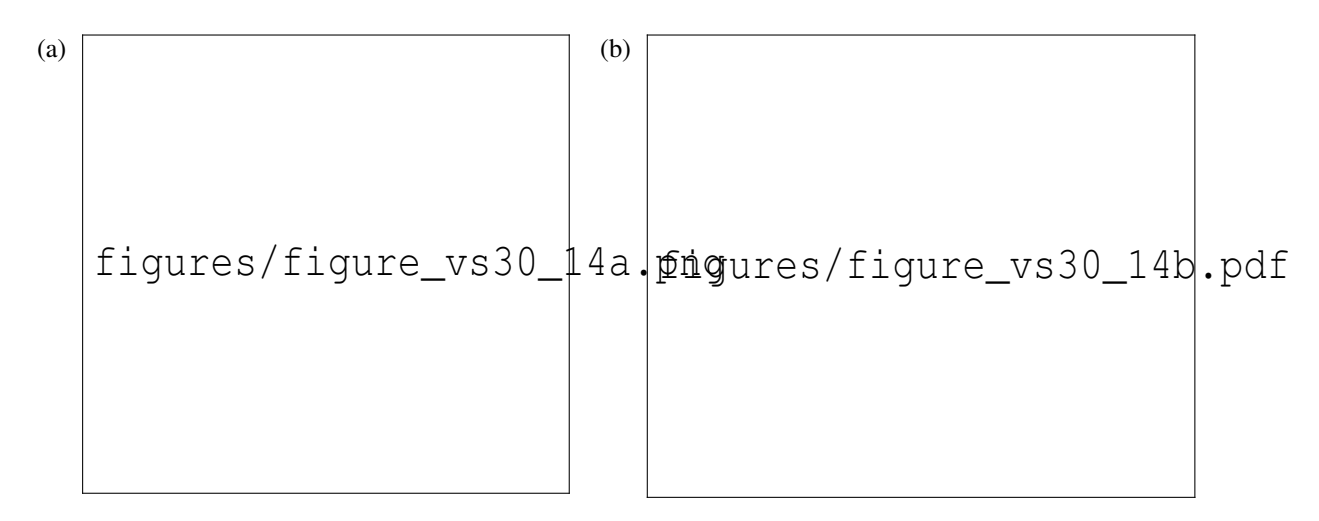


Figure 2.2: (a) V_S profile sample locations in California. Triangles denote rock sites and circles denote soil sites, and (b) extracted V_S profiles. The top panel zooms into the top 500 m.

Supplementary Materials

This supplement includes.

Chapter 3

Calibration of the Near-surface Seismic Structure in the SCEC Community Velocity Model Version 4

The near-surface seismic structure (to a depth of about 1000 m), particularly the shear-wave velocity (Vs), can strongly affect the propagation of seismic waves, and therefore must be accurately calibrated for ground motion simulations and seismic hazard assessment. The Vs of the top 30 m of the crust (Vs30) is often well-characterized from borehole studies, geotechnical measurements, and water wells, while the velocities of the material deeper than about 1000 m are typically determined by tomography studies. However, the material parameters between these two regions are typically poorly constrained due to lack of data constraints. A widely-used method for incorporating the near-surface earth structure is incorporated in the Southern California Earthquake Center (SCEC) Community Velocity Models (CVMs) by interpolating Vs from Vs30 measurements to the S-wave velocity at 350 m (Ely et al., 2010). However, our 3D simulations of the 2014 M5.1 La Habra earthquake in the Los Angeles area using the SCEC CVM-S4.26.M01 model significantly underpredict low-frequency (< 1 Hz) ground motions at

rock sites for the Ely *et al.* (2010) method. On the other hand, extending the Vs30-based refinement of the shallow velocities down to a depth of about 1000 meters improves the fit between our synthetics and seismic data at rock sites considerably, without compromising the fit at soil sites. We recommend that our proposed near-surface velocity refinement at rock sites down to about 1000 meters be incorporated in CVM-S4.26M01, as well as considered for other CVMs.

3.1 Introduction

Ground motion amplification due to the near-surface structure is widely accepted and well-studied (Gilbert et al., 1907; Field, 2000), and needs to be incorporated in numerical simulations of earthquakes to produce accurate ground motion results. The time-averaged shear-wave velocity (Vs) in the upper 30 m (Vs30) is routinely used as a representation of the site condition in ground motion prediction models and building codes (Borcherdt, 1994; Bozorgnia et al., 2014; International Code Council, 2014). For this purpose, several methods have proposed useful methods to derive Vs30 from topography (Wald et al. 2007), supplemented with nearsurface geological information (Thompson et al. 2014; Wills et al. 2015). However, with the continuing advancement in the Vs30-based methodologies by the seismic hazard community (e.g., Thompson et al. 2014, Heath et al. 2020), it is clear that Vs30 is not a good single proxy for the estimation of site amplification (e.g., Steidl 2000, Lee and Trifunac 2010 and Shingaki et al. 2018). One reason is the prohibitive cost of measuring velocity profiles at the resolution needed for seismic hazard analysis, leading to highly approximate results from interpolating limited Vs30 values and combining geological units. Furthermore, Vs30 value is found to be a product complicated by age and grain size, and therefore includes inherent inaccuracy within the soil category classification. Finally, Vs30 cannot account for depth-dependent or lateral velocity variations, which all affect the seismic wavefields.

While the current approximations to correct for site effects serve an important purpose,

a fully physics-based approach for seismic hazard analysis presents itself as a more difficult, but robust, long-term goal. In such an approach, the full wavefield is computed deterministically to maximum frequencies of 5 Hz or higher using a realistic 3D velocity model (e.g., Withers et al. 2019a,b; Hu and Olsen 2021). A necessary ingredient in producing accurate synthetic seismograms using physics-based simulations is an accurate velocity model for the model region. Community Velocity Models (CVMs) have been developed for such purpose, e.g., the Southern California Earthquake Center (SCEC) CVMs (Small et al., 2017), the Cascadia CVM (Stephenson et al., 2017) and the Subsurface Structure Model maintained by the Japan Seismic Hazard Information Station (Fujiwara et al. 2017). These velocity models are often generated by combining 3D tomographic inversion from seismic waves (e.g., Tape et al. 2009, Lee et al. 2014) with shallow geotechnical information (e.g., Vs30) and often yield a fixed resolution of a few hundreds of meters along depth. The spatial resolution of large-scale tomographic studies is generally limited by the density of ray paths, particularly in the upper 1000 m of the crust. While a relatively coarse resolution may be acceptable for the lower crust, that is insufficient to resolve shallower, more complicated structures with more rapid velocity variation. Unfortunately, data constraints on the velocities for the material between depths of about 30 m and 1000 m are limited to relatively rare seismic refraction studies (e.g. Teague et al. 2018) or borehole logs (e.g, Stellar 1996, Thompson 2012).

Previous studies have attempted to bridge the data constraints at shallow (< 30 m) and deeper (> 1000 m) depths for rock sites. For example, Boore and Joyner (1997) generated a continuous depth-dependent Vs function based on 3 different intervals. The Vs profile in the upper 30 m was constructed from interpolated shallow average arrival times. At depths below 4 km, Vs was estimated from the P-wave velocity (Vp), measured from earthquake location studies and velocity surveys, on the assumption of a fixed Poisson ratio at 0.25. Finally, the shallow and deeper Vs were connected using two power-law functions. Ely et al. (2010) proposed a generalized method that modifies the surface Vs from Vs30 and then interpolates velocities down

to 350 m depth, which has been implemented in some of the SCEC CVMs. The Vs30 values adopted by Ely et al. (2010) were obtained from the geology-based Vs30 map of Wills and Clahan (2006) for California and the topography-based estimations by Wald and Allen (2007) outside California. The determination of 350 m used for the depth extent of the Vs refinements by Ely et al. (2010) was based on qualitative comparison between seismic synthetics and data records from the 2008 M5.4 Chino Hills, CA, earthquake.

In this study, we aim to quantify the accuracy of the top 1000 m of crust in the greater Los Angeles area in California using using 3D wavefield simulations of the 2014 M5.1 La Habra earthquake, as well as propose an improved refinement method for rock site, if needed. The paper is organized as follows: we first briefly introduce our numerical approach to obtain the simulated ground motions, present an approximate 1D analysis of site amplification to evaluate the potential to improve site amplification at rock sites, and finally evaluate different rock site refinements using 3D wave propagation simulation and provide our recommendation.

3.2 Numerical Approach

Data and Resources

The UCVM program used to extract velocity meshes can be obtained from SCEC on https://github.com/SCECcode/UCVMC (last accessed 12/2020). The simulations were performed on Summit at the Oak Ridge Leadership Computing Facility in Tennessee. Most of the data-processing work was done using Python and the Generic Mapping Tools package (https://www.generic-mapping-tools.org, last accessed 04/2021).

Acknowledgements

This research was supported through the U.S. Geological Survey External Program (award #G19AS00021), as well as the Southern California Earthquake Center (SCEC; Contribution Number xx). SCEC is funded by the National Science Foundation (NSF) Cooperative Agreement EAR-1600087 and the U.S. Geological Survey (USGS) Cooperative Agreement G17AC00047. We thank Robert W. Graves for providing the source models and Fabio Silva for providing the station records of the 2014 La Habra earthquake.

Chapter 3, in full, is a reformatted version of a paper under revision for publication: Hu, Z., K. B. Olsen, and S. M. Day (2021). "Calibration of the Near-surface Seismic Structure in the SCEC Community Velocity Model Version 4." The dissertation author was the primary investigator and author of this paper.

Tables and Figures

Table 3.1: Simulation parameters used for the deterministic ground motion simulations of the 2014 La Habra earthquake.

Domain				
Length	147.840 km			
Width	140.400 km			
Depth	58.000 km			
Continue of a continue	-118.9774168,			
Southwest corner	33.9093124			
Spatial resolution				
Maximum frequency	5 Hz			
Minimum V_S	500 m/s			
Points per minimum wavelength	5			
Grid discretization	20/60 m			
Number of cells	25,092,587,520			
Number of GPU processors	960			
Wall-clock time	1.5 hr			
Temporal resolution				
Time discretization	0.001 s			
Simulation time	120 s			
Number of timesteps	120,000			

 Table 3.2: Rock site information

site_name	Lon (°)	Lat (°)	R_{hypo} (km)	<i>V_S</i> (m/s)	V _{S30} (m/s)	Elevation (m)	
CISRN	-117.79	33.83	17.53	1908.44	351.90	212.32	
CIQ0029	-117.75	33.73	27.87	2163.35	293.50	94.84	
CE13220	-117.75	33.68	31.99	2090.55	351.90	70.28	
CISTG	-117.77	33.66	32.61	1980.29	351.90	47.53	
CE13441	-117.78	33.66	32.74	1934.54	447.28	45.87	
CIPLS	-117.61	33.80	33.36	2234.93	351.90	1215.81	
CE24399	-118.06	34.22	36.28	2597.01	710.10	1724.74	
CIMWC	-118.06	34.22	36.28	2596.96	710.10	1727.73	
CIQ0034	-117.66	33.69	36.56	2289.27	293.50	324.50	
CIQ0009	-117.71	33.61	41.12	1885.40	351.90	106.23	
CIQ0022	-117.50	33.77	43.52	2425.56	351.90	362.41	
CIBFS	-117.66	34.24	44.01	2270.57	710.10	1301.77	
NP707	-117.45	33.85	45.57	2913.91	293.50	407.88	
CIQ0026	-117.57	33.64	45.83	2529.13	228.20	375.70	
CIQ0005	-117.77	33.53	46.38	1961.18	710.10	42.60	
CISDD	-117.66	33.55	48.13	1923.53	351.90	122.19	
CIQ0038	-117.43	33.73	51.38	2926.22	293.50	416.98	
CE13916	-117.32	33.90	56.71	2893.67	518.90	522.59	
CITA2	-117.68	34.38	56.88	2381.10	351.90	2258.42	
CILPC	-117.55	34.32	56.89	1970.65	351.90	1344.56	
CICJM	-117.42	34.27	61.30	2404.97	228.20	1615.85	
CE13080	-117.25	33.97	63.28	2607.63	518.90	542.10	
CE23958	-117.65	34.44	63.85	2093.92	447.28	1236.29	
CIQ0035	-118.20	34.47	66.03	2428.36	710.10	864.55	
CE13096	-117.27	33.70	66.46	4105.94	518.90	426.84	
CE23292	-117.54	34.43	66.98	1807.64	710.10	1211.92	
CIIPT	-117.29	34.20	67.45	2552.72	228.20	945.86	
CIPER	-117.21	33.86	67.67	2880.41	518.90	467.03	
CIQ0028	-117.18	33.83	70.30	3197.89	518.90	461.22	
CIQ0013	-118.06	34.54	70.31	2620.60	518.90	859.30	
CE13927	-117.17	33.92	70.31	2377.65	351.90	494.08	
CISOF	-117.56	33.37	70.35	2333.99	351.90	16.09	
CILUG	-117.37	34.37	72.20	2080.27	513.69	1136.43	
CISBPX	-117.24	34.23	73.34	2310.65	293.50	1872.13	
CE13924	-117.13	33.75	76.98	4161.26	351.90	486.31	
CIQ0049	-117.13	34.20	80.69	2184.64	710.10	1661.03	
CIBBS	-116.98	33.92	88.03	1639.46	518.90	782.79	
CE12919	-116.97	33.93	88.77	1559.19	518.90	795.50	
CIQ0020	-116.95	33.96	90.66	1588.16	468.40	859.36	

Table 3.3: Average FAS biases for all three components for various models.

Model	Soil sites				Rock sites			
Widdel	East-west	North-south	Vertical	Average	East-west	North-south	Vertical	Average
CVM-S*	0.034	0.044	0.009	0.029	-0.277	-0.261	-0.136	-0.225
$CVM-S + 350 \text{ m}^*$	0.040	0.048	0.009	0.033	-0.171	-0.153	-0.138	-0.154
$CVM-S + 700 \text{ m}^*$	0.055	0.062	0.018	0.045	-0.020	-0.015	-0.087	-0.041
$CVM-S + 1000 \text{ m}^*$	0.065	0.073	0.020	0.053	0.048	0.055	-0.055	0.016
$CVM-S + 350 \text{ m}$ $+ Q_S = 0.05V_S^{\dagger}$	-0.039	-0.027	-0.091	-0.052	-0.064	-0.052	-0.156	-0.091
$CVM-S + 1000 \text{ m}$ $+ Q_S = 0.15V_S^{\dagger}$	0.085	0.091	0.061	0.080	-0.135	-0.120	-0.105	-0.120

 $^{^*}$ $Q_S = 0.1V_S$; $Q_P = 2Q_S$ † $Q_P = 2Q_S$



Figure 3.1: Simulation region for the La Habra event (rectangle) and locations of 259 strong ground motion stations (circles represent soil sites with surface $V_S < 1000$ m/s and red triangles represent rock sites with surface $V_S >= 1000$ m/s). The named sites (triangles with black edge) are selected for further comparisons in Figure 12. The star depicts the epicenter of the La Habra earthquake.

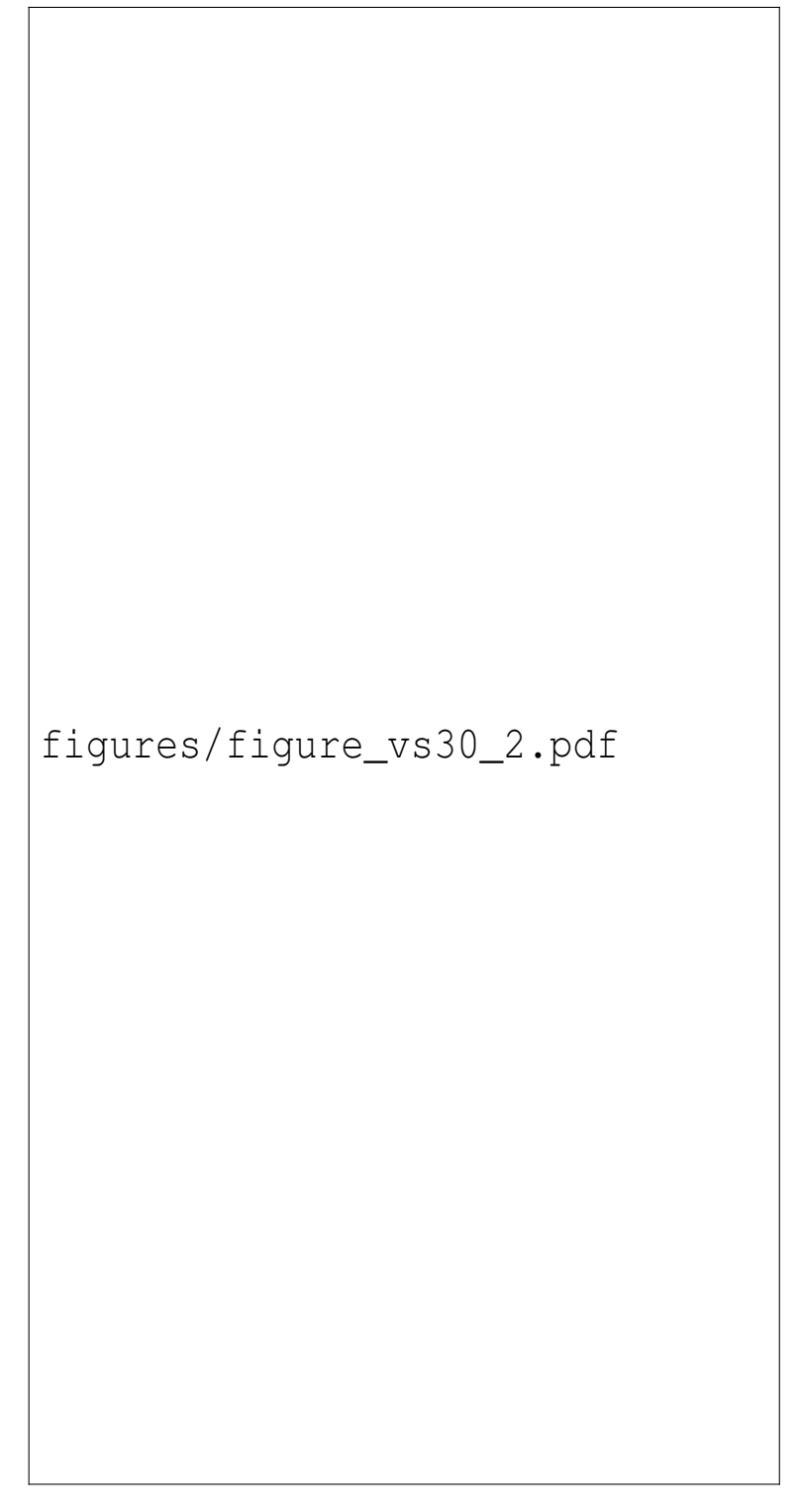


Figure 3.2: Description of the source model used in this study. (a) Total moment on the fault. The contours represent rupture time at a 0.4 s interval starting from 0. (b) and (c) represent the sum of the moment rates for all subfaults and the Fouerier amplitude spectrum, respectively.

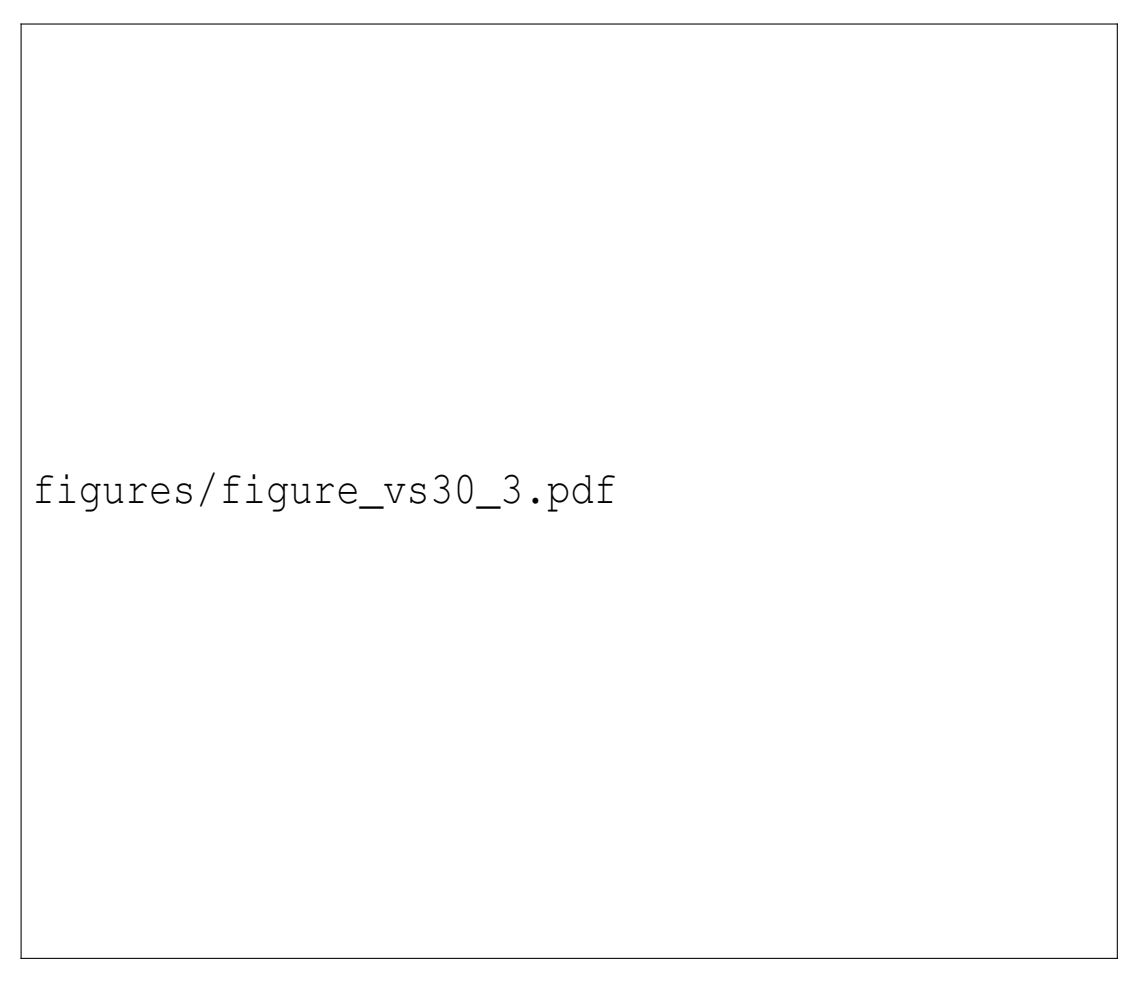


Figure 3.3: (a) Top 150 m and (b) 0-4000 m V_S profiles at the 259 stations. The black and red curves represent rock (surface $V_S >= 1000$ m/s) and soil (surface $V_S < 1000$ m/s) sites, respectively. The darker curves denote the sites with farther distance from the source.

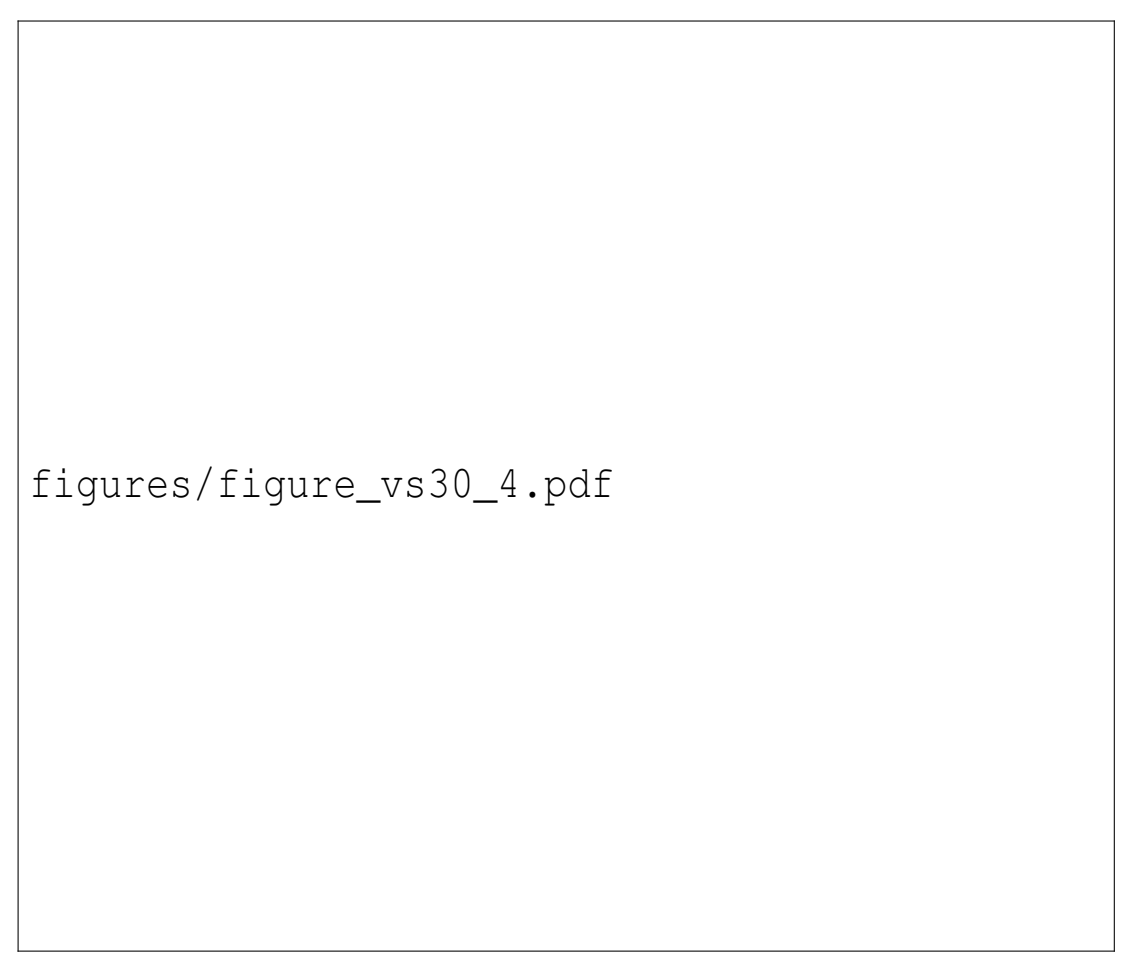


Figure 3.4: FAS derived from the records (black) and CVM-S (blue) for the (a) east-west component, (b) north-south component and (c) vertical component. The left and right columns represent soil sites with surface V_S smaller and larger than 1000 m/s, respectively. The solid line is the median of FAS over the site group, the narrow band is the 95% confidence interval of the median, and the wide band depicts the standard deviation centered at the median.

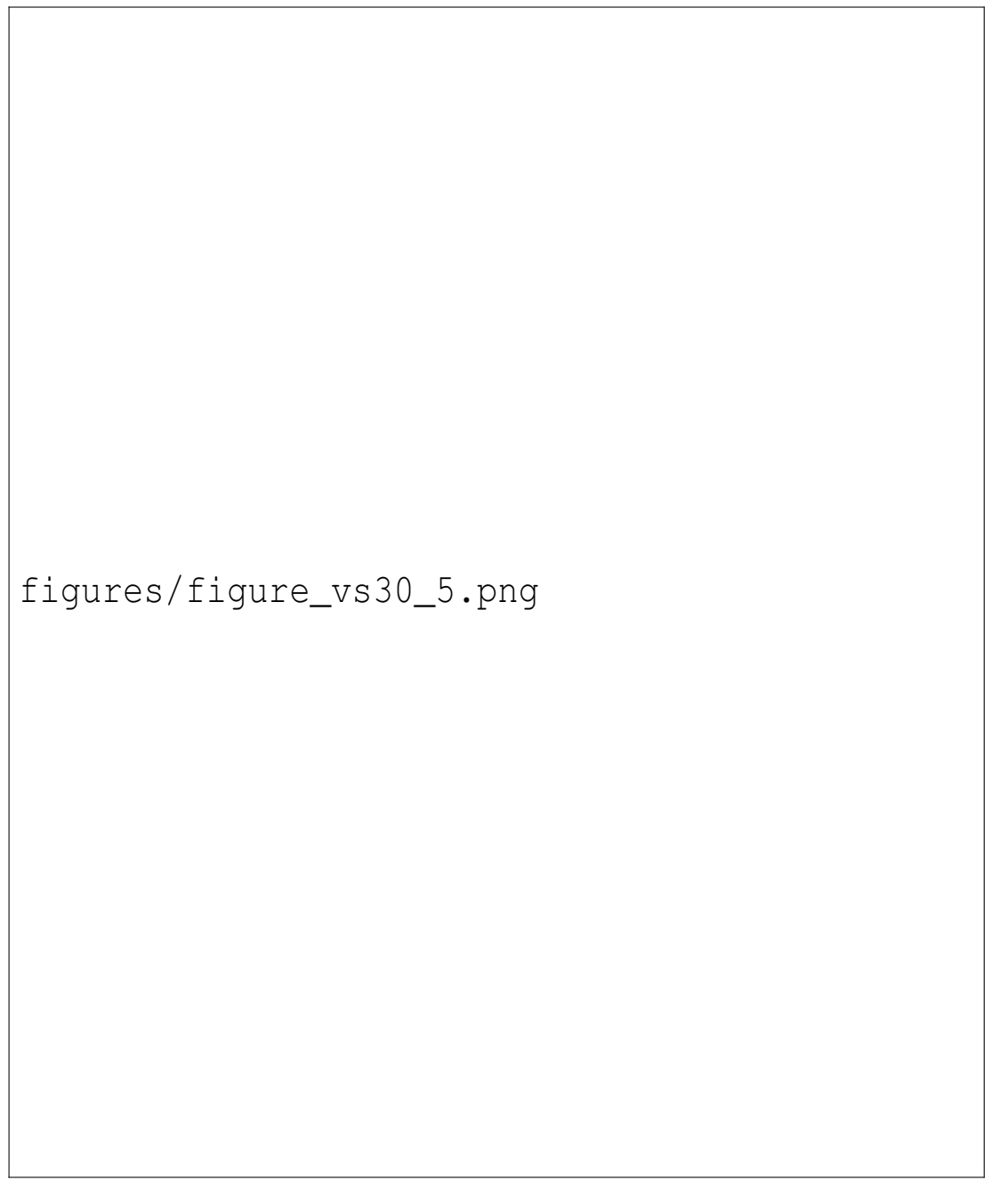


Figure 3.5: (a) Surface V_S extracted from CVM-S, and (b) V_{S30} from Thompson (2018) in our model domain (values in the left bottom corner are not available). The star denotes the epicenter.



Figure 3.6: Representative V_S profiles for (a) soil sites and (b) rock sites from CVM-S. The thick black curves depict the averaged velocity profiles for all 220 soil and 39 rock sites directly extracted from CVM-S. The thin lines show the V_S refinement resulting from our proposed method for different z_T depths between 200 m and 1500 m. The dashed curve shows the V_S profile calculated using our preferred z_T value of 1000 m.



Figure 3.7: The SH1D response for the refined profiles using various z_T depths for average (a) soil and (b) rock sites, divided by the response obtained with the averaged soil and rock profiles from CVM-S.



Figure 3.8: Bias of FAS for the two horizontal components averaged over all (a) soil and (b) rock sites for CVM-S at all 259 stations, superimposed with the corresponding SH1D response. The black curves denote CVM-S and other labeled curves represent refinements to various depths using SH1D results.

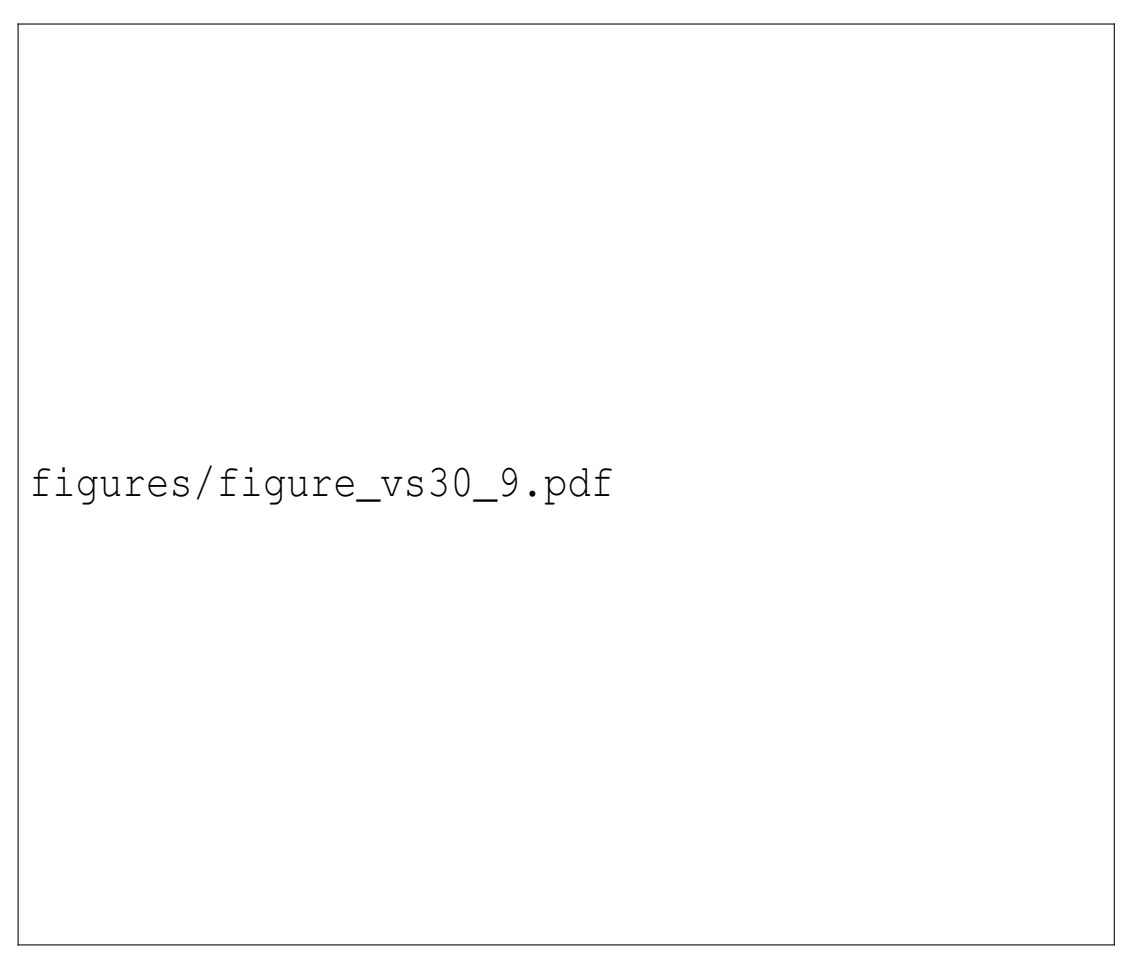


Figure 3.9: Bias of FAS on the (a) east-west, (b) north-south and (c) vertical components, calculated from 3D simulations in CVM-S and with V_S refinements of 350 m, 700 m, and 1000 m. A positive (negative) value depicts overprediction (underprediction). The left (right) column shows soil (rock) sites. The solid line is the median of FAS, where the narrow band is the 95% confidence interval of the median, and the dashed lines depict the standard deviation centered at the median.



Figure 3.10: Maps of interpolated log10-based FAS bias between four 3D models and data: (a) CVM-S, and CVM-S with refinements of (b) 350 m, (c) 700 m and (d) 1000 m, calculated from the synthetics and records at 259 stations. The warm (cool) colors represent overprediction (underprediction). The circles (triangles) depict soil (rock) sites. Note the log10-based colorbar.

figures/figure_vs30_11.png

Figure 3.11: Maps of interpolated log10-based FAS bias for two 3D CVMs and data. (a) CVM-S with refinement depth of 350 m and $Q_S = 0.15V_S$, and (b) CVM-S with refinement of 1000 m and $Q_S = 0.05V_S$. Warm (cool) colors represent overprediction (underprediction). Circles depict soil sites and triangles show rock sites.



Figure 3.12: Cumulative kinetic energy and Fourier velocity spectra at six rock sites. The subtitles show the names of the sites and their hypocentral distance.

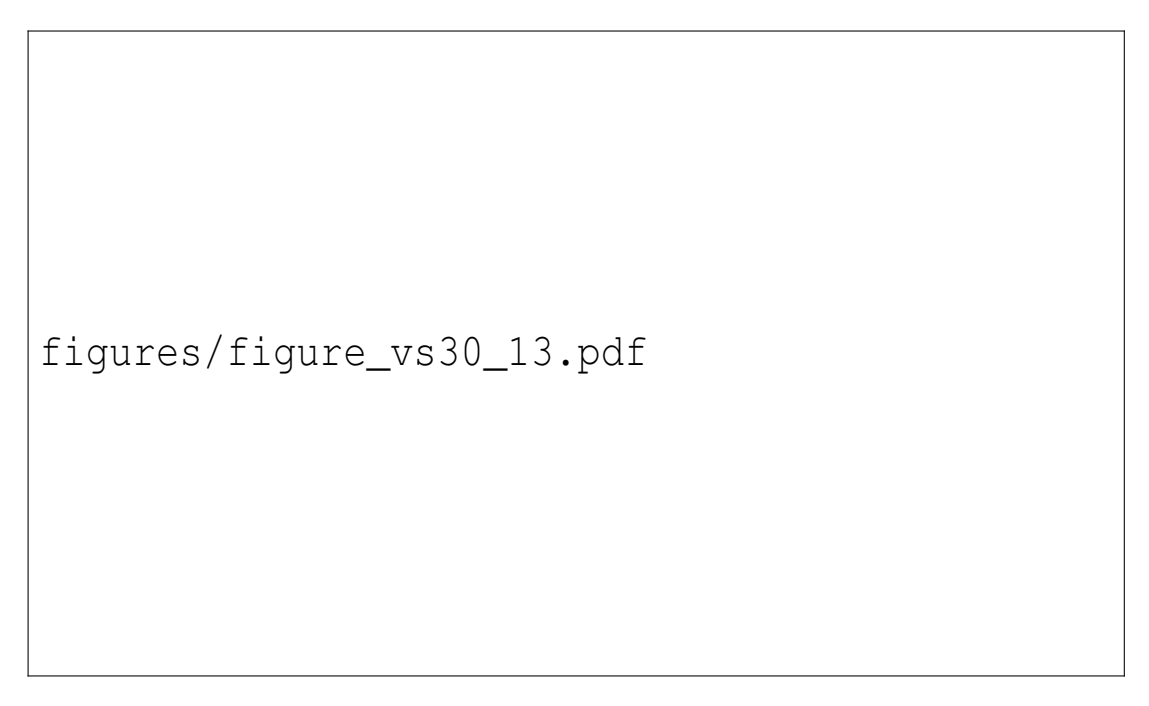


Figure 3.13: Rock site V_S profiles (defined as surface V_S >=1000 m/s) from CVM-S, and CVM-S and CVM-H with (default) Ely *et al.* (2010) GTL refinement depth of 350 m.

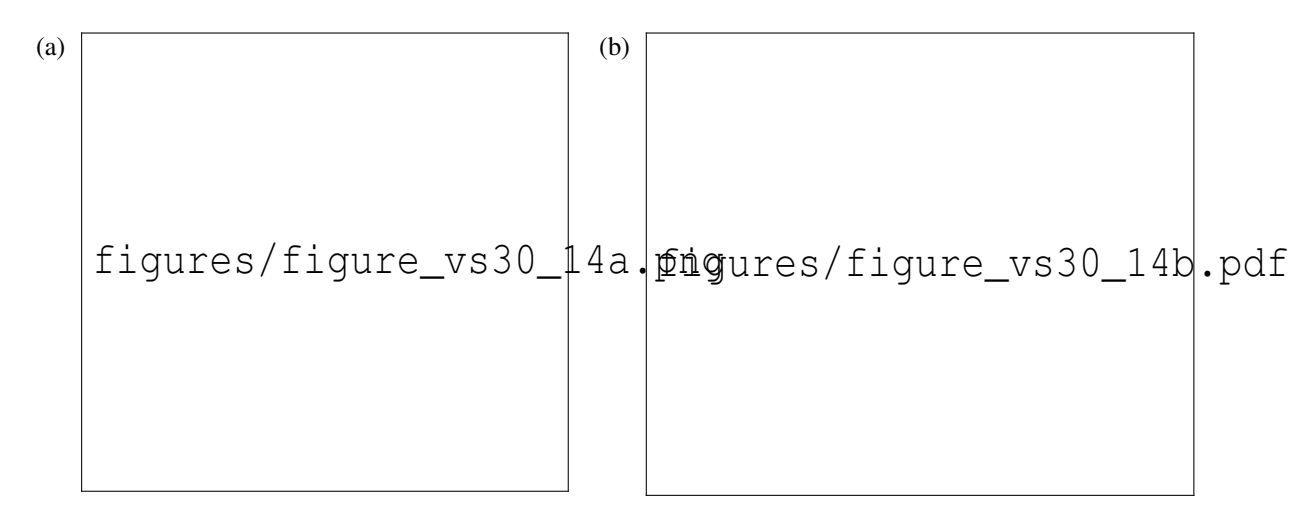


Figure 3.14: (a) V_S profile sample locations in California. Triangles denote rock sites and circles denote soil sites, and (b) extracted V_S profiles. The top panel zooms into the top 500 m.



Figure 3.15: Bias of FAS of the (a) east-west, (b) north-south and (c) vertical component, calculated from 3D simulations in CVM-S with V_S refinement depths of 350 m and 1000 m along with attenuation models $Q_S = 0.05V_S$, $Q_S = 0.1V_S$, and $Q_S = 0.15V_S$. A positive (negative) value means overprediction (underprediction). The left (right) columns show soil (rock) sites. The solid line is the median of FAS, where the narrow band is the 95% confidence interval of the median, and the dashed lines depict the standard deviation centered at the median.



Figure 3.16: Average FAS bias for frequencies between 0.15-1 Hz at rock sites plotted as a function of site surface V_S for (a) three-component average, (b) east-west, (c) east-west and (d) vertical components. The shades represent 95% confidence intervals estimated using bootstrap.

Supplementary Materials

This supplement includes.

Chapter 4

Calibration of the Near-surface Seismic Structure in the SCEC Community Velocity Model Version 4

The near-surface seismic structure (to a depth of about 1000 m), particularly the shear-wave velocity (Vs), can strongly affect the propagation of seismic waves, and therefore must be accurately calibrated for ground motion simulations and seismic hazard assessment. The Vs of the top 30 m of the crust (Vs30) is often well-characterized from borehole studies, geotechnical measurements, and water wells, while the velocities of the material deeper than about 1000 m are typically determined by tomography studies. However, the material parameters between these two regions are typically poorly constrained due to lack of data constraints. A widely-used method for incorporating the near-surface earth structure is incorporated in the Southern California Earthquake Center (SCEC) Community Velocity Models (CVMs) by interpolating Vs from Vs30 measurements to the S-wave velocity at 350 m (Ely et al., 2010). However, our 3D simulations of the 2014 M5.1 La Habra earthquake in the Los Angeles area using the SCEC CVM-S4.26.M01 model significantly underpredict low-frequency (< 1 Hz) ground motions at

rock sites for the Ely *et al.* (2010) method. On the other hand, extending the Vs30-based refinement of the shallow velocities down to a depth of about 1000 meters improves the fit between our synthetics and seismic data at rock sites considerably, without compromising the fit at soil sites. We recommend that our proposed near-surface velocity refinement at rock sites down to about 1000 meters be incorporated in CVM-S4.26M01, as well as considered for other CVMs.

4.1 Introduction

4.2 Numerical Approach

Data and Resources

The UCVM program used to extract velocity meshes can be obtained from SCEC on https://github.com/SCECcode/UCVMC (last accessed 12/2020). The simulations were performed on Summit at the Oak Ridge Leadership Computing Facility in Tennessee. Most of the data-processing work was done using Python and the Generic Mapping Tools package (https://www.generic-mapping-tools.org, last accessed 04/2021).

Acknowledgements

This research was supported through the U.S. Geological Survey External Program (award #G19AS00021), as well as the Southern California Earthquake Center (SCEC; Contribution Number xx). SCEC is funded by the National Science Foundation (NSF) Cooperative Agreement EAR-1600087 and the U.S. Geological Survey (USGS) Cooperative Agreement G17AC00047. We thank Robert W. Graves for providing the source models and Fabio Silva for providing the

station records of the 2014 La Habra earthquake.

Chapter 4, in full, is a reformatted version of a paper currently being prepared: Hu, Z. and Olsen, K.B. (2021), 0-5 Hz Deterministic 3D Ground Motion Simulations for the 2014 Mw 5.1 LaHabra Earthquake. The dissertation author was the primary investigator and author of this paper.

Tables and Figures

Supplementary Materials

This supplement includes.



Figure 4.1: (a) V_S profile sample locations in California. Triangles denote rock sites and circles denote soil sites, and (b) extracted V_S profiles. The top panel zooms into the top 500 m.

Chapter 5

Modeling of Empirical Transfer Functionswith 3D Velocity Structure

Empirical transfer functions (ETFs) between seismic records observed at the surface and depth represent a powerful tool to estimate site effects for earthquake hazard analysis. However, conventional modeling of site amplification, with assumptions of horizontally polarized shear waves propagating vertically through 1D layered homogeneous media, often poorly predicts the ETFs, particularly, in which large lateral variations of velocity are present. Here, we test whether more accurate site effects can be obtained from theoretical transfer functions (TTFs) extracted from physics-based simulations that naturally incorporate the complex material properties. We select two well-documented downhole sites (the KiK-net site TKCH05 in Japan and the Garner Valley site, Garner Valley Downhole Array, in southern California) for our study. The 3D subsurface geometry at the two sites is estimated by means of the surface topography near the sites and information from the shear-wave profiles obtained from borehole logs. By comparing the TTFs to ETFs at the selected sites, we show how simulations using the calibrated 3D models can significantly improve site amplification estimates as compared to 1D model predictions. The primary reason for this improvement in 3D models is redirection of scattering from vertically

propagating to more realistic obliquely propagating waves, which alleviates artificial amplification at nodes in the vertical-incidence response of corresponding 1D approximations, resulting in improvement of site effect estimation. The results demonstrate the importance of reliable calibration of subsurface structure and material properties in site response studies.

5.1 Introduction

Details of how ground shaking is affected by near-surface soil properties can help reduce the uncertainty in stochastic or empirical ground-motion models, which are important components of seismic hazard calculations. Transfer functions (TFs) are widely used to quantitatively represent site response by computing the spectral ratio of ground motions between site and reference locations in the frequency domain (e.g., Shearer and Orcutt, 1987; Steidl, 1993; Field and Jacob, 1995; Steidl *et al.*, 1996; Bonilla *et al.*, 2002). Assuming that the reference site, while sharing, approximately, the same path and source with the site of interest, is largely unaffected by site effects, the spectral ratio provided by the TF isolates the site response (Borcherdt, 1970). Two types of reference sites, both typically rock, have been proposed: a surface site or a downhole recording (used with the corresponding surface site). The surfacedownhole record pair is valuable for ensuring close proximity of the reference motions at the downhole sensor, ideally located in bedrock, whereas, it may be difficult to find an appropriate reference outcrop site within close distance to the soil site. In this article, we will only analyze TFs computed using surface-downhole site pairs.

The accuracy of site response estimates depends on the accuracy of the subsurface model used, and this is usually assumed to be controlled by the uncertainty in the site properties, in particular, the shear-wave velocity, V_S (e.g., Barani *et al.*, 2013; Griffiths *et al.*, 2016). V_S is the most important parameter for conventional 1D modeling of the TF, in which it is assumed that surface (and subsurface) motion consists of horizontally polarized plane S waves propagating

through a stack of homogeneous layers (e.g., Kramer, 1996). This modeling procedure (SH1D) ignores the lateral complexity of the often heterogeneous geology and subsurface structure and is, therefore, not able to include potential 2D and 3D amplification effects in the observations (e.g., Roten *et al.*, 2008; Thompson *et al.*, 2012). Zhu *et al.* (2018) performed numerical analysis on 2D basins and found that a constant spectral aggravation factor (Chávez-García and Faccioli, 2000), which quantifies the discrepancy between 1D and 2D/3D models, is insufficient to identify basin effects, especially, in close-to-edge regions of shallow basins. Both observations and analytical solutions suggest that 1D models lack an estimate of spatial variability, caused by complex wave propagation such as basin amplification, surface-wave generation, and scattering, and are, therefore, unable to capture spatial correlations, which may be important for understanding risk, especially, to regional-scale infrastructure (e.g., Olsen and Schuster, 1995; Boore, 2004). Although, recent approaches have attempted to reduce velocity uncertainties in site effect estimation (Matavosic and Hashash, 2012; Teague *et al.*, 2018), these methods either require prohibitively complex processing or are developed for specific cases only.

It is impractical to constrain subsurface structure over a wide region to the resolution (on the order of meters to tens of meters) required for accurate ground-motion estimation to high frequencies (e.g., 10 Hz). Instead, some studies choose to use simple proxies, based on broad site classes to supplement estimates of soil properties and site spatial characteristics, for example, the National Earthquake Hazards Reduction Program (NEHRP) soil classification (BSSC, 2003; Akkar and Bommer, 2010) or a weighted average of V_S in the uppermost 30 m (V_{S30} , e.g., Abrahamson and Silva, 2008; Idriss, 2014). Thompson *et al.* (2012) proposed a scheme to classify surface-downhole site pairs by the extent of interevent variability and goodness of fit between 1D modelling and empirical site response, which can be used to calibrate the constitutive models and guide specific site studies. Despite the use of these characterizations in some generic seismic hazard estimates, for instance, via ground-motion prediction equations, recent work has pointed out the importance of considering site-to-site amplification variability (Atkinson and

Boore, 2006; Atik *et al.*, 2010). These studies show that, even within a single NEHRP or V_{S30} class, the variability of site amplification and spatial correlations is strong enough to contribute significant uncertainty in ground-motion estimates.

In this chapter, we propose a method to constrain the near-surface properties using surface topography and perform highresolution 3D numerical simulations to investigate the uncertainty in site response modeling. The simulations naturally take advantage of 3D geotechnical information and are able to incorporate complicated spatially varying amplification effects. We use two downhole array sites, namely the Garner Valley Downhole Array (GVDA) in California and the TKCH05 site from the Kiban–Kyoshin network (KiK-net) surface-downhole pairs in Japan, where detailed in situ constraints of site seismic properties (e.g., V_S and layer thicknesses) and abundant earthquake records are available, for our analysis. Both borehole sites have welldocumented geological structure data, and previous studies have showed that SH1D modeling poorly predicts the ground motions without adjustments of subsurface properties or recalibration of constitutive models. Thompson et al. (2012) found low interevent variability and poor fit using SH1D modeling for the site TKCH05, due to omission of spatial variability around the site that scatters the downgoing waves and reduces pseudoresonance. They found that no satisfactory fit could be achieved by adjusting the velocity profile, whereas Tao and Rathje (2020) showed that modification in the top 20 m can significantly improve the site response estimate for the outcrop TF (spectral ratio between two surface sites). Bonilla et al. (2002) studied the wave propagation at GVDA and reported significant S-to-P conversions that led to misfit in prediction of the empirical TF (ETF; see Section 5.3) by horizontal-to-vertical spectral ratios. Teague et al. (2018) applied the Toro randomization model (Toro, 1995) with the spectral analysis of surface waves method, to obtain the site signature with the best match of the ETF and the theoretical TF (TTF); however, this approach suffers from the nonunique nature of inverting V_S profiles.

5.2 Data

Dependent on the strength of the input motion, site amplification and deamplification can be caused by a combination of linear and nonlinear effects. Here, we focus on linear site effects, and reserve the nonlinear analysis for subsequent research endeavors. To limit our analysis to linear ground motions, we exclude records with maximum surface accelerations larger than 0.1g (e.g., Beresnev and Wen, 1996). For each of the two site selections, we randomly picked 36 events of various azimuth and distance to the site that meets this criterion, with a minimum signal-to-noise ratio of five in their records. The goodness of fit between TTFs and ETFs from recordings is described by the variance reduction (VR) as follows:

$$VR = 1 - \frac{\sum_{i=1}^{n} [TTF(f_i) - ETF_{med}(f_i)]^2}{\sum_{i=1}^{n} [ETF_{med}(f_i)]^2}$$
(5.1)

in which n is the number of frequencies at which the ETFs and TTFs are computed, and ETF med is the median of the ETFs from the events that we selected. We evaluate a set of linearly spaced frequencies between 0.5 and 10 Hz, with the lower limit determined by the noise level of the data, and the upper limit from the resolution of our simulations. The VR ranges within $[-\inf, 1]$, in which VR = 1 means a perfect match, and smaller values indicate poorer fit.

5.3 TFs

We compute TFs between surface and downhole locations as follows:

$$TF = \frac{G_s(f)}{G_d(f)} \tag{5.2}$$

in which $G_s(f)$ and $G_d(f)$ are the root mean squares of the Fourier amplitude spectra of horizontal accelerations at the surface and downhole locations, respectively. It is worthwhile to note that the downhole recordings include the upgoing incident wavefield as well as downgoing waves that are reflected back from the free surface. This phenomenon complicates the wavefields recorded at downhole sites, and, therefore, the use of surface-downhole pairs to study site response. For records obtained at depths shallower than 200 m, as in this study, the upgoing and downgoing pulses overlap in the records, with differences in arrival times as small as 0.2 s, complicating a separation of the two contributions in the presence of extended source duration and site response (Shearer and Orcutt, 1987). For example, Bonilla *et al.* (2002) found from simulations at the GVDA site using the f -k method that the downgoing wave effect is predominant above the soil-bedrock interface and strongly degraded below that depth. Because it is almost impossible to eliminate downgoing waves from the records, we include the total wavefields at the surface and downhole sites, when calculating the TFs for both synthetics and records.

Our procedure for processing the recorded time series is similar to that documented in Tao and Rathje (2019). First, we collected acceleration time series at the surface and downhole accelerometers. Second, a fifth-order Butterworth filter, with a passband of 0.5–12 Hz, was applied to the demeaned and detrended accelerations, in which signal at frequencies below 0.5 Hz was discarded to minimize the contribution from low-frequency noise interference. Third, a second-order polynomial baseline correction was applied to the observed displacement time series, obtained by integrating the accelerations twice. Then, the ETFs were obtained as the ratio of the Fourier spectral amplitude between the surface and downhole acceleration time series for all the events. We further smoothed the TFs using the Konno–Ohmachi smoothing window in the frequency domain (Konno and Ohmachi, 1998). Although, not necessary for the synthetics, we applied the preprocessing (steps 2 and 3) to both synthetics and data for consistency.

5.4 Model Construction

It is reasonable to assume that, in the vicinity of a site of interest, bedrock depth varies in accordance with surface topography. In such models, sites located in a mountainous area have near-zero bedrock depth, whereas, sites in valley regions are characterized by larger depths to bedrock. Under this assumption, our 3D mesh is generated by mapping the topography to bedrock depth, with the constraints from borehole logging measurements. Oftentimes, bedrock depth increases rapidly from the edge toward the center of a sedimentary valley and approaches a maximum near the center of the valley, suggesting that depth to bedrock in a valley can be estimated using the topographic signature from digital elevation models. Gallant and Dowling (2003) proposed an algorithm that operates at multiple scales and combines topographic elevations into a single continuous multiresolution index of valley bottom flatness (MRVBF). Values of MRVBF below 0.5 represent areas with the steepest topography, values between 0.5 and 1.5 relate to the steep areas with few flat valley bottoms, and larger MRVBF values indicate broader and flatter valley bottoms. Here, we adopt the MRVBF technique and used the same threshold value (1.5) as in Gallant and Dowling (2003), to discriminate valley and mountainous regions. The quantitative relationship between the bedrock depth (D) and MRVBF values are assumed to obey a logarithmic formula:

$$D = max(0, \quad D_0 * log_{10}(\frac{MRVBF}{MRVBF_t}))$$
(5.3)

in which $MRVBF_t$ is the threshold MRVBF value (here, 1.5), and D_0 is a coefficient, which is calculated by substituting the MRVBF value and bedrock depth at the borehole site into the borehole equation, that is, $D_0 = D_{borehole}/log_{10}(\frac{MRVBF_{borehole}}{MRVBF_t})$.

In addition to the modifications of the velocity model from the MRVBF method, we explore the extent to which scattering effects from statistical distributions of near-surface smallscale heterogeneities (SSHs) can improve site effect estimation. Previous studies using 1D modeling show that including SSHs may improve the prediction of ETFs, likely by weakening the downgoing wave effects (Nour *et al.*, 2003; Thompson *et al.*, 2012). Here, we use guidance from published studies on spectral coloring of Gaussian random numbers with von Karman spatial correlation functions for characterizing the statistics of heterogeneities (see Appendix A; as well as, e.g., Frankel and Clayton, 1986; Withers *et al.*, 2019). We use a Hurst number of 0.05, a correlation length of 100 m, a standard deviation of 5%, and a horizontal-to-vertical anisotropy of five, as constrained from sonic borehole logs in the Los Angeles basin by Savran and Olsen (2016). We include SSHs with these parameters, when generating TFs at our two selected locations, whereas, the sensitivity of the TFs to variation in the parameters is explored in the Discussion section.

5.4.1 Numerical simulations

Our goal to quantify the effects of 3D Earth structure on highfrequency (<10 Hz) TFs, using 3D modeling, is computationally challenging. We use the parallel and scalable discontinuous—mesh velocity—stress staggered-grid finite-difference code AWP-ODC-DM (Olsen, 1994; Cui *et al.*, 2010; Nie *et al.*, 2017) to simulate the site response. One-dimensional TTFs are computed under the SH1D assumption, in which the model consists of a stack of homogeneous layers, to provide a point of comparison for the 3D models. The model definition for the 3D TTF computation is more complicated. We include the effects of frequency-dependent attenuation using the model:

$$Q(f) = \begin{cases} Q_0 \times f_{\gamma}, & f > 1 \\ Q_0, & f \le 1 \end{cases}$$

$$(5.4)$$

in which Q_0 is a frequency-independent constant attenuation proportional to the velocity, and γ is a power-law exponent describing the attenuation above 1 Hz (Withers *et al.*, 2015). Here, we

adopt area-specific parameters suggested in the literature; for GVDA, we use $Q_{S,0} = 0.05 \times V_S$ (V_S in meters per second), $Q_{P,0} = 2 \times Q_{S,0}$, and $\gamma = 0.6$ (Withers *et al.*, 2015; for southern Calfornia), and for TKCH05, we use a model for $Q_{P,0} = Q_{S,0} = Q_0$, given by

$$Q_0 = \begin{cases} 60, & V_S \le 600\\ 100, & 600 < V_S \le 1100\\ 150, & 1100 < V_S \le 2100\\ 200, & 2100 < V_S \le 3200\\ 300, & V_S > 3200 \end{cases}$$

$$(5.5)$$

in which V_S is in meters per second, from the Japan Seismic Hazard Information Station (J-SHIS) and $\gamma = 0.2$, following the study by Nakajima et al. (2013). We discretize the velocity models using two partitions in our discontinuous mesh, with grid spacings small enough to resolve the minimum V_S wavelengths (20 m and 14 m for the GVDA and TKCH05 cases, respectively), anywhere in the model with, at least, five points. In our simulations, the surface recordings at a neighboring outcrop site are deconvolved from its local subsurface property layers, up to the bottom of the simulation domain; the resulting three-component acceleration time series (converted to body forces in AWP-ODC-DM) are then distributed on the entire bottom surface of the computational domain, to generate a oneway upward propagating plane wave. We verified that such vertical-incident plane wave sources are reasonable approximations, considering our shallow simulation domains (0.4 km and 1 km deep at GVDA and TKCH05, respectively), as well as earthquake hypocenters at depths of 10 km+ and distances of tens of kilometers. We used an elastic boundary condition at the bottom grid boundary, which is transparent to downgoing waves, to avoid artificial resonance of the soil column (Roten et al., 2012). We part from the common way of placing the model base at the downhole site and have the input motion as the downhole motion, due to our boundary conditions. We perform the numerical simulations on

the Oak Ridge National Laboratory Summit supercomputer, in which each of our simulations with the 3D model at TKCH05, including 64 million cells, requires a wall-clock time of 100 min on 32 graphic processing units for 750,000 timesteps. Similar computational requirements are needed for the 3D GVDA simulations.

5.5 GVDA

The GVDA is located in a seismically active region of California, 7 km from the San Jacinto fault and 35 km from the San Andreas fault (see Fig. 5.1; Archuleta *et al.*, 1992). The site is situated in a narrow valley within the Peninsular Ranges Batholith (Bonilla *et al.*, 2002), 23 km east of Hemet and 20 km southwest of Palm Springs, California. The near-surface stratigraphy beneath GVDA consists of extensive lake-bed alluvium and decomposed crystalline rocks (Hill, 1981). Soft silty and clayey sands makes up the top 18-25 m across the site (Steidl *et al.*, 1996), followed by 50–60 m thick, decomposed, and weathered granite down to about 64-87 m, as constrained by seismic downhole testing and shallow and deep P–S velocity suspension logging (Gibbs, 1989; Steller, 1996). The GVDA site is equipped with multiple downhole accelerometers, at depths of 15, 22, 50, and 150 m that are capable of measuring accelerations from 3×10^{-6} to 2.0g below 100 Hz. The 150 m deep accelerometer is the only downhole sensor that penetrates the granitic rock, which is used to compute TTFs in this study.

To be able to resolve frequencies up to 10 Hz at the GVDA site, we generated a mesh of size 4 km × 4 km × 0.4 km (length × width × depth), with mesh properties compressional wave velocity (V_P), V_S and density from the 3D Community Velocity Model (CVM) S4.26.M01, which is developed and maintained by the Southern California Earthquake Center (SCEC; Small *et al.*, 2017). The borehole logs show V_S of the near-surface soft soils between 180 and 220 m/s, with the value of V_S smaller than 200 m/s only at depths between 1.4 and 2.8 m (Steller, 1996). The minimum velocity in our model was truncated at 200 m/s, which is about the average of the

top 4 m, resolving frequencies up to 10 Hz, with, at least, five points per minimum S wavelength, using a smallest grid spacing of 4 m. The SCEC CVM S4.26.M01, however, fails to resolve the 3D Garner Valley structure to the accuracy required by our analysis, and we use the MRVBF method to describe the depth to bedrock instead.

At every surface location, we first compute the MRVBF value and bedrock depth, as described in the Numerical simulations section. We then force the V_P , V_S , and densities above the bedrock to be the same as those in the measured borehole log, while keeping the seismic velocities and densities unchanged in the bedrock. Figure 5.2 illustrates how we estimate bedrock depth from the MRVBF values, using surface topography. The deeper parts of the valley are represented by larger MRVBF values. The areas with MRVBF smaller than the threshold value at 1.5 are shown in dark shading, corresponding to steeper terrain. The borehole site GVDA, at the center of the region, has a MRVBF value of 5.8 and bedrock depth of 64 m, consistent with the borehole log from Gibbs (1989). The 3D geometry inferred from the spatially varying bedrock depth is shown in the left panels of Figure 5.3, compared to the original borehole profile in the right panel.

Although we computed the ETFs for all the selected 36 events (Table 5.1 and Fig. S5.1), only one event (ID = 33) was used to generate the upgoing waves in the simulations and to compute the TTF. The selection of event ID 33 was arbitrary for two reasons: (1) the ETFs at GVDA show low interevent source variability, indicated by the narrow σ band in Figure 5.4, and (2) the modeling is constrained to linear wave propagation. The use of a realistic source allows straightforward extension to multiple sites, as well as to nonlinear analysis in the future. The source time function was obtained by deconvolving the surface recordings of this event at the neighboring outcrop site GVAR (see Fig. 5.1) to the maximum depth of our domain.

The TTFs and ETFs for GVDA are compared in Figure 5.4. The two-sigma scatter of all the ETFs is fairly narrow above 1 Hz and not sensitive to the azimuths and distances of the events, which implies that the ETFs are primarily determined by the site characteristics, and

confers greater predictive power on an ETF (and presumably also on a TTF). Although the peaks for the ETFs and both 3D and 1D TTFsgenerally occurnear thesame frequencies, the goodness of fit predicted from the 1D model (VR = 0.64) is significantly smaller compared to the 3D model (VR = 0.85). This result suggests that the shallow 3D structure contributes first-order effects to the local site amplification at GVDA (see Section 5.7).

5.6 TKCH05

The KiK-net strong-motion seismograph network in Japan provides, approximately, 700 sites, with pairs of surface and downhole seismographs installed that have recorded earthquakes with a wide range of magnitudes. KiK-net also provides geological and geophysical data, including velocity structure for each site, derived from borehole logs. Thompson et al. (2012) analyzed the interevent variability and goodness of fit between SH1D models and data at 100 sites from KiK-net, and identified some sites where the standard 1D site response analysis provided poor results. Among these sites, we targeted TKCH05, which is located in Honbetsu, Hokkaido, Japan, to investigate the contributions from its underlying 3D structure on site effects. Figure 5.5 shows the location of TKCH05, in a narrow valley surrounded by mountains. The large gradients of the surface topography at the valley boundaries suggest the presence of significant 3D variation of the bedrock interface below the valley. The stratigraphy at TKCH05 is, approximately, 6 m of soil and sandy gravel with $V_S = 140$ m/s, overlying tens of meters of sandstone over gravel stone and siltstone (see Fig. 5.6; National Research Institute for Earth Science and Disaster Resilience, 2019). Table 5.2 lists the events included in our analysis of the ETFs at TKCH05 (see Fig. S5.2 for their locations and time series), among which the event with an ID of 1 was selected to generate the incoming waves in our simulations. As we did at site GVDA, we deconvolved the surface records at the closest outcrop site, Fnet site URH, which is about 21.7 km away from TKCH05 to the domain bottom.

Figure 5.6 shows the downhole profile at TKCH05, and Figure 7a shows a comparison between the corresponding 1D TTF compared to the ETFs. The 1D TTF fails to match the frequency peaks and strongly overpredicts the amplifications at lower frequencies, producing a relatively low VR (VR = 0.35). We also considered the adjacent K-Net site HKD090, due to its proximity to TKCH05 (only 4 m relative distance), in our analysis. The available information from the measured V_S profile at HKD090 only extends to a depth of about 18 m, but, varies notably from those at TKCH05, considering the close distance. Because the top layers are as thin as 2 m, it is possible that the accuracy was degraded when the downhole logging measurements of travel time were converted to piecewise constant profiles. For this reason, we tested a simplified profile combining the two borehole logs, by replacing the TKCH05 V_S profile between 5 and 100 m, with an average value of 680 m/s. The adjustment reduces the strong discrepancy in shallow V_S values between the two borehole logs and retains the travel time from the bedrock to the surface. The SH1D model with the simplified profile produces a poorer fit to the ETF (VR = 0.181) than that obtained using the TKCH05 profile. Although, the simplified profile agrees better with the location of the second spectral peak of the ETF, the overall response compares less favorably to that obtained using the original profile due to larger amplitudes, especially at frequencies between 1 and 3 Hz.

Next, we extract our background 3D models at TKCH05 with a 1 km \times 1 km \times 1 km region, with the top boundary centered at TKCH05, from the Japanese national subsurface V_S model provided by J-SHIS. The J-SHIS model provides V_S and V_P and density with a horizontal spatial resolution of 1 km. Along the vertical direction, J-SHIS provides the depths of 33 layers with various thicknesses. Each layer is homogeneous and of increasing V_S with depth, ranging from 350 to 3400 m/s. Given the coarse horizontal resolution, the J-SHIS model is essentially 1D, with small stepwise discontinuities present close to the southern edge of the model (Fig. 5.8d). The bedrock depth was then estimated using the MRVBF method. The V_S below the downhole array is 1100 m/s, which increases to 1700 m/s at the bottom of our domain (Fig. 5.8).

Based on the surface V_S of 140 m/s, we interpolated the initial mesh to a grid spacing of $\Delta h = 2.5$ m in the top partition of the mesh, to ensure at least 5–6 points per minimum S wavelength. In the discontinuous mesh setup, the lower mesh partition starts at a depth of 400 m, with a grid spacing of 7.5 m. Figure 5.7a compares ETFs to TTFs, based on the 3D models generated by the MRVBF technique, as well as the soil profile at TKCH05 and our simplified profile. Compared to the 1D models, the 3D models are able to fit the ETFs much better, with VR values of 0.50 and 0.86 for the 3D models with the original and simplified profiles, respectively. The 3D models, while both producing a shift of the second peak compared with their corresponding 1D models, show remarkable improvement in the amplitudes of the first peak, especially when using the simplified profile. The results suggest that the simplified velocity profile, combining the borehole logs from the two adjacent sites, characterizes the local subsurface velocity structure below TKCH05 significantly better than the TKCH05 borehole log.

In general, a site response model can be evaluated by comparing the predicted surface ground motions (obtained by convolving the TF with the records at the reference site), with those recorded at the site of interest. We follow the traditional procedure for the calculation of TFs, neglecting the phase in the convolution process and quantifying the goodness of fit by the amplitudes only. Figure 5.7b,c compares the 1.5-8 Hz band-pass filtered surface recordings to the predicted motions from TTFs, illustrating the improvement in synthetic waveforms, as compared to data obtained at TKCH05 using the 3D as compared to the 1D model.

5.7 Discussion

We have demonstrated for two borehole sites (GVDA and TKCH05) that site amplification estimation using TTFs can be significantly improved by including effects of the underlying 3D structure. However, the 3D TTFs still leave some room for improvement. A likely important cause of the remaining misfit between TTFs computed using 3D structure and the ETFs is the uncertainty in seismic velocity estimates as a function of depth. It is common practice in soil analysis to approximate the near-surface geology as a stack of layers with constant velocity. Boore and Thompson (2007) showed that the effects of approximating logging measurements with 10 m thick, constant-slowness layers are small for frequencies less than about 5 Hz. However, Day (1996) examined analytically the relation between site response in the frequency domain and elastic structure and found that the spectral average of bandwidth Δf is only constrained by the elastic structure up to a two-way travel-time depth of $1/\Delta f$. This means that the average TF (predominantly at higher frequencies) can be biased due to uncertainty in the shallow structure. Because the first layer is often thin, a bias in the thickness estimate can contribute relatively large error in the site effects.

The deeper structure, in particular, the bedrock depth, can also be important in determining the TFs. In conventional 1D models, the bedrock topography is simplified as a layer with fixed depth; whereas, our approach incorporates lateral variations by mapping surface topography. The subsurface structure in our model is, therefore, composed of multiple irregular interfaces, each of which is anchored to the borehole log right beneath the site of interest. In some cases, the exact depth of the soil-bedrock interface is unclear. For example, the weathered granite boundary below the GVDA site is reported at 64 m by Gibbs (1989) and 87 m by Steller Steller (1996). The two velocity profiles are similar, except for the bedrock depth (Fig. 5.9a). In the following discussion, the two models utilize their respective bedrock depth and velocity profiles. Figure 5.9b shows the TFs from two 3D models assembled with the Gibbs and Steller profiles (the latter shifted 1 m deeper than the reported value due to the 4 m spatial resolution of our model). The Steller model response matches the ETF at high frequencies better than that from the Gibbs model, whereas, the latter model fits better at 1.5–7 Hz, with a slightly better overall fit (VR = 0.85 vs. 0.82). It is noticeable that the Steller model, representing lower average velocity in the soil column, results in a shift of the peaks of the TF to the left at low frequencies. We conclude that both the lateral variation and the location of the subsurface strata are important in modeling the site response. The 3D-to-1D comparison shown in Figure 5.4 indicates that the lateral variations lead to changes in both the amplitudes and the frequency of the TF, whereas the variability of the bedrock depth mainly results in shifts in frequency of the TF.

Another source of uncertainty in the site amplification estimates arises from unconstrained (mostly high frequency) scattering effects from crustal SSHs, and we test the effects thereof from a range of different parameters of the von Karman autocorrelation functions. Figure 5.10 shows the 3D TTFs modeled with a nine-realization ensemble of von Karman velocity and density perturbations, by varying the Hurst number from 0.05 to 0.15, the correlation length from 50 to 500 m, and the standard deviation of 5% and 10%, while keeping the horizontal-to-vertical anisotropy at 5. We find that the TTFs computed from these 3D models are relatively insensitive to the SSHs, except near the upper limit of our modeling bandwidth (> 9 Hz). The median VR (0.83) of the resulting TTFs is similar to that without including the SSHs, suggesting that the random fields do not contribute first-order effects to the site amplification. However, our sensitivity study included only limited realizations for each set of von Karman parameters due to computational limitations, and, we recommend a more thorough analysis, estimating the uncertainty of the site amplification estimates arising from additional ensembles of statistical distributions of small-scale crustal perturbations.

To better understand the reasons why the 3D models better predict the observed site amplification, as compared to their 1D counterparts, we show snapshots of wave propagation for our 3D and 1D (simplified) models of TKCH05 in Figures S5.3 and S5.4. The snapshots are extracted for frequencies between 4.5 and 5 Hz, in which the 3D TTF provides a much improved fit to the ETF, as compared to the 1D TTF. As expected, the 3D models naturally increase the complexity of the wave propagation compared to the SH1D model, for example, the presence of wave energy trapped in basins, and reflections at interfaces between geological units with different V_S (Fig. S5.3). For example, note the horizontally propagating energy in the upper tens of meters in the snapshots from the 3D model, naturally absent in the 1D results. Of course,

the improvement in the site response from the 3D model depends on the accuracy of the added degrees of freedom.

To further illustrate this added complexity, we compare the horizontal and vertical cumulative energy along the borehole profile (Fig. Figure 5.11a,b) to the theoretical (1D) response (Fig. Figure 5.11c) for different incidence angles at TKCH05. We carry out our analysis for the bandwidth 1.6–1.9 Hz, centered on the largest SH1D ETF peak at about 1.75 Hz (see Fig. 5.7a). The depth-dependent theoretical particle velocities, with the internal reflections neglected, can be described as follows:

$$v(z,t) = \cos\left(\omega\left(t - \frac{z\cos\theta}{V_S}\right)\right) + \cos\left(\omega\left(t + \frac{z\cos\theta}{V_S}\right)\right)$$
 (5.6)

in which z is the depth, t is the time, ω is the angular frequency, and θ is the incidence angle. As inferred from the SH1D solution in Figure 5.11c, the peak at 1.75 Hz is, primarily, due to a node at the downhole sensor location in the vertical-incidence response. This theoretical solution implies that a small departure from vertical incidence, which, in practice, is caused by interactions with the 3D bedrock interface, scatters some vertically propagating seismic waves to obliquely propagating waves, and moves the node to greater depth, thereby, increasing the response at the sensor depth point. Such wave scattering changes the energy distribution along depth, including the reduced horizontal-component energy near a depth of 100 m in the 3D model compared to the 1D model (Fig. 5.11a) and the increase in vertical-component energy (Fig. 5.11b). The results indicate that at TKCH05, the site response remains a first-order 1D resonance effect, but coupled with 3D effects from horizontally propagating waves, which, when included, greatly improves the fit to the ETF compared with the SH1D model.

5.8 Summary and Conclusions

We present a method to obtain refined site effect measurements by taking into account 3D structural variation below a downhole array site and a path to refine estimates of the elastic properties of the underlying stratigraphy via the MRVBF technique. The approach requires layer properties (e.g., S-wave velocities) along a vertical profile (typically obtained from the downhole array) as well as regional elevation data, which is widely available for most areas.

Application of the method to two sites, GVDA in southern California and TKCH05 in Japan, illustrates the extent of improvement over the conventional 1D site effect amplifications that can be expected. The relatively poor fit of the SH1D model at TKCH05 indicates that it deviates strongly from 1D behavior, supported by the complex 3D structure in the vicinity of the downhole array obtained by the MRVBF technique. Although significant improvement of the fit was obtained at GVDA as well, our results suggest that the medium below the borehole site is more horizontally stratified than is the case at TKCH05 (smaller improvements from including the effects of a MRVBFestimated 3D model). This interpretation is also supported by the horizontally stratified nature of the resulting 3D model around the GVDA site, except for smaller patches of near-surface low-velocity material produced by the method.

Thus, our method is likely to improve the prediction of site response in the presence of significant 3D structure, as well as at sites with an oversimplified or otherwise less accurate V_S profile. However, the accuracy of the site effects estimated by our proposed technique depends strongly on the fidelity of the available soil properties in the borehole, in particular at the upper end of our target bandwidth, near 10 Hz. The variability of the bedrock depth, beneath the site, as one of the controlling parameters in constructing our 3D model, can be a significant source of error in the prediction of the TF, by introducing frequency shifts at low frequencies. Finally, our results show that the improvement of the TTFs produced by incorporating small-scale crustal heterogeneities via a statistical model is secondary to that obtained by including 3D subsurface

information.

Our results generally support the conclusions by Thompson *et al.* (2009) that the theoretical formulation to map soil properties to site amplification largely limits our ability to accurately model site response transfer functions, rather than the uncertainties of the soil property. However, our method provides a realistic constitutive framework, suitable for predicting site response, regardless of the spatial variability in material properties across the site. Furthermore, this approach can be extended to explore nonlinear soil effects, another important component of site effects not explored here. For future work, we also recommend that the assumption of the quantitative relationship between topography and bedrock depth receive further scrutiny with 3D simulations at more sites, especially where the interevent variability is large.

Data and Resources

The seismograms and borehole log data used in this study were collected from the National Research Institute for Earth Science and Disaster Prevention (National Research Institute for Earth Science and Disaster Resilience, 2019) in Japan for TKCH05, and the Earthquake Engineering Group, Earth Research Institute at University of California, Santa Barbara (UCSB) (http://nees.ucsb.edu/) for Garner Valley Downhole Array (GVDA). The transfer functions for all earthquakes and simulations at both sites used in the analysis can be obtained from the authors upon request. Some plots were made using the Generic Mapping Tools (GMT) version 6.0.0 (https:// www.generic-mapping-tools.org/; Wessel *et al.* 2019). We used the open-source project ObsPy version 1.2.0 (https://github.com/obspy/obspy) to compute the Konno–Ohmachi smoothing window for Transfer functions (TFs). All websites were last accessed in June 2020. We included figures on the event locations and recorded accelerations, as well as snapshots of the 3D and 1D simulations, for GVDA and TKCH05 in the supplemental material to this article.

Acknowledgements

Computations in this project were performed on Rhea and Summit, which are part of the Oak Ridge Leadership Facility at the Oak Ridge National Laboratory. This research was supported by the Southern California Earthquake Center (SCEC; Contribution Number 10885) and by the National Science Foundation under Grant Number EAR-1664203. SCEC is funded by National Science Foundation (NSF) Cooperative Agreement EAR-1600087 and U.S. Geological Survey (USGS) Cooperative Agreement G17AC00047. Figure 5.6a is reprinted from Thompson *et al.* (2012). The authors thank two anonymous reviewers and the Associate Editor Jim Kaklamanos for valuable suggestions that helped to improve this article.

Chapter 5, in full, is a reformatted version of the material as it appears in Bulletin of the Seismological Society of America: Hu, Z., Roten, D., Olsen, K. B, and Day, S.M. (2020). Modeling of Empirical Transfer Functions with 3D Velocity Structure. *Bulletin of the Seismological Society of America*. The dissertation author was the primary investigator and author of this paper.

Tables and Figures

Table 5.1: Earthquakes Used to Compute the Empirical Transfer Functions at Garner Valley Downhole Array (GVDA)

ID	Date (yy/mm/dd)	Time (hh:mm:ss)	M_L	Latitude (°)	Longitude (°)	Depth (km)	Distance (km)	Azimuth (°)
1	7/6/02	05:11:26	4.3	33.872	-116.212	5	48	242
2	7/6/13	14:50:34	3.4	33.697	-116.042	12	59	267
3	8/7/29	18:42:16	5.4	33.953	-117.761	15	106	108
4	8/12/06	04:18:43	5.1	34.813	-116.419	7	130	190
5	9/3/13	03:42:22	3	34.016	-117.197	15	62	129
6	9/11/15	07:54:23	3.3	33.914	-117.059	14	45	127
7	10/3/13	16:32:32	4.2	32.991	-116.358	6	81	339
8	10/6/15	04:26:58	5.7	32.7	-115.921	5	129	327
9	10/7/08	01:07:11	3	33.445	-116.406	12	35	315
10	10/11/17	09:46:15	3.2	33.987	-117.159	15	57	128
11	11/6/14	08:25:41	3.6	33.69	-116.74	18	7	111
12	11/11/19	20:32:21	3.9	33.245	-116.265	10	61	321
13	12/3/30	06:09:27	3.3	33.304	-116.879	15	45	25
14	12/5/18	10:37:12	3.6	33.319	-116.402	8	46	327
15	12/8/08	16:33:22	4.5	33.904	-117.791	10	107	105
16	12/8/27	04:41:37	4.9	33.021	-115.519	4	129	304
17	12/10/02	08:28:15	4.1	32.805	-116.144	10	108	333
18	13/03/11	16:56:06	4.7	33.502	-116.457	13	27	313
19	13/03/27	17:50:29	3.4	33.495	-116.445	8	29	312
20	14/01/16	07:40:06	3.6	33.829	-117.687	10	95	101
21	14/03/29	04:09:42	5.1	33.932	-117.917	5	119	105
22	14/05/19	20:08:52	3.8	34.253	-116.825	8	66	168
23	14/07/10	20:41:44	3.2	33.505	-116.507	15	24	320
24	14/11/03	08:53:35	3.3	34.017	-117.232	18	65	127
25	14/12/04	16:53:21	3.6	33.963	-116.635	16	33	186
26	15/05/31	13:02:56	3.6	33.313	-116.282	13	54	317
27	16/01/09	11:43:11	3.3	33.66	-116.774	14	9	84
28	16/02/14	09:01:10	3.4	33.892	-117.118	14	48	121
29	16/06/10	08:04:39	5.2	33.431	-116.443	12	34	321
30	16/09/26	14:31:08	4.3	33.298	-115.714	2	98	295
31	17/06/25	13:53:25	3.5	34.001	-116.903	14	43	150
32	17/12/09	20:45:24	3.5	33.4987	-116.801	5	22	32
33	18/04/23	00:46:09	3.9	33.921	-116.322	8	43	229
34	18/05/19	19:26:51	3.5	33.4958	-116.808	3	23	33
35	18/08/04	13:48:49	3.1	33.9323	-116.828	6	33	154
36	18/09/01	16:50:29	3.1	33.4878	-116.807	2	24	31

Table 5.2: Earthquakes Used to Compute the Empirical Transfer Functions at TKCH05

1 8/8/29 23:41:00 4.1 42.935 144.035 96 40 2 8/11/09 09:11:00 3.8 42.712 143.698 93 46 3 9/1/11 14:57:00 4.7 42.593 143.415 68 61 4 9/2/28 09:36:00 5.3 42.583 142.188 113 131 5 9/3/20 15:52:00 5 42.6 144.535 64 95 6 9/6/05 12:30:00 6.4 41.812 143.62 31 145 7 10/1/15 03:46:00 5 42.352 143.117 51 95 8 10/4/09 03:41:00 4.8 42.917 144.722 57 93 9 10/7/08 21:23:00 4.7 42.573 144.528 59 96 10 10/7/28 08:06:00 4.5 42.337 143.798 56 88 11 10/10/14	Azimuth (°)
3 9/1/11 14:57:00 4.7 42.593 143.415 68 61 4 9/2/28 09:36:00 5.3 42.583 142.188 113 131 5 9/3/20 15:52:00 5 42.6 144.535 64 95 6 9/6/05 12:30:00 6.4 41.812 143.62 31 145 7 10/1/15 03:46:00 5 42.352 143.117 51 95 8 10/4/09 03:41:00 4.8 42.917 144.722 57 93 9 10/7/08 21:23:00 4.7 42.573 144.528 59 96 10 10/7/28 08:06:00 4.5 42.337 143.798 56 88 11 10/10/14 22:59:00 5.5 42.312 143.068 53 101 12 12/3/11 17:33:00 4.4 42.537 143.265 63 71 13 12/3/14	301
3 9/1/11 14:57:00 4.7 42.593 143.415 68 61 4 9/2/28 09:36:00 5.3 42.583 142.188 113 131 5 9/3/20 15:52:00 5 42.6 144.535 64 95 6 9/6/05 12:30:00 6.4 41.812 143.62 31 145 7 10/1/15 03:46:00 5 42.352 143.117 51 95 8 10/4/09 03:41:00 4.8 42.917 144.722 57 93 9 10/7/08 21:23:00 4.7 42.573 144.528 59 96 10 10/7/28 08:06:00 4.5 42.337 143.798 56 88 11 10/10/14 22:59:00 5.5 42.312 143.068 53 101 12 12/3/11 17:33:00 4.4 42.537 143.265 63 71 13 12/3/14	352
5 9/3/20 15:52:00 5 42.6 144.535 64 95 6 9/6/05 12:30:00 6.4 41.812 143.62 31 145 7 10/1/15 03:46:00 5 42.352 143.117 51 95 8 10/4/09 03:41:00 4.8 42.917 144.722 57 93 9 10/7/08 21:23:00 4.7 42.573 144.528 59 96 10 10/7/28 08:06:00 4.5 42.337 143.068 53 101 12 12/3/11 17:33:00 4.4 42.537 143.068 53 101 12 12/3/14 19:49:00 6 40.68 144.967 69 293 14 12/7/22 13:42:00 5.1 42.488 143.052 53 98 16 12/10/26 19:52:00 3.7 42.702 143.212 104 57 17 12/11/19	16
6 9/6/05 12:30:00 6.4 41.812 143.62 31 145 7 10/1/15 03:46:00 5 42.352 143.117 51 95 8 10/4/09 03:41:00 4.8 42.917 144.722 57 93 9 10/7/08 21:23:00 4.7 42.573 144.528 59 96 10 10/7/28 08:06:00 4.5 42.337 143.798 56 88 11 10/10/14 22:59:00 5.5 42.312 143.068 53 101 12 12/3/11 17:33:00 4.4 42.537 143.265 63 71 13 12/3/14 19:49:00 6 40.68 144.967 69 293 14 12/7/22 13:42:00 5.1 42.488 143.025 61 85 15 12/8/22 10:33:00 5.2 42.347 143.052 53 98 16 12/10/26 </td <td>63</td>	63
7 10/1/15 03:46:00 5 42.352 143.117 51 95 8 10/4/09 03:41:00 4.8 42.917 144.722 57 93 9 10/7/08 21:23:00 4.7 42.573 144.528 59 96 10 10/7/28 08:06:00 4.5 42.337 143.798 56 88 11 10/10/14 22:59:00 5.5 42.312 143.068 53 101 12 12/3/11 17:33:00 4.4 42.537 143.265 63 71 13 12/3/14 19:49:00 6 40.68 144.967 69 293 14 12/7/22 13:42:00 5.1 42.488 143.025 61 85 15 12/8/22 10:33:00 5.2 42.347 143.052 53 98 16 12/10/26 19:52:00 3.7 42.702 143.212 104 57 17 12/11/	307
8 10/4/09 03:41:00 4.8 42.917 144.722 57 93 9 10/7/08 21:23:00 4.7 42.573 144.528 59 96 10 10/7/28 08:06:00 4.5 42.337 143.798 56 88 11 10/10/14 22:59:00 5.5 42.312 143.068 53 101 12 12/3/11 17:33:00 4.4 42.537 143.265 63 71 13 12/3/14 19:49:00 6 40.68 144.967 69 293 14 12/7/22 13:42:00 5.1 42.488 143.025 61 85 15 12/8/22 10:33:00 5.2 42.347 143.052 53 98 16 12/10/26 19:52:00 3.7 42.702 143.212 104 57 17 12/11/19 10:37:00 4.1 42.773 143.942 103 47 18 13/03/09 21:16:00 5 43.13 144.77 101 94	360
9 10/7/08 21:23:00 4.7 42.573 144.528 59 96 10 10/7/28 08:06:00 4.5 42.337 143.798 56 88 11 10/10/14 22:59:00 5.5 42.312 143.068 53 101 12 12/3/11 17:33:00 4.4 42.537 143.265 63 71 13 12/3/14 19:49:00 6 40.68 144.967 69 293 14 12/7/22 13:42:00 5.1 42.488 143.025 61 85 15 12/8/22 10:33:00 5.2 42.347 143.052 53 98 16 12/10/26 19:52:00 3.7 42.702 143.212 104 57 17 12/11/19 10:37:00 4.1 42.773 143.942 103 47 18 13/03/09 21:16:00 5 43.13 144.77 101 94 19 13/05/17 04:20:00 4.3 42.672 143.417 74 53	26
10 10/7/28 08:06:00 4.5 42:337 143.798 56 88 11 10/10/14 22:59:00 5.5 42:312 143.068 53 101 12 12/3/11 17:33:00 4.4 42:537 143:265 63 71 13 12/3/14 19:49:00 6 40:68 144.967 69 293 14 12/7/22 13:42:00 5.1 42.488 143.025 61 85 15 12/8/22 10:33:00 5.2 42.347 143.052 53 98 16 12/10/26 19:52:00 3.7 42.702 143.212 104 57 17 12/11/19 10:37:00 4.1 42.773 143.942 103 47 18 13/03/09 21:16:00 5 43.13 144.77 101 94 19 13/05/17 04:20:00 4.3 42.672 143.417 74 53 20	284
11 10/10/14 22:59:00 5.5 42.312 143.068 53 101 12 12/3/11 17:33:00 4.4 42.537 143.265 63 71 13 12/3/14 19:49:00 6 40.68 144.967 69 293 14 12/7/22 13:42:00 5.1 42.488 143.025 61 85 15 12/8/22 10:33:00 5.2 42.347 143.052 53 98 16 12/10/26 19:52:00 3.7 42.702 143.212 104 57 17 12/11/19 10:37:00 4.1 42.773 143.942 103 47 18 13/03/09 21:16:00 5 43.13 144.77 101 94 19 13/05/17 04:20:00 4.3 42.672 143.417 74 53 20 13/08/22 15:53:00 4.8 42.318 142.995 54 103 21 <t< td=""><td>309</td></t<>	309
12 12/3/11 17:33:00 4.4 42.537 143.265 63 71 13 12/3/14 19:49:00 6 40.68 144.967 69 293 14 12/7/22 13:42:00 5.1 42.488 143.025 61 85 15 12/8/22 10:33:00 5.2 42.347 143.052 53 98 16 12/10/26 19:52:00 3.7 42.702 143.212 104 57 17 12/11/19 10:37:00 4.1 42.773 143.942 103 47 18 13/03/09 21:16:00 5 43.13 144.77 101 94 19 13/05/17 04:20:00 4.3 42.672 143.417 74 53 20 13/08/22 15:53:00 4.8 42.318 142.995 54 103 21 13/10/21 12:33:00 4.6 42.32 143.047 50 101 22 14/04/21 16:46:00 4.2 42.492 143.563 77 70 <	350
13 12/3/14 19:49:00 6 40.68 144.967 69 293 14 12/7/22 13:42:00 5.1 42.488 143.025 61 85 15 12/8/22 10:33:00 5.2 42.347 143.052 53 98 16 12/10/26 19:52:00 3.7 42.702 143.212 104 57 17 12/11/19 10:37:00 4.1 42.773 143.942 103 47 18 13/03/09 21:16:00 5 43.13 144.77 101 94 19 13/05/17 04:20:00 4.3 42.672 143.417 74 53 20 13/08/22 15:53:00 4.8 42.318 142.995 54 103 21 13/10/21 12:33:00 4.6 42.32 143.047 50 101 22 14/04/21 16:46:00 4.2 42.492 143.563 77 70 23 <t< td=""><td>27</td></t<>	27
14 12/7/22 13:42:00 5.1 42.488 143.025 61 85 15 12/8/22 10:33:00 5.2 42.347 143.052 53 98 16 12/10/26 19:52:00 3.7 42.702 143.212 104 57 17 12/11/19 10:37:00 4.1 42.773 143.942 103 47 18 13/03/09 21:16:00 5 43.13 144.77 101 94 19 13/05/17 04:20:00 4.3 42.672 143.417 74 53 20 13/08/22 15:53:00 4.8 42.318 142.995 54 103 21 13/10/21 12:33:00 4.6 42.32 143.047 50 101 22 14/04/21 16:46:00 4.2 42.492 143.563 77 70 23 15/03/25 09:34:00 5 42.352 143.095 50 96 24 15/08/14 13:43:00 5.1 42.752 143.112 80 58	24
15 12/8/22 10:33:00 5.2 42.347 143.052 53 98 16 12/10/26 19:52:00 3.7 42.702 143.212 104 57 17 12/11/19 10:37:00 4.1 42.773 143.942 103 47 18 13/03/09 21:16:00 5 43.13 144.77 101 94 19 13/05/17 04:20:00 4.3 42.672 143.417 74 53 20 13/08/22 15:53:00 4.8 42.318 142.995 54 103 21 13/10/21 12:33:00 4.6 42.32 143.047 50 101 22 14/04/21 16:46:00 4.2 42.492 143.563 77 70 23 15/03/25 09:34:00 5 42.352 143.095 50 96 24 15/08/14 13:43:00 5.1 42.752 143.112 80 58 25 15/09/26 18:49:00 4.5 42.212 141.957 94 170 26 15/11/11 00:50:00 3.9 42.955 143.758 116 22 27 16/07/24 11:51:00 <td>337</td>	337
16 12/10/26 19:52:00 3.7 42.702 143.212 104 57 17 12/11/19 10:37:00 4.1 42.773 143.942 103 47 18 13/03/09 21:16:00 5 43.13 144.77 101 94 19 13/05/17 04:20:00 4.3 42.672 143.417 74 53 20 13/08/22 15:53:00 4.8 42.318 142.995 54 103 21 13/10/21 12:33:00 4.6 42.32 143.047 50 101 22 14/04/21 16:46:00 4.2 42.492 143.563 77 70 23 15/03/25 09:34:00 5 42.352 143.095 50 96 24 15/08/14 13:43:00 5.1 42.752 143.112 80 58 25 15/09/26 18:49:00 4.5 42.212 141.957 94 170 26 15/11/11 00:50:00 3.9 42.955 143.758 116 22	35
17 12/11/19 10:37:00 4.1 42.773 143.942 103 47 18 13/03/09 21:16:00 5 43.13 144.77 101 94 19 13/05/17 04:20:00 4.3 42.672 143.417 74 53 20 13/08/22 15:53:00 4.8 42.318 142.995 54 103 21 13/10/21 12:33:00 4.6 42.32 143.047 50 101 22 14/04/21 16:46:00 4.2 42.492 143.563 77 70 23 15/03/25 09:34:00 5 42.352 143.095 50 96 24 15/08/14 13:43:00 5.1 42.752 143.112 80 58 25 15/09/26 18:49:00 4.5 42.212 141.957 94 170 26 15/11/11 00:50:00 3.9 42.955 143.758 116 22 27 16/07/24 11:51:00 4.9 42.873 143.173 96 46 28 16/09/07 18:42:00 4.7 42.493 142.68 110 104	29
18 13/03/09 21:16:00 5 43.13 144.77 101 94 19 13/05/17 04:20:00 4.3 42.672 143.417 74 53 20 13/08/22 15:53:00 4.8 42.318 142.995 54 103 21 13/10/21 12:33:00 4.6 42.32 143.047 50 101 22 14/04/21 16:46:00 4.2 42.492 143.563 77 70 23 15/03/25 09:34:00 5 42.352 143.095 50 96 24 15/08/14 13:43:00 5.1 42.752 143.112 80 58 25 15/09/26 18:49:00 4.5 42.212 141.957 94 170 26 15/11/11 00:50:00 3.9 42.955 143.758 116 22 27 16/07/24 11:51:00 4.9 42.873 143.173 96 46 28 16/09/07 18:42:00 4.7 42.493 142.68 110 104	36
19 13/05/17 04:20:00 4.3 42.672 143.417 74 53 20 13/08/22 15:53:00 4.8 42.318 142.995 54 103 21 13/10/21 12:33:00 4.6 42.32 143.047 50 101 22 14/04/21 16:46:00 4.2 42.492 143.563 77 70 23 15/03/25 09:34:00 5 42.352 143.095 50 96 24 15/08/14 13:43:00 5.1 42.752 143.112 80 58 25 15/09/26 18:49:00 4.5 42.212 141.957 94 170 26 15/11/11 00:50:00 3.9 42.955 143.758 116 22 27 16/07/24 11:51:00 4.9 42.873 143.173 96 46 28 16/09/07 18:42:00 4.7 42.493 142.68 110 104	326
20 13/08/22 15:53:00 4.8 42.318 142.995 54 103 21 13/10/21 12:33:00 4.6 42.32 143.047 50 101 22 14/04/21 16:46:00 4.2 42.492 143.563 77 70 23 15/03/25 09:34:00 5 42.352 143.095 50 96 24 15/08/14 13:43:00 5.1 42.752 143.112 80 58 25 15/09/26 18:49:00 4.5 42.212 141.957 94 170 26 15/11/11 00:50:00 3.9 42.955 143.758 116 22 27 16/07/24 11:51:00 4.9 42.873 143.173 96 46 28 16/09/07 18:42:00 4.7 42.493 142.68 110 104	269
21 13/10/21 12:33:00 4.6 42.32 143.047 50 101 22 14/04/21 16:46:00 4.2 42.492 143.563 77 70 23 15/03/25 09:34:00 5 42.352 143.095 50 96 24 15/08/14 13:43:00 5.1 42.752 143.112 80 58 25 15/09/26 18:49:00 4.5 42.212 141.957 94 170 26 15/11/11 00:50:00 3.9 42.955 143.758 116 22 27 16/07/24 11:51:00 4.9 42.873 143.173 96 46 28 16/09/07 18:42:00 4.7 42.493 142.68 110 104	18
22 14/04/21 16:46:00 4.2 42.492 143.563 77 70 23 15/03/25 09:34:00 5 42.352 143.095 50 96 24 15/08/14 13:43:00 5.1 42.752 143.112 80 58 25 15/09/26 18:49:00 4.5 42.212 141.957 94 170 26 15/11/11 00:50:00 3.9 42.955 143.758 116 22 27 16/07/24 11:51:00 4.9 42.873 143.173 96 46 28 16/09/07 18:42:00 4.7 42.493 142.68 110 104	30
23 15/03/25 09:34:00 5 42.352 143.095 50 96 24 15/08/14 13:43:00 5.1 42.752 143.112 80 58 25 15/09/26 18:49:00 4.5 42.212 141.957 94 170 26 15/11/11 00:50:00 3.9 42.955 143.758 116 22 27 16/07/24 11:51:00 4.9 42.873 143.173 96 46 28 16/09/07 18:42:00 4.7 42.493 142.68 110 104	28
24 15/08/14 13:43:00 5.1 42.752 143.112 80 58 25 15/09/26 18:49:00 4.5 42.212 141.957 94 170 26 15/11/11 00:50:00 3.9 42.955 143.758 116 22 27 16/07/24 11:51:00 4.9 42.873 143.173 96 46 28 16/09/07 18:42:00 4.7 42.493 142.68 110 104	4
25 15/09/26 18:49:00 4.5 42.212 141.957 94 170 26 15/11/11 00:50:00 3.9 42.955 143.758 116 22 27 16/07/24 11:51:00 4.9 42.873 143.173 96 46 28 16/09/07 18:42:00 4.7 42.493 142.68 110 104	27
26 15/11/11 00:50:00 3.9 42.955 143.758 116 22 27 16/07/24 11:51:00 4.9 42.873 143.173 96 46 28 16/09/07 18:42:00 4.7 42.493 142.68 110 104	45
27 16/07/24 11:51:00 4.9 42.873 143.173 96 46 28 16/09/07 18:42:00 4.7 42.493 142.68 110 104	54
28 16/09/07 18:42:00 4.7 42.493 142.68 110 104	328
	53
	48
29 16/10/09 03:36:00 3.9 42.877 143.923 115 37	317
30 16/10/12 04:02:00 5 42.325 143.042 50 100	28
31 17/02/27 18:10:00 4.7 42.348 143.048 52 98	29
32 17/03/14 12:57:00 4.7 42.815 142.7 82 82	66
33 17/04/30 23:42:00 5.4 42.322 143.07 53 99	27
34 17/09/10 17:44:00 5.6 41.758 142.877 43 163	22
35 17/11/03 12:45:00 5 42.563 143.748 66 63	350
36 18/04/14 04:00:00 5.4 43.175 145.737 53 172	267

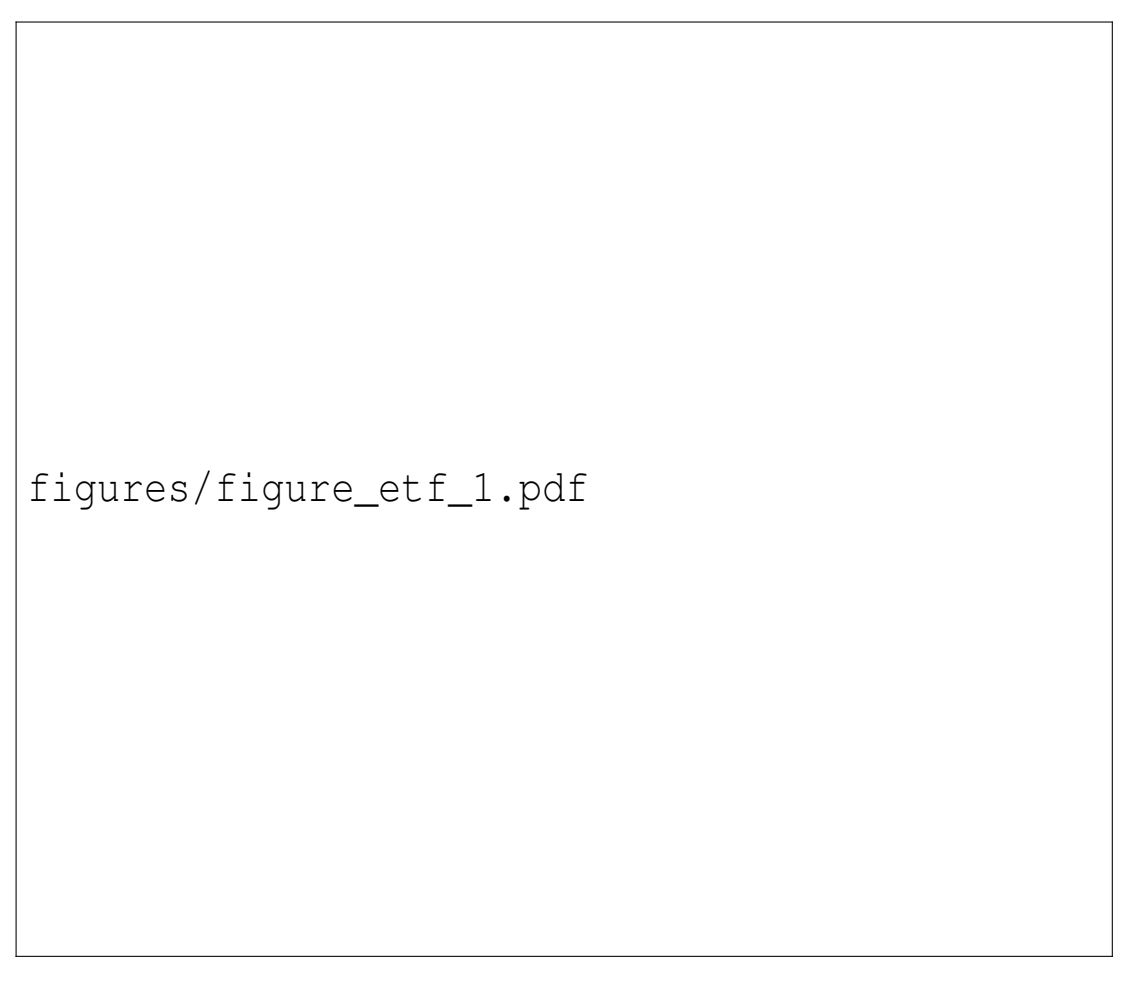


Figure 5.1: Site map of Garner Valley Downhole Array (GVDA), denoted by the star. The rectangle depicts the extent of the modeling domain, where the contours depict elevation in meters. The triangle denotes a nearby outcrop site GVAR. The color version of this figure is available only in the electronic edition.



Figure 5.2: (a) Multiresolution index of valley bottom flatness (MRVBF) and (b) the bedrock depth map surrounding GVDA, which is depicted by a triangle in both figures. (c) The mapping function from MRVBF to bedrock depth, with GVDA marked with an asterisk. The color version of this figure is available only in the electronic edition.



Figure 5.3: Cross sections of V_S in the 3D mesh (see Fig. 5.2) intersecting GVDA along (a) A–A' and (c) B–B'; the downhole accelerometer is denoted with the asterisk. (b) The 1D V_S profile, with its location denoted by the dashed line in the left panels, obtained from the borehole log, and used in the SH1D model. The color version of this figure is available only in the electronic edition.

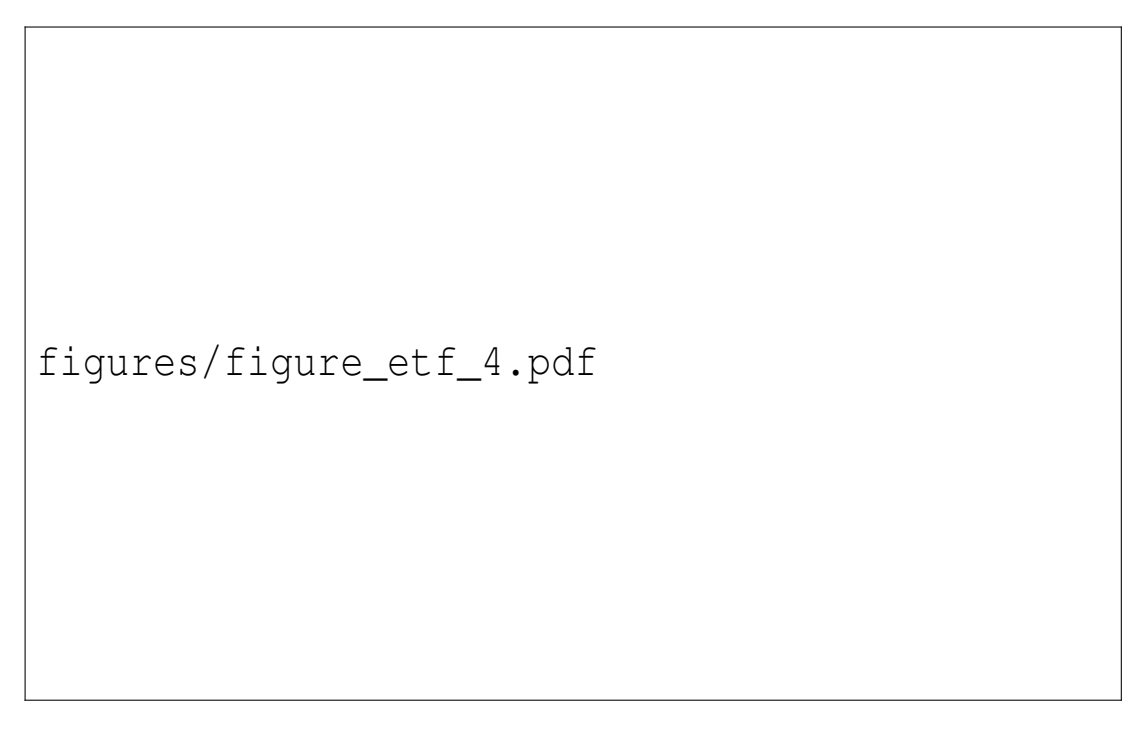


Figure 5.4: Comparison between the theoretical transfer functions (TTFs) computed using the 3D model and the SH1D model at GVDA, with the two-sigma scatter of empirical transfer functions (ETFs) shaded in gray. The color version of this figure is available only in the electronic edition.

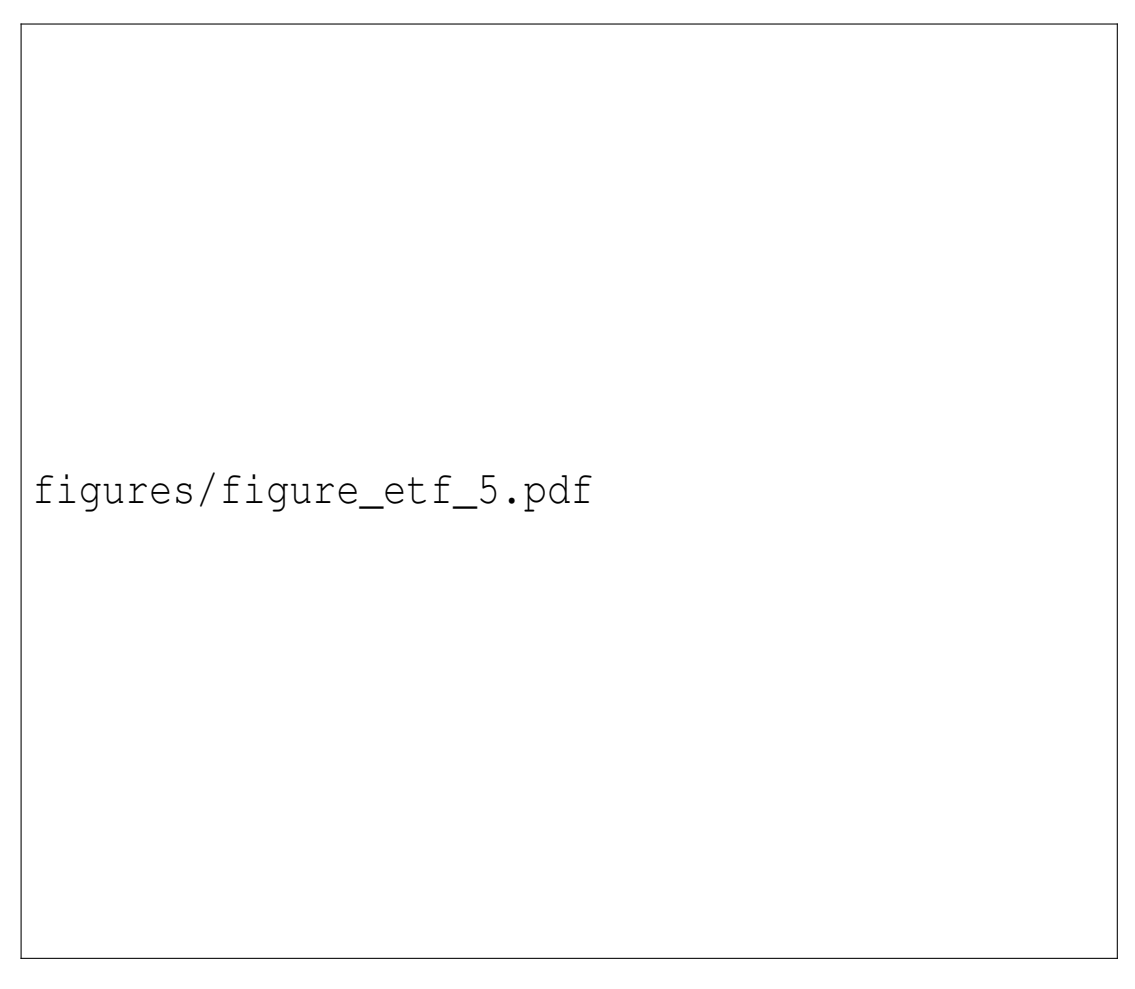


Figure 5.5: Site map of TKCH05, denoted by the star. The rectangle depicts the extent of the modeling domain, where the contours depict elevation in meters. The color version of this figure is available only in the electronic edition.



Figure 5.6: (a) Borehole log at TKCH05 (from Thompson *et al.* 2012). (b) Borehole V_S profiles at TKCH05 and HKD090, as well as for our simplified 1D model. The color version of this figure is available only in the electronic edition.



Figure 5.7: (a) Comparison between TTFs and the two-sigma scatter of the ETF for 3D and 1D models at TKCH05. Solid and dashed lines without markers are the 3D and 1D models based on the borehole log profile, respectively; solid and dashed lines with diamond markers depict the 3D and 1D models, based on the simplified downhole profile. (b,c) Comparison of 1.5–8 Hz observed east—west component surface ground motions with those obtained from convolution of the downhole records with the TTFs from models using the simplified profile for the (b) 3D model and (c) 1D model. The color version of this figure is available only in the electronic edition.

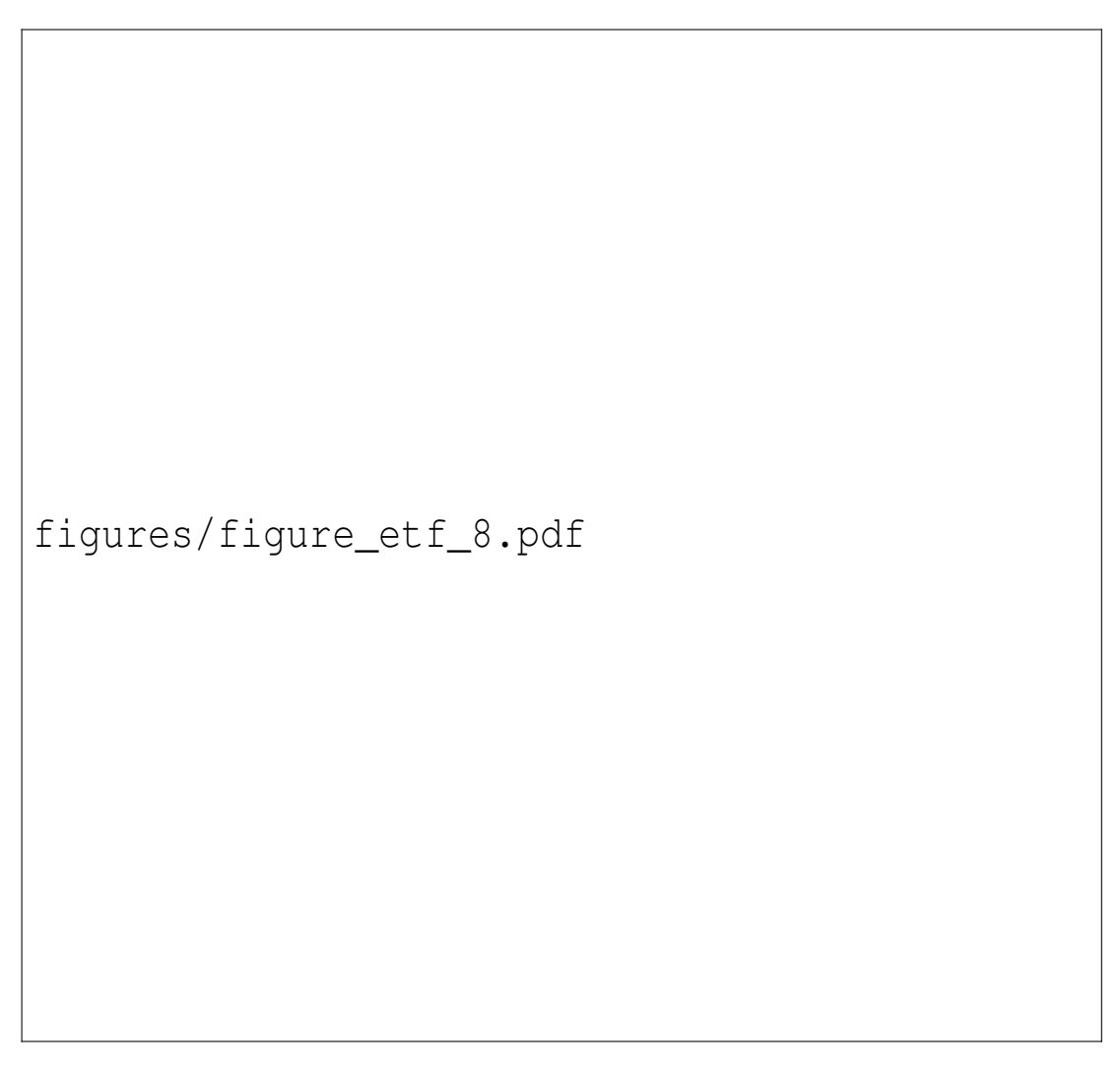


Figure 5.8: (a) MRVBF and (c) depth to bedrock in the vicinity of TKCH05, with the site location denoted by the triangle. (b) West–east A–A' and (d) north–south B–B' cross sections intersecting TKCH05, the downhole sensor is marked with the asterisk. The color version of this figure is available only in the electronic edition.

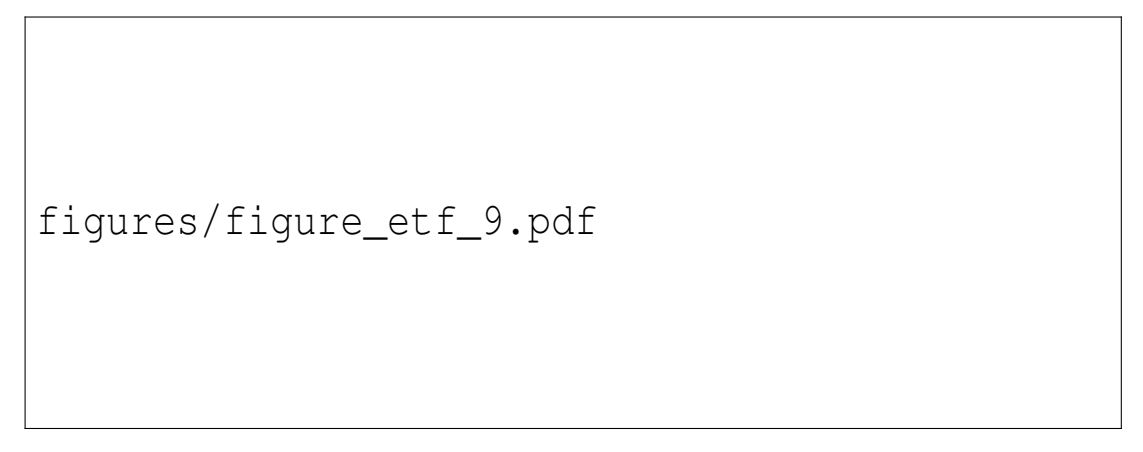


Figure 5.9: (a) The Gibbs and Steller velocity profiles at GVDA, in which the bedrock depth is 64 (solid line) and 88 m (dashed line), respectively. (b) Comparison between the two-sigma scatter of the ETFs (gray shaded) and the TTFs from the 3D models assembled with the Gibbs and Steller profiles, respectively. The color version of this figure is available only in the electronic edition.



Figure 5.10: Comparison between the median ensemble ETF, the TTF from the 3D model without and with small-scale heterogeneities (SSHs) at TKCH05. The gray shaded region is the range of maximum and minimum values encountered in TTFs from these realizations of SSHs. The color version of this figure is available only in the electronic edition.



Figure 5.11: Energy on the (a) horizontal and (b) vertical components at the site TKCH05. (c) Total energy along depth using the simplified velocity profile at TKCH05 with different incidence angles. The gray horizontal line, at around 100 m depth, depicts the downhole site depth. The color version of this figure is available only in the electronic edition.

Supplementary Materials

This supplement includes one figure (Figure S5.1) showing the location of the events used in the GVDA study and recorded accelerations at a subset of events, one figure (Figure S5.2) showing the locations of the events used in the TKCH05 study and recorded accelerations at a subset of events, and two figures (Figures S5.3 and S5.4) showing the comparison of snapshots generated in 3D and 1D models at the TKCH05 site in Japan.

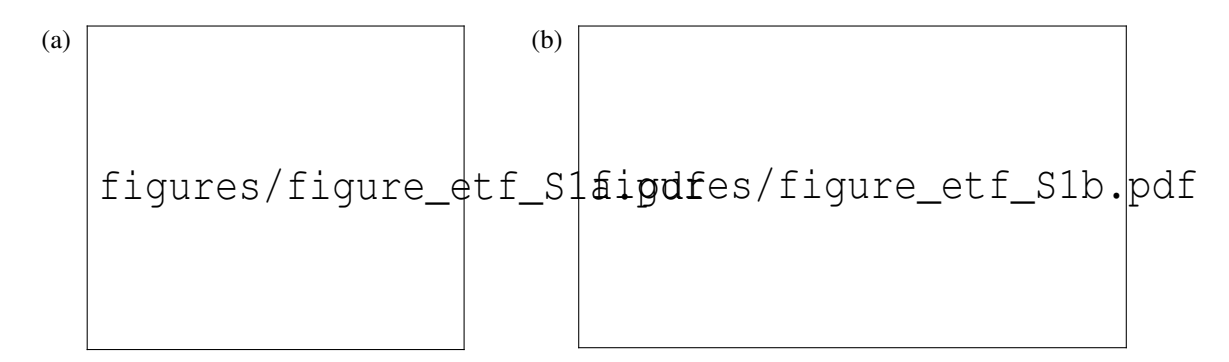


Figure S5.1: (a) Map of events (purple triangles) used for computing the ETFs at GVDA. The red triangle depicts the event used in simulations. (b) Recorded accelerations (normalized) along West-East direction at 10 randomly selected sites. The maximum amplitude is showed to the left of each line.

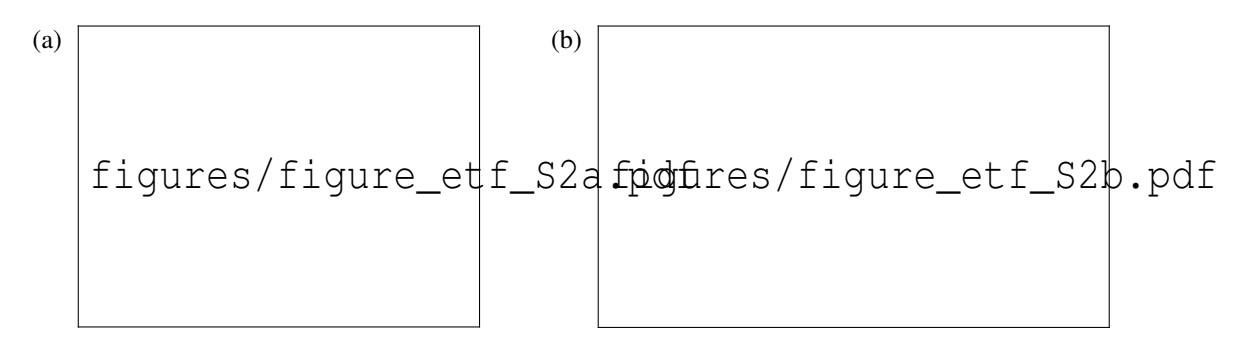


Figure S5.2: (a) Map of events (purple triangles) used for computing the ETFs at TKCH05. The red triangle depicts the event used in simulations. (b) Recorded accelerations (normalized) along West-East direction at 10 randomly selected sites. The maximum amplitude is showed to the left of each line.

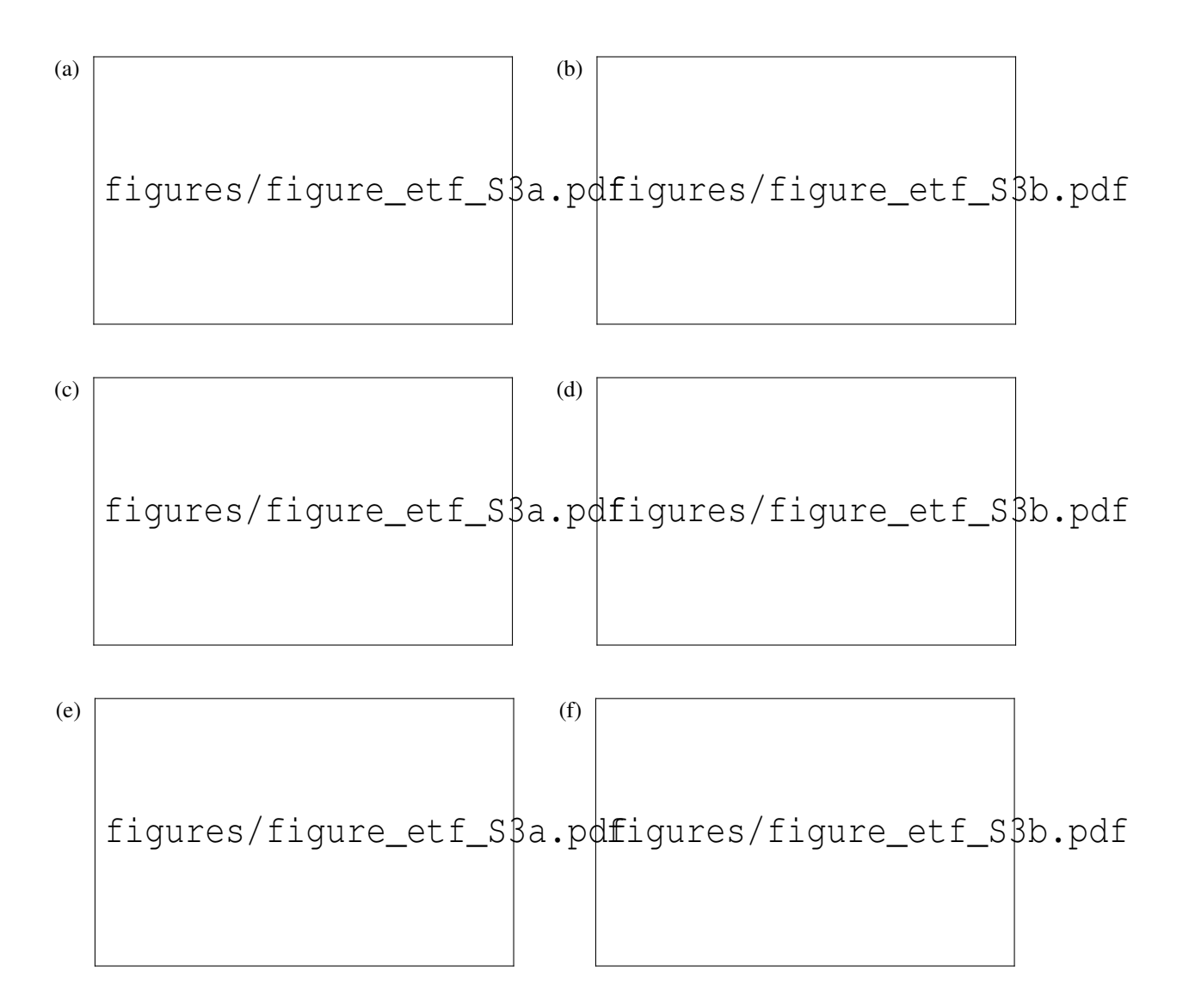


Figure S5.3: Snapshots of V_X at TKCH05 along the A-A' cross section in Figure 5.8c, bandpass filtered between 4.5 and 5 Hz. (a), (c) and (e) display snapshots of the 3D model, where the gray contour lines represent interfaces between bulks with difference Vs; the green star denotes the downhole site and the green line marks its depth. (b), (d) and (f) are for the 1D model.

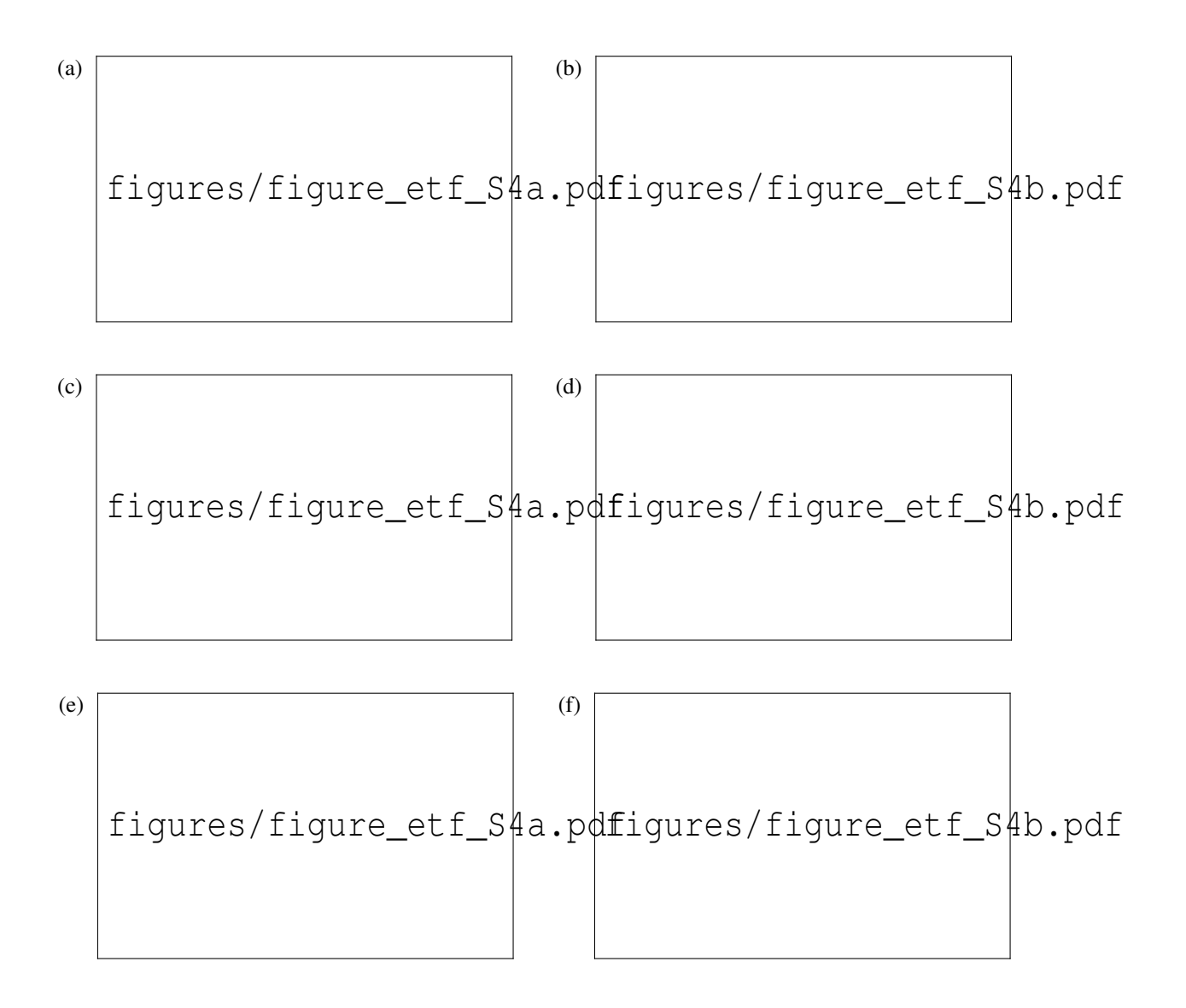


Figure S5.4: Same as Figure S5.3, except along the B-B' cross section in Figure 5.8c.

Appendix

A Von Karmen Autocorrelation Function

The form of the Von Karman autocorrelation function (Frankel and Clayton, 1986) is

$$\Phi_{\nu,a}(r) = \sigma^2 \frac{2^{1-\nu}}{\Gamma(\nu)} \left(\frac{r}{a}\right)^{\nu} K_{\nu} \left(\frac{r}{a}\right) \tag{A1}$$

in which v is the Hurst component, a is the correlation length, K_v is the modified Bessel function of order v, $\Gamma(v)$ is the gamma function, and σ^2 is the variance with Fourier transform:

$$P(k) = \frac{\sigma^2 (2\sqrt{\pi}a)^E \Gamma(\nu + E/2)^{\nu + E/2}}{\Gamma(\nu) (1 + k^2 a^2)}$$
(A2)

in which k is the wave number and E is the Euclidean dimension.

Bibliography

- Abercrombie, R. E. (1997). "Near-Surface Attenuation and Site Effects from Comparison of Surface and Deep Borehole Recordings". In: *Bulletin of the Seismological Society of America* 87.3, pp. 731–744. ISSN: 0037-1106.
- Abrahamson, N. and Silva, W. (2008). "Summary of the Abrahamson & Silva NGA Ground-Motion Relations". In: *Earthquake Spectra* 24.1, pp. 67–97. ISSN: 8755-2930, 1944-8201.
- Abrahamson, N. A., Silva, W. J., and Kamai, R. (2014). "Summary of the ASK14 Ground Motion Relation for Active Crustal Regions". In: *Earthquake Spectra* 30.3, pp. 1025–1055. ISSN: 8755-2930, 1944-8201.
- Aki, K. and Richards, P. G. (2002). *Quantitative Seismology*. 2nd ed. Sausalito, CA: University Science Books. ISBN: 0-935702-96-2.
- Aki, K. (1969). "Analysis of the Seismic Coda of Local Earthquakes as Scattered Waves". In: *Journal of Geophysical Research* (1896-1977) 74.2, pp. 615–631. ISSN: 2156-2202.
- (1980). "Attenuation of Shear-Waves in the Lithosphere for Frequencies from 0.05 to 25 Hz". In: *Physics of the Earth and Planetary Interiors* 21.1, pp. 50–60. ISSN: 00319201.
- (1993). "Local Site Effects on Weak and Strong Ground Motion". In: *Tectonophysics*. New Horizons in Strong Motion: Seismic Studies and Engineering Practice 218.1, pp. 93–111. ISSN: 0040-1951.
- Aki, K. and Chouet, B. (1975). "Origin of Coda Waves: Source, Attenuation, and Scattering Effects". In: *Journal of Geophysical Research* (1896-1977) 80.23, pp. 3322–3342. ISSN: 2156-2202.
- Akkar, S. and Bommer, J. J. (2010). "Empirical Equations for the Prediction of PGA, PGV, and Spectral Accelerations in Europe, the Mediterranean Region, and the Middle East". In: *Seismological Research Letters* 81.2, pp. 195–206. ISSN: 0895-0695.
- Andrews, D. J., Hanks, T. C., and Whitney, J. W. (2007). "Physical Limits on Ground Motion at Yucca Mountain". In: *Bulletin of the Seismological Society of America* 97.6, pp. 1771–1792. ISSN: 0037-1106.

- Archuleta, R., Seale, S., and Swain, L. B. S. (1992). "Garner Valley Downhole Array of Accelerometers: Instrumentation and Preliminary Data Analysis". In: *Bulletin of the Seismological Society of America* 82.4, pp. 1592–1621.
- Ashford, S. A. and Sitar, N. (1997). "Analysis of Topographic Amplification of Inclined Shear Waves in a Steep Coastal Bluff". In: *Bulletin of the Seismological Society of America* 87.3, pp. 692–700. ISSN: 0037-1106.
- Aster, R. C. and Shearer, P. M. (1991). "High-Frequency Borehole Seismograms Recorded in the San Jacinto Fault Zone, Southern California. Part 1. Polarizations". In: *Bulletin of the Seismological Society of America* 81.4, pp. 1057–1080. ISSN: 0037-1106.
- Atik, L. A., Abrahamson, N., Bommer, J. J., Scherbaum, F., Cotton, F., and Kuehn, N. (2010). "The Variability of Ground-Motion Prediction Models and Its Components". In: *Seismological Research Letters* 81.5, pp. 794–801. ISSN: 0895-0695.
- Atkinson, G. M. and Boore, D. M. (2006). "Earthquake Ground-Motion Prediction Equations for Eastern North America". In: *Bulletin of the Seismological Society of America* 96.6, pp. 2181–2205. ISSN: 0037-1106.
- Atkinson, G. M. (1995). "Attenuation and Source Parameters of Earthquakes in the Cascadia Region". In: *Bulletin of the Seismological Society of America* 85.5, pp. 1327–1342. ISSN: 0037-1106.
- Bao, H., Bielak, J., Ghattas, O., Kallivokas, L. F., O'Hallaron, D. R., Shewchuk, J. R., and Xu, J. (1998). "Large-Scale Simulation of Elastic Wave Propagation in Heterogeneous Media on Parallel Computers". In: *Computer Methods in Applied Mechanics and Engineering*. Containing Papers Presented at the Symposium on Advances in Computational Mechanics 152.1, pp. 85–102. ISSN: 0045-7825.
- Barani, S., De Ferrari, R., and Ferretti, G. (2013). "Influence of Soil Modeling Uncertainties on Site Response". In: *Earthquake Spectra* 29.3, pp. 705–732. ISSN: 8755-2930, 1944-8201.
- Bean, C. J., Marsan, D., and Martini, F. (1999). "Statistical Measures of Crustal Heterogeneity from Reflection Seismic Data: The Role of Seismic Bandwidth". In: *Geophysical Research Letters* 26.21, pp. 3241–3244. ISSN: 1944-8007.
- Beresnev, I. A. and Wen, K.-L. (1996). "Nonlinear Soil Response a Reality?" In: *Bulletin of the Seismological Society of America* 86.6, pp. 1964–1978.
- Bielak, J., Graves, R. W., Olsen, K. B., Taborda, R., RamÃrez-Guzmán, L., Day, S. M., Ely, G. P., Roten, D., Jordan, T. H., Maechling, P. J., Urbanic, J., Cui, Y., and Juve, G. (2010). "The ShakeOut Earthquake Scenario: Verification of Three Simulation Sets". In: *Geophysical Journal International* 180.1, pp. 375–404. ISSN: 0956540X, 1365246X.

- Blanch, J. O., Robertsson, J. O., and Symes, W. W. (1995). "Modeling of a Constant Q: Methodology and Algorithm for an Efficient and Optimally Inexpensive Viscoelastic Technique". In: *Geophysics* 60.1, pp. 176–184.
- Bommer, J. J. and Abrahamson, N. A. (2006). "Why Do Modern Probabilistic Seismic-Hazard Analyses Often Lead to Increased Hazard Estimates?" In: *Bulletin of the Seismological Society of America* 96.6, pp. 1967–1977. ISSN: 0037-1106.
- Bonilla, L. F., Steidl, J., Gariel, J.-C., and Archuleta, R. (2002). "Borehole Response Studies at the Garner Valley Downhole Array, Southern California". In: *Bulletin of the Seismological Society of America* 92.8, pp. 3165–3179. ISSN: 0037-1106.
- Boore, D. M. (1972). "A Note on the Effect of Simple Topography on Seismic SH Waves". In: *Bulletin of the Seismological Society of America* 62.1, pp. 275–284.
- Boore, D. M. and Joyner, W. B. (1997). "Site Amplifications for Generic Rock Sites". In: p. 15.
- Boore, D. M. (1986). "Short-Period P- and S-Wave Radiation from Large Earthquakes: Implications for Spectral Scaling Relations". In: *Bulletin of the Seismological Society of America* 76.1, pp. 43–64. ISSN: 0037-1106.
- (2004). "Can Site Response Be Predicted?" In: *Journal of Earthquake Engineering* 8 (sup001), pp. 1–41. ISSN: 1363-2469, 1559-808X.
- Boore, D. M., Stewart, J. P., Seyhan, E., and Atkinson, G. M. (2014). "NGA-West2 Equations for Predicting PGA, PGV, and 5% Damped PSA for Shallow Crustal Earthquakes". In: *Earthquake Spectra* 30.3, pp. 1057–1085. ISSN: 8755-2930.
- Boore, D. M. and Thompson, E. M. (2007). "On Using Surface-Source Downhole-Receiver Logging to Determine Seismic Slownesses". In: *Soil Dynamics and Earthquake Engineering* 27.11, pp. 971–985. ISSN: 02677261.
- Borcherdt, R. D. (1970). "Effects of Local Geology on Ground Motion near San Francisco Bay". In: *Bulletin of the Seismological Society of America* 60, pp. 29–61.
- Borcherdt, R. D. (1994). "Estimates of Site-Dependent Response Spectra for Design (Methodology and Justification)". In: *Earthquake Spectra* 10.4, pp. 617–653. ISSN: 8755-2930, 1944-8201.
- Bouckovalas, G. D. and Papadimitriou, A. G. (2005). "Numerical Evaluation of Slope Topography Effects on Seismic Ground Motion". In: *Soil Dynamics and Earthquake Engineering*. 11th International Conference on Soil Dynamics and Earthquake Engineering (ICSDEE): Part 1 25.7, pp. 547–558. ISSN: 0267-7261.
- Bozorgnia, Y., Abrahamson, N. A., Atik, L. A., Ancheta, T. D., Atkinson, G. M., Baker, J. W., Baltay, A., Boore, D. M., Campbell, K. W., Chiou, B. S.-J., Darragh, R., Day, S., Don-

- ahue, J., Graves, R. W., Gregor, N., Hanks, T., Idriss, I. M., Kamai, R., Kishida, T., Kottke, A., Mahin, S. A., Rezaeian, S., Rowshandel, B., Seyhan, E., Shahi, S., Shantz, T., Silva, W., Spudich, P., Stewart, J. P., Watson-Lamprey, J., Wooddell, K., and Youngs, R. (2014). "NGA-West2 Research Project". In: *Earthquake Spectra* 30.3, pp. 973–987. ISSN: 8755-2930, 1944-8201.
- BSSC (2003). The 2003 NEHRP Recommended Provisions for New Buildings and Other Structures. Part 1: Provisions (FEMA 450).
- Burjánek, J., Edwards, B., and Fäh, D. (2014). "Empirical Evidence of Local Seismic Effects at Sites with Pronounced Topography: A Systematic Approach". In: *Geophysical Journal International* 197.1, pp. 608–619. ISSN: 0956-540X.
- Campbell, K. W. and Bozorgnia, Y. (2014). "NGA-West2 Ground Motion Model for the Average Horizontal Components of PGA, PGV, and 5% Damped Linear Acceleration Response Spectra". In: *Earthquake Spectra* 30.3, pp. 1087–1115. ISSN: 8755-2930, 1944-8201.
- Çelebi, M. (1987). "Topographical and Geological Amplifications Determined from Strong-Motion and Aftershock Records of the 3 March 1985 Chile Earthquake". In: *Bulletin of the Seismological Society of America* 77.4, pp. 1147–1167. ISSN: 0037-1106.
- Chaljub, E., Komatitsch, D., Vilotte, J., Capdeville, Y., and Festa, G. (2006). Spectral Element Analysis in Seismology. Advances in Wave Propagation in Heterogeneous Earth, Ru-Shan Wu and Valerie Maupin, Etds., in the Series Advances.
- Chávez-García, F. J. and Faccioli, E. (2000). "Complex Site Effects and Building Codes: Making the Leap". In: *Journal of Seismology* 4.1, pp. 23–40. ISSN: 13834649.
- Chiou, B. S.-J. and Youngs, R. R. (2014). "Update of the Chiou and Youngs NGA Model for the Average Horizontal Component of Peak Ground Motion and Response Spectra". In: *Earthquake Spectra* 30.3, pp. 1117–1153. ISSN: 8755-2930, 1944-8201.
- Cui, Y., Moore, R., Olsen, K., Chourasia, A., Maechling, P., Minster, B., Day, S., Hu, Y., Zhu, J., and Jordan, T. (2009a). "Toward Petascale Earthquake Simulations". In: *Acta Geotechnica* 4.2, pp. 79–93. ISSN: 1861-1133.
- Cui, Y., Olsen, K., Chourasia, A., Moore, R., Maechling, P., and Jordan, T. (2009b). "The TeraShake Computational Platform for Large-Scale Earthquake Simulations". In: *Advances in Geocomputing*. Ed. by H. Xing. Lecture Notes in Earth Sciences. Berlin, Heidelberg: Springer, pp. 229–277. ISBN: 978-3-540-85879-9.
- Cui, Y., Olsen, K. B., Jordan, T. H., Lee, K., Zhou, J., Small, P., Roten, D., Ely, G., Panda, D. K., Chourasia, A., Levesque, J., Day, S. M., and Maechling, P. (2010). "Scalable Earthquake Simulation on Petascale Supercomputers". In: 2010 ACM/IEEE International Conference for High Performance Computing, Networking, Storage and Analysis. 2010 SC -

- International Conference for High Performance Computing, Networking, Storage and Analysis. New Orleans, LA, USA: IEEE, pp. 1–20. ISBN: 978-1-4244-7557-5.
- Day, S. M. (1996). "RMS Response of a One-Dimensional Half-Space to SH". In: *Bulletin of the Seismological Society of America* 86.2, pp. 363–370.
- Day, S. M. and Minster, J. B. (1984). "Numerical Simulation of Attenuated Wavefields Using a Padé Approximant Method". In: *Geophysical Journal International* 78.1, pp. 105–118.
- Dolan, S. S. and Bean, C. J. (1997). "Some Remarks on the Estimation of Fractal Scaling Parameters from Borehole Wire-Line Logs". In: *Geophysical Research Letters* 24.10, pp. 1271–1274. ISSN: 1944-8007.
- Duan, B. and Day, S. M. (2010). "Sensitivity Study of Physical Limits on Ground Motion at Yucca Mountain". In: *Bulletin of the Seismological Society of America* 100.6, pp. 2996–3019. ISSN: 0037-1106.
- Dunham, E. M., Belanger, D., Cong, L., and Kozdon, J. E. (2011). "Earthquake Ruptures with Strongly Rate-Weakening Friction and Off-Fault Plasticity, Part 1: Planar Faults". In: *Bulletin of the Seismological Society of America* 101.5, pp. 2296–2307. ISSN: 0037-1106.
- Ely, G., Small, P., Jordan, T. H., Maechling, P. J., and Wang, F. (2010). "A Vs30-Derived Near-Surface Seismic Velocity Model". In: AGU. No. S51A-1907. San Francisco, California, p. 1.
- Emmerich, H. and Korn, M. (1987). "Incorporation of Attenuation into Time-Domain Computations of Seismic Wave Fields". In: *Geophysics* 52.9, pp. 1252–1264.
- Erickson, D., McNamara, D. E., and Benz, H. M. (2004). "Frequency-Dependent Lg Q within the Continental United States". In: *Bulletin of the Seismological Society of America* 94.5, pp. 1630–1643. ISSN: 0037-1106.
- Field, E. H. (2000). "A Modified Ground-Motion Attenuation Relationship for Southern California That Accounts for Detailed Site Classification and a Basin-Depth Effect". In: *Bulletin of the Seismological Society of America* 90 (6B), S209–S221. ISSN: 0037-1106.
- Field, E. H., Kramer, S., Elgamal, A.-W., Bray, J., Matasovic, N., Johnson, P., Cramer, C., Roblee, C., Wald, D., Bonilla, L., Dimitriu, P., and Anderson, J. (1998). "Nonlinear Site Response: Where We're At (A Report from a SCEC/PEER Seminar and Workshop)". In: *Seismological Research Letters* 69.3, pp. 230–234. ISSN: 0895-0695.
- Field, E. H. and Jacob, K. H. (1995). "A Comparison and Test of Various Site-Response Estimation Techniques, Including Three That Are Not Reference-Site Dependent". In: *Bulletin of the Seismological Society of America* 85.4, pp. 1127–1143.

- Flatté, S. M. and Wu, R.-S. (1988). "Small-Scale Structure in the Lithosphere and Asthenosphere Deduced from Arrival Time and Amplitude Fluctuations at NORSAR". In: *Journal of Geophysical Research: Solid Earth* 93.B6, pp. 6601–6614. ISSN: 2156-2202.
- Frankel, A. and Clayton, R. W. (1986). "Finite Difference Simulations of Seismic Scattering: Implications for the Propagation of Short-Period Seismic Waves in the Crust and Models of Crustal Heterogeneity". In: *Journal of Geophysical Research* 91.B6, p. 6465. ISSN: 0148-0227.
- Frankel, A., McGarr, A., Bicknell, J., Mori, J., Seeber, L., and Cranswick, E. (1990). "Attenuation of High-Frequency Shear Waves in the Crust: Measurements from New York State, South Africa, and Southern California". In: *Journal of Geophysical Research: Solid Earth* 95.B11, pp. 17441–17457. ISSN: 2156-2202.
- Frankel, A. and Vidale, J. (1992). "A Three-Dimensional Simulation of Seismic Waves in the Santa Clara Valley, California, from a Loma Prieta Aftershock". In: *Bulletin of the Seismological Society of America* 82.5, pp. 2045–2074. ISSN: 0037-1106.
- Gallant, J. C. and Dowling, T. I. (2003). "A Multiresolution Index of Valley Bottom Flatness for Mapping Depositional Areas". In: *Water Resources Research* 39.12, p. 1347. ISSN: 00431397.
- Geli, L., Bard, P.-Y., and Jullien, B. (1988). "The Effect of Topography on Earthquake Ground Motion: A Review and New Results". In: *Bulletin of the Seismological Society of America* 78.1, pp. 42–63. ISSN: 0037-1106.
- Gibbs, J. (1989). Near-Surface P- and S-Wave Velocities from Borehole Measurements near Lake Hemet, California. Report 89-630.
- Gilbert, G. K., Holmes, J., Humphrey, R. L., Sewell, J., and Soule, F. (1907). *The San Francisco Earthquake and Fire of April 18, 1906, and Their Effects on Structures and Structural Materials*. USGS Numbered Series 324. Govt. Print. Off., pp. 1–13.
- Graves, R. W. and Pitarka, A. (2010). "Broadband Ground-Motion Simulation Using a Hybrid Approach". In: *Bulletin of the Seismological Society of America* 100 (5A), pp. 2095–2123. ISSN: 0037-1106.
- Graves, R. W. (1996). "Simulating Seismic Wave Propagation in 3D Elastic Media Using Staggered-Grid Finite Differences". In: *Bulletin of the Seismological Society of America* 86.4, pp. 1091–1106. ISSN: 0037-1106.
- Graves, R. W., Aagaard, B. T., Hudnut, K. W., Star, L. M., Stewart, J. P., and Jordan, T. H. (2008). "Broadband Simulations for M w 7.8 Southern San Andreas Earthquakes: Ground Motion Sensitivity to Rupture Speed". In: *Geophysical Research Letters* 35.22, p. L22302. ISSN: 0094-8276.

- Griffiths, S. C., Cox, B. R., Rathje, E. M., and Teague, D. P. (2016). "Mapping Dispersion Misfit and Uncertainty in Vs Profiles to Variability in Site Response Estimates". In: *Journal of Geotechnical and Geoenvironmental Engineering* 142.11, p. 04016062. ISSN: 1090-0241, 1943-5606.
- Gusev, A. A. and Abubakirov, I. R. (1996). "Simulated Envelopes of Non-Isotropically Scattered Body Waves as Compared to Observed Ones: Another Manifestation of Fractal Heterogeneity". In: *Geophysical Journal International* 127.1, pp. 49–60. ISSN: 0956-540X.
- Gutenberg, B. (1957). "Effects of Ground on Earthquake Motion". In: *Bulletin of the Seismological Society of America* 47.3, pp. 221–250. ISSN: 0037-1106.
- Hanks, T. C., Abrahamson, N., Board, M., Boore, D. M., Brune, J., and Cornell, C. (2005). "Observed Ground Motions, Extreme Ground Motions, and Physical Limits to Ground Motions". In: *Directions in Strong Motion Instrumentation*. Ed. by P. Gülkan and J. G. Anderson. Nato Science Series: IV: Earth and Environmental Sciences. Dordrecht: Springer Netherlands, pp. 55–59. ISBN: 978-1-4020-3812-9.
- Hartzell, S., Harmsen, S., and Frankel, A. (2010). "Effects of 3D Random Correlated Velocity Perturbations on Predicted Ground Motions". In: *Bulletin of the Seismological Society of America* 100.4, pp. 1415–1426. ISSN: 0037-1106.
- Hartzell, S., Ramírez-Guzmán, L., Meremonte, M., and Leeds, A. (2017). "Ground Motion in the Presence of Complex Topography II: Earthquake Sources and 3D Simulations". In: *Bulletin of the Seismological Society of America* 107.1, pp. 344–358. ISSN: 0037-1106, 1943-3573.
- Hedlin, M. A. H., Shearer, P. M., and Earle, P. S. (1997). "Seismic Evidence for Small-Scale Heterogeneity throughout the Earth's Mantle". In: *Nature* 387.6629 (6629), pp. 145–150. ISSN: 1476-4687.
- Helffrich, G. R. and Wood, B. J. (2001). "The Earth's Mantle". In: *Nature* 412.6846 (6846), pp. 501–507. ISSN: 1476-4687.
- Hill, R. (1981). "Geology of Garner Valley and Vicinity". In: South Coast Geol. Soc., pp. 90–99.
- Idriss, I. M. (2014). "An NGA-West2 Empirical Model for Estimating the Horizontal Spectral Values Generated by Shallow Crustal Earthquakes". In: *Earthquake Spectra* 30.3, pp. 1155–1177. ISSN: 8755-2930, 1944-8201.
- Imperatori, W. and Mai, P. M. (2013). "Broad-Band near-Field Ground Motion Simulations in 3-Dimensional Scattering Media". In: *Geophysical Journal International* 192.2, pp. 725–744. ISSN: 0956-540X.

- Imperatori, W. and Mai, P. (2015). "The Role of Topography and Lateral Velocity Heterogeneities on Near-Source Scattering and Ground-Motion Variability". In: *Geophysical Journal International* 202.3, pp. 2163–2181. ISSN: 0956-540X, 1365-246X.
- International Code Council (2014). 2015 IBC International Building Code, International Code Council.
- Käser, M. and Dumbser, M. (2006). "An Arbitrary High-Order Discontinuous Galerkin Method for Elastic Waves on Unstructured Meshes I. The Two-Dimensional Isotropic Case with External Source Terms". In: *Geophysical Journal International* 166.2, pp. 855–877. ISSN: 0956-540X.
- Kawase, H. and Aki, K. (1990). "Topography Effect at the Critical SV-Wave Incidence: Possible Explanation of Damage Pattern by the Whittier Narrows, California, Earthquake of 1 October 1987". In: *Bulletin of the Seismological Society of America* 80.1, pp. 1–22. ISSN: 0037-1106.
- Konno, K. and Ohmachi, T. (1998). "Ground-Motion Characteristics Estimated from Spectral Ratio between Horizontal and Vertical Components of Microtremor". In: *Bulletin of the Seismological Society of America* 88.1, pp. 228–241. ISSN: 0037-1106.
- Kramer, S. L. (1996). *Geotechnical Earthquake Engineering*. PrenticeHall, Englewood Cliffs, N. J.
- Lai, V. H., Graves, R. W., Yu, C., Zhan, Z., and Helmberger, D. V. (2020). "Shallow Basin Structure and Attenuation Are Key to Predicting Long Shaking Duration in Los Angeles Basin". In: *Journal of Geophysical Research: Solid Earth* 125.10. ISSN: 2169-9313, 2169-9356.
- Lee, E. J., Chen, P., and Jordan, T. H. (2014). "Testing Waveform Predictions of 3D Velocity Models against Two Recent Los Angeles Earthquakes". In: *Seismological Research Letters* 85.6, pp. 1275–1284. ISSN: 0895-0695, 1938-2057.
- Levander, A., Hobbs, R. W., Smith, S. K., England, R. W., Snyder, D. B., and Holliger, K. (1994). "The Crust as a Heterogeneous "Optical" Medium, or "Crocodiles in the Mist"". In: *Tectonophysics*. Seismic Reflection Probing of the Continents and Their Margins 232.1, pp. 281–297. ISSN: 0040-1951.
- Levander, A. R. and Holliger, K. (1992). "Small-Scale Heterogeneity and Large-Scale Velocity Structure of the Continental Crust". In: *Journal of Geophysical Research: Solid Earth* 97.B6, pp. 8797–8804. ISSN: 2156-2202.
- Liu, P., Archuleta, R. J., and Hartzell, S. H. (2006). "Prediction of Broadband Ground-Motion Time Histories: Hybrid Low/High- Frequency Method with Correlated Random Source Parameters". In: *Bulletin of the Seismological Society of America* 96.6, pp. 2118–2130. ISSN: 0037-1106.

- Lovati, S., Bakavoli, M., Massa, M., Ferretti, G., Pacor, F., Paolucci, R., Haghshenas, E., and Kamalian, M. (2011). "Estimation of Topographical Effects at Narni Ridge (Central Italy): Comparisons between Experimental Results and Numerical Modelling". In: *Bulletin of earthquake Engineering* 9.6, pp. 1987–2005.
- Ma, S. (2008). "A Physical Model for Widespread Near-Surface and Fault Zone Damage Induced by Earthquakes". In: *Geochemistry, Geophysics, Geosystems* 9.11.
- Mai, P. M., Imperatori, W., and Olsen, K. B. (2010). "Hybrid Broadband Ground-Motion Simulations: Combining Long-Period Deterministic Synthetics with High-Frequency Multiple S-to-S Backscattering". In: *Bulletin of the Seismological Society of America* 100 (5A), pp. 2124–2142. ISSN: 0037-1106.
- Marafi, N. A., Eberhard, M. O., Berman, J. W., Wirth, E. A., and Frankel, A. D. (2019). "Impacts of Simulated M9 Cascadia Subduction Zone Motions on Idealized Systems". In: *Earthquake Spectra* 35.3, pp. 1261–1287. ISSN: 8755-2930.
- Massa, M., Lovati, S., D'Alema, E., Ferretti, G., and Bakavoli, M. (2010). "An Experimental Approach for Estimating Seismic Amplification Effects at the Top of a Ridge, and the Implication for Ground-Motion Predictions: The Case of Narni, Central Italy". In: *Bulletin of the Seismological Society of America* 100.6, pp. 3020–3034. ISSN: 0037-1106.
- Matavosic, N. and Hashash, Y. (2012). *Practices and Procedures for Site-Specific Evaluations of Earthquake Ground Motions*. Washington, D.C.: Transportation Research Board. ISBN: 978-0-309-22355-3.
- Maufroy, E., Cruz-Atienza, V. M., Cotton, F., and Gaffet, S. (2015). "Frequency-Scaled Curvature as a Proxy for Topographic Site-Effect Amplification and Ground-Motion Variability". In: *Bulletin of the Seismological Society of America* 105.1, pp. 354–367. ISSN: 0037-1106, 1943-3573.
- Molnar, S., Cassidy, J. F., Olsen, K. B., Dosso, S. E., and He, J. (2014). "Earthquake Ground Motion and 3D Georgia Basin Amplification in Southwest British Columbia: Shallow Blind-Thrust Scenario Earthquakes". In: *Bulletin of the Seismological Society of America* 104.1, pp. 321–335.
- Nakajima, J., Hada, S., Hayami, E., Uchida, N., Hasegawa, A., Yoshioka, S., Matsuzawa, T., and Umino, N. (2013). "Seismic Attenuation beneath Northeastern Japan: Constraints on Mantle Dynamics and Arc Magmatism". In: *Journal of Geophysical Research: Solid Earth* 118.11, pp. 5838–5855. ISSN: 21699313.
- National Research Institute for Earth Science and Disaster Resilience (2019). *NIED K-NET*, *KiK-Net*. National Research Institute for Earth Science and Disaster Resilience.

- Nguyen, K.-V. and Gatmiri, B. (2007). "Evaluation of Seismic Ground Motion Induced by Topographic Irregularity". In: *Soil Dynamics and Earthquake Engineering* 27.2, pp. 183–188. ISSN: 0267-7261.
- Nie, S., Wang, Y., Olsen, K. B., and Day, S. M. (2017). "Fourth-order Staggered-grid Finite-difference Seismic Wavefield Estimation Using a Discontinuous Mesh Interface (Wedmi)". In: *Bulletin of the Seismological Society of America* 107.5, pp. 2183–2193. ISSN: 0037-1106, 1943-3573.
- Nielsen, L. and Thybo, H. (2006). "Identification of Crustal and Upper Mantle Heterogeneity by Modelling of Controlled-Source Seismic Data". In: *Tectonophysics*. The Heterogeneous Mantle 416.1, pp. 209–228. ISSN: 0040-1951.
- Nour, A., Slimani, A., Laouami, N., and Afra, H. (2003). "Finite Element Model for the Probabilistic Seismic Response of Heterogeneous Soil Profile". In: *Soil Dynamics and Earthquake Engineering* 23.5, pp. 331–348. ISSN: 02677261.
- O'Connell, R. J. and Budiansky, B. (1978). "Measures of Dissipation in Viscoelastic Media". In: *Geophysical Research Letters* 5.1, pp. 5–8. ISSN: 1944-8007.
- O'Reilly, O., Yeh, T.-Y., Olsen, K. B., Hu, Z., Breuer, A., Roten, D., and Goulet, C. (2021). "A High-Order Finite Difference Method on Staggered Curvilinear Grids for Seismic Wave Propagation Applications with Topography". In: *Bulletin of the Seismological Society of America*.
- Olsen, K., Day, S., Dalguer, L., Mayhew, J., Cui, Y., Zhu, J., Cruz-Atienza, V., Roten, D., Maechling, P., Jordan, T., *et al.* (2009). "ShakeOut-D: Ground Motion Estimates Using an Ensemble of Large Earthquakes on the Southern San Andreas Fault with Spontaneous Rupture Propagation". In: *Geophysical Research Letters* 36.4.
- Olsen, K. B., Stephenson, W. J., and Geisselmeyer, A. (2008). "3D Crustal Structure and Long-Period Ground Motions from a M9. 0 Megathrust Earthquake in the Pacific Northwest Region". In: *Journal of Seismology* 12.2, pp. 145–159.
- Olsen, K. B. (1994). "Simulation of Three Dimensional Wave Propagation in the Salt Lake Basin". Salt Lake City, Utah: The University of Utah.
- Olsen, K. B., Archuleta, R. J., and Matarese, J. R. (1995). "Three-Dimensional Simulation of a Magnitude 7.75 Earthquake on the San Andreas Fault". In: *Science* 270.5242, pp. 1628–1632. ISSN: 0036-8075, 1095-9203.
- Olsen, K. B. and Schuster, G. T. (1995). "Causes of Low-Frequency Ground Motion Amplification in the Salt Lake Basin: The Case of the Vertically Incident P Wave". In: *Geophysical Journal International* 122.3, pp. 1045–1061. ISSN: 0956540X, 1365246X.

- Pischiutta, M., Cultrera, G., Caserta, A., Luzi, L., and Rovelli, A. (2010). "Topographic Effects on the Hill of Nocera Umbra, Central Italy: Topographic Effects on Nocera Umbra Hill". In: *Geophysical Journal International* 182.2, pp. 977–987. ISSN: 0956540X, 1365246X.
- Pitarka, A. and Ichinose, G. (2009). "Simulating Forward and Backward Scattering in Viscoelastic 3D Media with Random Velocity Variations and Basin Structure". In: *US Geol. Surv. Tech. Rep.*
- Poggi, V., Edwards, B., and Fah, D. (2011). "Derivation of a Reference Shear-Wave Velocity Model from Empirical Site Amplification". In: *Bulletin of the Seismological Society of America* 101.1, pp. 258–274. ISSN: 0037-1106.
- Przybilla, J., Korn, M., and Wegler, U. (2006). "Radiative Transfer of Elastic Waves versus Finite Difference Simulations in Two-Dimensional Random Media". In: *Journal of Geophysical Research: Solid Earth* 111.B4. ISSN: 2156-2202.
- Przybilla, J., Wegler, U., and Korn, M. (2009). "Estimation of Crustal Scattering Parameters with Elastic Radiative Transfer Theory". In: *Geophysical Journal International* 178.2, pp. 1105–1111. ISSN: 0956540X, 1365246X.
- Rai, M., Rodriguez-Marek, A., and Chiou, B. S. (2017). "Empirical Terrain-Based Topographic Modification Factors for Use in Ground Motion Prediction". In: *Earthquake Spectra* 33.1, pp. 157–177. ISSN: 8755-2930, 1944-8201.
- Reid, H. F. (1910). The California Earthquake of April 18, 1906. 2, pp. 16–18.
- Roten, D., Fäh, D., Olsen, K. B., and Giardini, D. (2008). "A Comparison of Observed and Simulated Site Response in the Rhône Valley". In: *Geophysical Journal International* 173.3, pp. 958–978. ISSN: 0956540X, 1365246X.
- Roten, D., Olsen, K. B., Day, S. M., and Cui, Y. (2017). "Quantification of Fault-Zone Plasticity Effects with Spontaneous Rupture Simulations". In: *Pure and Applied Geophysics* 174.9, pp. 3369–3391. ISSN: 0033-4553, 1420-9136.
- Roten, D., Olsen, K. B., and Pechmann, J. C. (2012). "3D Simulations of M 7 Earthquakes on the Wasatch Fault, Utah, Part Ii: Broadband (0-10 Hz) Ground Motions and Nonlinear Soil Behavior". In: *Bulletin of the Seismological Society of America* 102.5, pp. 2008–2030. ISSN: 0037-1106.
- Roth, M. and Korn, M. (1993). "Single Scattering Theory Versus Numerical Modelling In 2-D Random Media". In: *Geophysical Journal International* 112.1, pp. 124–140. ISSN: 0956-540X.
- Saito, T., Sato, H., and Ohtake, M. (2002). "Envelope Broadening of Spherically Outgoing Waves in Three-Dimensional Random Media Having Power Law Spectra". In: *Journal of Geophysical Research: Solid Earth* 107.B5, ESE 3-1-ESE 3-15. ISSN: 2156-2202.

- Sánchez-Sesma, F. J. and Campillo, M. (1991). "Diffraction of P, SV, and Rayleigh Waves by Topographic Features: A Boundary Integral Formulation". In: *Bulletin of the Seismological Society of America* 81.6, pp. 2234–2253. ISSN: 0037-1106.
- Sánchez-Sesma, F. J., Herrera, I., and Avilés, J. (1982). "A Boundary Method for Elastic Wave Diffraction: Application to Scattering of SH Waves by Surface Irregularities". In: *Bulletin of the seismological Society of America* 72.2, pp. 473–490.
- Sato, H. (1989). "Broadening of Seismogram Envelopes in the Randomly Inhomogeneous Lithosphere Based on the Parabolic Approximation: Southeastern Honshu, Japan". In: *Journal of Geophysical Research: Solid Earth* 94.B12, pp. 17735–17747. ISSN: 2156-2202.
- Sato, H. and Fehler, M. C. (2009). Seismic Wave Propagation and Scattering in the Heterogeneous Earth. Berlin, Heidelberg: Springer Berlin Heidelberg. ISBN: 978-3-540-89622-7 978-3-540-89623-4.
- Savran, W. H. and Olsen, K. B. (2019). "Ground Motion Simulation and Validation of the 2008 Chino Hills Earthquake in Scattering Media". In: *Geophysical Journal International* 219.3, pp. 1836–1850. ISSN: 0956-540X, 1365-246X.
- (2016). "Model for Small-Scale Crustal Heterogeneity in Los Angeles Basin Based on Inversion of Sonic Log Data". In: *Geophysical Journal International* 205.2, pp. 856–863. ISSN: 0956-540X, 1365-246X.
- Sawazaki, K., Sato, H., and Nishimura, T. (2011). "Envelope Synthesis of Short-Period Seismograms in 3-D Random Media for a Point Shear Dislocation Source Based on the Forward Scattering Approximation: Application to Small Strike-Slip Earthquakes in Southwestern Japan". In: *Journal of Geophysical Research: Solid Earth* 116.B8. ISSN: 2156-2202.
- Seriani, G. (1998). "3-D Large-Scale Wave Propagation Modeling by Spectral Element Method on Cray T3E Multiprocessor". In: *Computer Methods in Applied Mechanics and Engineering*. Exterior Problems of Wave Propagation 164.1, pp. 235–247. ISSN: 0045-7825.
- Shapiro, S. A. and Kneib, G. (1993). "Seismic Attenuation By Scattering: Theory and Numerical Results". In: *Geophysical Journal International* 114.2, pp. 373–391. ISSN: 0956-540X.
- Shaw, J. H., Plesch, A., Tape, C., Suess, M. P., Jordan, T. H., Ely, G., Hauksson, E., Tromp, J., Tanimoto, T., Graves, R., Olsen, K., Nicholson, C., Maechling, P. J., Rivero, C., Lovely, P., Brankman, C. M., and Munster, J. (2015). "Unified Structural Representation of the Southern California Crust and Upper Mantle". In: *Earth and Planetary Science Letters* 415, pp. 1–15. ISSN: 0012-821X.
- Shearer, P. M. and Orcutt, J. S. (1987). "Surface and Near-Surface Effects on Seismic Waves—Theory and Borehole Seismometer Results". In: *Bulletin of the Seismological Society of America* 77.4, pp. 1168–1196.

- Silva, W. and Darragh, R. B. (1995). *Engineering Characterization of Strong Ground Motion Recorded at Rock Sites. Final Report*. EPRI-TR-102262. Electric Power Research Inst. (EPRI), Palo Alto, CA (United States); Pacific Engineering and Analysis, Inc., El Cerrito, CA (United States).
- Singh, S. K. and Ordaz, M. (1993). "On the Origin of Long Coda Observed in the Lake-Bed Strong-Motion Records of Mexico City". In: *Bulletin of the Seismological Society of America* 83.4, pp. 1298–1306.
- Small, P., Gill, D., Maechling, P. J., Taborda, R., Callaghan, S., Jordan, T. H., Olsen, K. B., Ely, G. P., and Goulet, C. (2017). "The SCEC Unified Community Velocity Model Software Framework". In: *Seismological Research Letters* 88.6, pp. 1539–1552. ISSN: 0895-0695, 1938-2057.
- Steidl, J. H. (1993). "Variation of Site Response at the UCSB Dense Array of Portable Accelerometers". In: *Earthquake Spectra* 9.2, pp. 289–302. ISSN: 8755-2930, 1944-8201.
- Steidl, J. H., Tumarkin, A. G., and Archuleta, R. J. (1996). "What Is a Reference Site?" In: *Bulletin of the Seismological Society of America* 86.6, pp. 1733–1748. ISSN: 0037-1106.
- Steller, R. (1996). New Borehole Geophysical Results at GVDA. UCSB Internal Report.
- Tao, Y. and Rathje, E. (2019). "Insights into Modeling Small-Strain Site Response Derived from Downhole Array Data". In: *Journal of Geotechnical and Geoenvironmental Engineering* 145.7, p. 04019023. ISSN: 1090-0241, 1943-5606.
- (2020). "Taxonomy for Evaluating the Site-Specific Applicability of One-Dimensional Ground Response Analysis". In: *Soil Dynamics and Earthquake Engineering* 128, p. 105865. ISSN: 02677261.
- Teague, D. P., Cox, B. R., and Rathje, E. M. (2018). "Measured Vs. Predicted Site Response at the Garner Valley Downhole Array Considering Shear Wave Velocity Uncertainty from Borehole and Surface Wave Methods". In: *Soil Dynamics and Earthquake Engineering* 113, pp. 339–355. ISSN: 02677261.
- Templeton, E. L., Bhat, H. S., Dmowska, R., and Rice, J. R. (2010). "Dynamic Rupture through a Branched Fault Configuration at Yucca Mountain, and Resulting Ground Motions". In: *Bulletin of the Seismological Society of America* 100.4, pp. 1485–1497. ISSN: 0037-1106.
- Thompson, E. M. (2018). An Updated Vs30 Map for California with Geologic and Topographic Constraints. U.S. Geological Survey.
- Thompson, E. M., Baise, L. G., Kayen, R. E., and Guzina, B. B. (2009). "Impediments to Predicting Site Response: Seismic Property Estimation and Modeling Simplifications". In: *Bulletin of the Seismological Society of America* 99.5, pp. 2927–2949. ISSN: 0037-1106.

- Thompson, E. M., Baise, L. G., Tanaka, Y., and Kayen, R. E. (2012). "A Taxonomy of Site Response Complexity". In: *Soil Dynamics and Earthquake Engineering* 41, pp. 32–43. ISSN: 02677261.
- Thybo, H., Nielsen, L., and Perchuc, E. (2003). "Seismic Scattering at the Top of the Mantle Transition Zone". In: *Earth and Planetary Science Letters* 216.3, pp. 259–269. ISSN: 0012-821X.
- Toro, G. (1995). Probabilistic Models of Site Velocity Profiles for Generic and Site-Specific Ground-Motion Amplification Studies. Technical Report No. 779574. Upton, N.Y.: Brookhaven National Laboratory, p. 147.
- Wessel, P., Luis, J. F., Uieda, L., Scharroo, R., Wobbe, F., Smith, W. H. F., and Tian, D. (2019). "The Generic Mapping Tools Version 6". In: *Geochemistry, Geophysics, Geosystems* 20.11, pp. 5556–5564. ISSN: 1525-2027, 1525-2027.
- Withers, K. B., Olsen, K. B., and Day, S. M. (2015). "Memory-efficient Simulation of Frequency-dependent q". In: *Bulletin of the Seismological Society of America* 105.6, pp. 3129–3142. ISSN: 0037-1106, 1943-3573.
- Withers, K. B., Olsen, K. B., Day, S. M., and Shi, Z. (2019). "Ground Motion and Intraevent Variability from 3D Deterministic Broadband (0–7.5 Hz) Simulations along a Nonplanar Strike-slip Fault". In: *Bulletin of the Seismological Society of America* 109.1, pp. 229–250. ISSN: 0037-1106, 1943-3573.
- Wood, H. (1908). Distribution of Apparent Intensity in San Francisco, in the California Earth-quake of April 18, 1906. Washington, DC: Carnegie Institute of Washington, pp. 220–245.
- Wu, R.-S. (1985). "Multiple Scattering and Energy Transfer of Seismic Waves Separation of Scattering Effect from Intrinsic Attenuation I. Theoretical Modelling". In: *Geophysical Journal International* 82.1, pp. 57–80. ISSN: 0956-540X.
- Zeng, Y. (1993). "Theory of Scattered P- and S-Wave Energy in a Random Isotropic Scattering Medium". In: *Bulletin of the Seismological Society of America* 83.4, pp. 1264–1276. ISSN: 0037-1106.
- Zeng, Y., Anderson, J. G., and Su, F. (1995). "Subevent Rake and Random Scattering Effects in Realistic Strong Ground Motion Simulation". In: *Geophysical Research Letters* 22.1, pp. 17–20. ISSN: 1944-8007.
- Zeng, Y., Su, F., and Aki, K. (1991). "Scattering Wave Energy Propagation in a Random Isotropic Scattering Medium: 1. Theory". In: *Journal of Geophysical Research: Solid Earth* 96.B1, pp. 607–619. ISSN: 2156-2202.

- Zhang, W., Zhang, Z., and Chen, X. (2012). "Three-Dimensional Elastic Wave Numerical Modelling in the Presence of Surface Topography by a Collocated-Grid Finite-Difference Method on Curvilinear Grids". In: *Geophysical Journal International* 190.1, pp. 358–378. ISSN: 0956-540X.
- Zhu, C., Riga, E., Pitilakis, K., Zhang, J., and Thambiratnam, D. (2018). "Seismic Aggravation in Shallow Basins in Addition to One-Dimensional Site Amplification". In: *Journal of Earthquake Engineering* 24.9, pp. 402–412. ISSN: 1363-2469, 1559-808X.